Organotypic head and neck cancer models for advanced preclinical drug testing

Inaugural-dissertation
to obtain the doctoral degree
Doctor rerum naturalium (Dr. rer. nat.)

submitted to the Department of Biology, Chemistry, Pharmacy
of Freie Universität Berlin

by

Leonie Gronbach

2020

This thesis and all associated experiments were prepared and performed from July 2017 to November 2020, under the supervision of Prof. Dr. Monika Schäfer-Korting, Institute of Pharmacy (Pharmacology and Toxicology), Freie Universität Berlin.

1st Reviewer	Prof. Dr. Monika Schäfer-Korting Freie Universität Berlin Institute of Pharmacy (Pharmacology and Toxicology) Königin-Luise-Str. 2+4 14195 Berlin
2nd Reviewer	Prof. Dr. Burkhard Kleuser Freie Universität Berlin Institute of Pharmacy (Pharmacology and Toxicology) Königin-Luise-Str. 2+4 14195 Berlin
Date of disputation	16th March 2021

ACKNOWLEDGEMENT

I would like to express my deepest gratitude to my first supervisor Prof. Dr. Monika Schäfer-Korting, who gave me the opportunity to work on this very interesting research topic. Since my master's thesis in 2016, I worked with her and she always offered her time and expertise when needed besides her fully packed working plan, as professor of pharmacology at the Institute of Pharmacy and executive vice president of Freie Universität Berlin. Thank you for your kindness and trust in me.

My grateful thanks go to Prof. Dr. Burkhard Kleuser, who was willing to serve as the second reviewer of this thesis and who gave me all the time and space I needed, to finish the last publication procedures and to write this thesis. Special thanks go to Prof. Dr. Johanna Plendl and Prof. Dr. Gerhard Wolber for joining my mentoring team at the Dahlem Research School, in my graduate study "Biomedical Sciences". Thank you both for all the critical questions and suggestions, to improve my research project.

I wish to show my great appreciation to Dr. Christian Zoschke, who always cared about my concerns and worked hard and close with me on creating our paper drafts. Thank you for motivating me every single day and your outstanding support in all the countless ways on my journey through the Ph.D.

I would like to thank all my colleagues in the lab, who always created a very enjoyable atmosphere and a time, that I will always look back with a smile. Christopher Wolff, who showed me how to build 3D culture models and helped me with all the belonging methods. Maria Grabowski always helped me with difficult pharmaceutical questions and together with Carola Kapfer and Uta Hirt, constituted the best office roommates I could imagine. I want to thank Dr. Vivian Kral for her support in all the teaching and BB3R happenings. Gabriele Roggenbuck-Kosch's and Petra Heine's assistance in organizational and financial matters is greatly acknowledged. Thanks, Dr. Anja Pfalzgraf, Dr. Christian Hausmann, Charlotte Lübow, Rawan Charbaji, Anne Eichhorst, Patrick Graff, and Dr. Priscila Schilrreff for making it easy for me to go to the lab and stay for long days, even in the hardest experiment-based times.

One of the main advantages for me, working in this institute, was to get to know so many fascinating people all over the world. Dr. Roberta Balansin Rigon (Brazil) and Charlène Dévé (France) became one of my best friends for life. Leticia Da Silva Cruz (Brazil) and Jill Garcia-

Miller (Spain), I had the pleasure to supervise during their master's theses and they helped me, by the way, a lot in my own projects.

I definitely would like to thank all my collaborators, who gave me many different kinds of views and the opportunity to have an insight into plenty of various techniques. It was my pleasure to work in particular with Prof. Dr. Ulrich Keilholz, Prof. Dr. Ingeborg Tinhofer-Keilholz, Prof. Dr. Ulrike Alexiev, Dr. Konrad Klinghammer, Dr. Philipp Jurmeister, Johannes Stellmacher, Prof. Dr. Maria Kristina Parr, Dr. Jan Felix Joseph, Bernhard Wuest, Prof. Dr. Eckart Rühl, Dr. Piotr Patoka, Gregor Germer, and Tamasri Senapati.

Additionally, I want to thank the female promotion, which allowed me two times, to present my work at international congresses by poster and oral presentation.

Last but not least, I would like to thank my parents, for their endless love and support during my whole lifetime. My very last thank goes to my partner and heart, who always makes me smile and remembers me about the important things in life, being the balancing part to my scientific work.

LIST OF ABBREVIATIONS

3Rs	Replacement, reduction, and refinement of animal tests
ADME	Adsorption, distribution, metabolism, elimination
AFM-IR	Atomic force microscopy-based infrared spectroscopy
AUC	Area under the curve
BM	Basement membrane
CAFs	Cancer-associated fibroblasts
CT	Computer tomography
CTCs	Circulating tumor cells
DLT	Dose-limiting toxicity
ECM	Extracellular matrix
EGFR	Epidermal growth factor receptor
ELISA	Enzyme-linked immunosorbent assay
FLIM	Fluorescence lifetime imaging microscopy
HIF-1α	Hypoxia-inducible factor 1α
HNSCC	Head and neck squamous cell carcinoma
IL-6	Interleukin-6
iPSC	Induced pluripotent stem cells
Ki-67	Kiel-67
LDH	Lactate dehydrogenase
MMP	Matrix metalloproteinase
MRI	Magnetic resonance imaging
MRT	Magnetic resonance tomography
MTD	Maximal tolerated dose
M_w	Molecular weight
NOM	normal oral mucosa
OCT	Optical coherence tomography

PDX	Patient-derived xenograft
PET	Positron emission tomography
SCC-25	squamous cell carcinoma-25
SVD	Singular value decomposition
TNM	Tumor size, nodal status, metastasis distribution
TOM	Tumor oral mucosa
TUNEL	TdT-mediated dUTP-biotin nick end labeling
UHPLC-MS/MS	Ultra-high performance liquid chromatography-tandem mass spectrometry
UM-SCC-22B	University of Michigan-squamous cell carcinoma-22B

DIRECTORY

1. Introduction

1.1 Head and Neck Squamous Cell Carcinoma

Epidemiology Head and neck cancer is the seventh most common cancer type and the seventh most frequent cause of death from cancer with 890,000 new cases and 450,000 deaths worldwide in 2018 (1). This results in over 5.5 million affected people with 2.4 million of mouth, 1.7 million of the pharynx, and 1.4 million of the larynx in 2015 with an obvious ascending trend (2). In Germany, 18,246 new cases and 9,894 deaths have been reported in 2018 (1). Head and neck cancer is localized at the lips, the oral cavity, the larynx, the naso-, oro-, and hypopharynx, the salivary glands, the paranasal sinuses, or the nasal cavity. Oral squamous cell carcinoma has the highest prevalence (38%) in head and neck squamous cell carcinoma (HNSCC), with the tongue (44%) and buccal mucosa (33%) as the most affected parts in the oral cavity (3). Men are more likely to be affected than women (2:1) and diagnosed mostly between the age of 55-65 years (4). The main risk factors are tobacco use and alcohol consumption, included in around 75% of all cases (5). The infection of the human papillomavirus is as well an increasingly important risk factor, especially regarding cancer of the oropharynx, while connected to better therapy responsiveness and prognosis. The infection of the Epstein-Barr virus, bad mouth hygiene, and UV-light exposure especially to the lips are also considered risk factors. In Asia chewing betel quid and the areca nut are high-risk factors too (6), leading to highest incidences and making head and neck cancer the most common cancer type in south Asia and the pacific islands (e.g. India and Papua New Guinea) (7). Parts of Europe, South America, and the Caribbean are also associated with high numbers of head and neck cancer patients (8). The average 5-year survival rate is about 34-66% with a high dependency on tumor stage and type (9).

Pathophysiology More than 90% of head and neck cancers are squamous, often arising from leukoplakia and erythroplakia (Figure 1a). The location of the tumor is often connected to the location with the highest exposition of cancer-causing agents like tobacco and alcohol. For example, cigarette smoking more likely leads to SCC of the lips, whereas chewing of the betel quid is linked to SCC of the gingiva and inner cheeks (10). Alcohol consumption, on the contrary, is associated with higher SCC incidences of the oral cavity, hypopharynx, and larynx (11). Later states of the tumor frequently exhibit single lumps or ulcers with raised margins causing mandibular destruction (Figure 1b, c). In HNSCC, tumor cells often spread to regional lymph nodes (40% in oral cancer) and cause second cancer developments (12). These secondary carcinomas are most likely to be formed in the head and neck, lungs, lymph nodes, liver, or bones (13).

Figure 1 Clinical presentation of HNSCC a) leukoplakia of the floor of the mouth and ventral part of the tongue, b) squamous cell carcinoma of the tongue, c) tumor on the floor of the tongue. Images are reprinted from K. D. Hunter (14), R. J. Shaw (15), and J. Bagan (16), with permission granted by Springer Nature, John Wiley and Sons, and Elsevier.

Diagnosis The most common precancerous HNSCC lesions are white and red patches, called leukoplakia and erythroplakia, respectively. Since they are non-itching lesions that don´t heal and can´t be rubbed off, they are often ignored or remain unrecognized, which is one of the reasons, why HNSCC is most often diagnosed in advanced stadiums (17). All abnormalities in the oral cavity, which remain for at least two weeks, are classified as potentially cancerous (18). Further characteristic symptoms of HNSCC belong to changes in voice, dry mouth with difficulties in swallowing, and consequentially worsened nutrition uptake. The loss of teeth, numbness in the mouth, bad breath, globus sensation, as well as speech impediment, are possible symptoms as well (19). When there is an assumption of HNSCC, the next steps for detection can be the palpation of the region, endoscopy, and medical imaging methods such as computer tomography (CT), magnetic resonance tomography (MRT), positron emission tomography (PET), X-ray, and sonography. Tissue biopsies and blood tests are as well important for the determination of the tumor grading and the diagnosis (18). The tumor itself will then be classified by the TNM staging system, taking into account the tumor size (T), the nodal status (N), and the existence of distant metastases (M).

Therapy options Without any treatment, it is reported that 50% of the HNSCC patients die within the following 4 months after diagnosis (20). To face the battle against cancer, it is very important to choose the right therapy option, as early as possible. Since cancer is not one disease, but many, and due to the high heterogeneity of HNSCC, also the therapy has to be decided individually, which makes the best therapy finding challenging. The main therapy options for HNSCC nowadays are surgery, radiotherapy, chemotherapy, and targeted therapy, which are often combined. To find the best individual therapy option, primary tumor site, tumor staging, resectability, but also patient factors as age, the desire for organ preservation, interfering illnesses, and if available empirical therapy responses from earlier treatment, are taken under consideration for suitable therapy management (21). Recurrences after treatment are frequent and the mentioned therapy options are associated with many side effects. Surgery can result in deficits in saliva production, mastication, deglutition, and speech since essential body parts may have to be removed, dependent on the tumor location and invasiveness. Additionally, a surgical margin of 5 mm from the cutting site to the tumor edge is indicated (22). All these impairments and the esthetic aspect can furthermore lead to depression and social isolation. Reconstruction is often a big topic after surgical resection. Radiotherapy often results in mucositis, osteoradionecrosis, inflammation, all associated with pain, salivary gland dysfunction, difficulties in swallowing, and speech, which intensifies the symptoms the patient already has to cope with (23). Most frequently used chemotherapeutics in the management of HNSCC therapy, are docetaxel, cis- or carboplatin, and 5-fluorouracil, which are often combined in the so-called TPF (taxane; platinum; fluorouracil) approach. The first and only approved targeted therapy option in the treatment of HNSCC is to date build-up by cetuximab, an epidermal growth factor receptor (EGFR) inhibitor (24, 25). Chemotherapeutic agents are all given intravenously and are commonly connected to reduced numbers of blood cells, diarrhea, fatigue, nausea, risk of infections, skin irritation, and loss of the hair (26).

In this study, docetaxel, and cetuximab, as commonly anti-cancer therapeutics for HNSCC, were tested for the first time in 3D tissue-engineered normal oral mucosa (NOM) and tumor oral mucosa (TOM) models, to investigate the potential of these newly established models for preclinical drug testing, as well as the benefits of a topical therapy option in HNSCC therapy. Docetaxel (Taxotere®, Sanofi-Aventis), which belongs to the group of taxanes, is a microtubule inhibitor, binding reversible to the β-tubulin unit with high affinity. This prevents the microtubules to assemble and disassemble and leads to a stop in mitotic cell division and can result in apoptosis (27). Docetaxel is a semi-synthetic analog of the 3 times less effective paclitaxel (28), which is only found in the barks of the rare Pacific yew tree. It was first approved for medical use in 1995 and is also used in the therapy of breast, gastric, prostate, ovarian, and non-small cell lung cancer. The most frequent adverse effect of docetaxel is neutropenia. Other common side effects include anemia, gastrointestinal complications, skin erythema, acute respiratory distress, and eye disorders. In the induction chemotherapy, the recommended dose of docetaxel is 75 mg/m^2, applied in a 1 h infusion, administered every 3 weeks in 4 cycles, and combined with cisplatin and 5-fluorouracil (29). Its small size (807.89 g/mol) and its effectiveness make it an interesting drug for topical treatment studies.

Cetuximab (Erbitux®, Merck group) is a chimeric, monoclonal IgG antibody against the EGFR, and was initially induced for colon carcinoma (2004). Since 2006, cetuximab is also approved for advanced head and neck cancers in combination with radiotherapy, and since 2008, cetuximab is as well indicated for recurrent and metastatic head and neck cancer in combination with platinum-based chemotherapy (24, 30). Cetuximab binds competitively to the extracellular site of the EGFR with a 5-10 higher binding affinity than the physiological EGF ligand, and so prevents the receptor to become phosphorylated and activated. This results in the inhibition of several signaling pathways involved in cell proliferation, angiogenesis, and invasion, leading to apoptosis. Cetuximab is applied by infusion and can cause anaphylactic reactions, electrolyte disturbances, severe skin reactions, disorders of the eye, the nervous system, and the liver, as well as neutropenia, representing the main adverse effects. Cetuximab is applied once weekly, with an initial dosage of 400 mg/m^2 and a later dosage of 250 mg/m^2 (31). Due to frequent tumor resistance mechanisms, the treatment efficacy of cetuximab monotherapy is low with a single-agent response rate of 13% (32) and 36%, when combined with other chemotherapeutics (30). The resistance mechanisms are still not completely understood, and the problem is not overcome, which makes cetuximab as well an interesting drug to study.

1.2 Preclinical Drug Evaluation

After the discovery of potential drug candidates, by first target identification, hit discovery, high-throughput screenings, and hit to lead identification and optimization, the drugs reach the preclinical phase. In this preclinical stage, the desired drug effects have to be ensured by *in vitro* and *in vivo* (animal) studies, to validate the drug candidates to their potency. Furthermore, effectiveness, toxicity, and pharmacokinetics and -dynamics have to be elucidated, to optimize the drug's formulation and to find the first-in-human dose before it goes into clinical trials. Consequently, a successful and efficient preclinical phase is strongly dependent on the models' quality.

Model systems In the field of preclinical drug testing, the drug candidate has to go through many different test setups and model systems. The most commonly used model systems for drug testing are nowadays monolayer cell culture and animals (Figure 2). From all possible anti-cancer drugs, passing the preclinical trials, only 3.4% are successful in the following clinical phases (33). To investigate the drug candidate's efficacy and the potential toxicological effects in humans, a good model setup, reflecting closely the *in vivo* situation, is of substantial importance. Monolayer cell culture models are easy to manipulate but fail to mimic the native microenvironment, missing the interaction of different cell types and the necessary architecture and polarity for an *in vivo* cell behavior. So, cell monolayers are unable to answer complex questions and generate doubtable results (34, 35).

This is the reason, why animal models are frequently used since they have the advantage to build up a complete organism. But, as learned from the past, there is a relevant species gap, which sometimes leads to fatal consequences, as we know e.g. from the thalidomide's history. Thalidomide was being used from 1957-61 against nausea and insomnia but proved later to be teratogenic in humans, non-human primates, rabbits, and many more (36, 37). But due to the fact, that mice have been the generally used model for drug testing in that time and turned out to be less sensitive to this drug, thalidomide made it on the market. The thalidomide disaster sensitized for the thinking of suitable drug testing models and changed the way we test new drugs. To combine the human aspect with a living organism, small pieces (3-4 mm) of human tumors have been transplanted subcutaneously into immunocompromised animals like mice, called patient-derived xenografts (PDX) (38). These PDX models turned out to be useful in drug screenings, biomarker development, and the evaluation of personalized medicine strategies (39). Although these PDX ought to maintain their molecular and genetic heterogeneity of the native tumor through serial passages (up to passage 6) (40), there are observations, that the copy number alteration landscape is shifted away from the original primary tumor by ∅12.3% within four passages, and associated to different drug responses (41). Further limitations are long engraftment times, an impaired ability of tumor progression to metastasis, and still the animal gap with e.g. essential differences in pharmacokinetics (42). Additionally, the constrained immune system and the replacement of human by murine stromal tissue (43) can lead to distorted tumor growth and patient drug response (44).

In the course of enhanced animal welfare, the principles of 3Rs (Replacement, Reduction, Refinement), were first described by Russell and Burch in 1959 (45). Since this time, plenty of alternative models have been set up and tested for basic research, pharmacological, and toxicologic questions. So, *in silico* models gained more and more attention, being able to predict drug toxicities and effects, and offer the identification of drug interactions (46), in a high-throughput, low cost, reproducible, and easily adoptable manner (47). Further promising alternative methods are 3D models, which are build up from human cells and can be of various sizes and shapes, accordingly to their application. Spheroids for example are round cell formations of > 500 µm in diameter, surrounded by a gelatinous protein mixture. These cell masses can be easily used in high-throughput assays and can be used as building blocks in tissue engineering (48). But besides these spheroids, there are also organotypic tissue-engineered models, which not only enable the cells to grow in a 3D manner but also try to mimic the polarity and architectural composition of the specific organ, as close as possible. Miniaturized connected 3D models of different cell types furthermore can be integrated into so-called organ- and human-on-a-chips (49), which depict nowadays the closest and most complex human-based 3D models (50, 51). Still, it remains clear, that even the most advanced *in vitro* models will never get along without *in vivo* testing before it goes into clinical trials. However, they can help to reduce animal testing immensely and identify the effects of a drug candidate more efficiently by giving closer prognoses to the human body reactions.

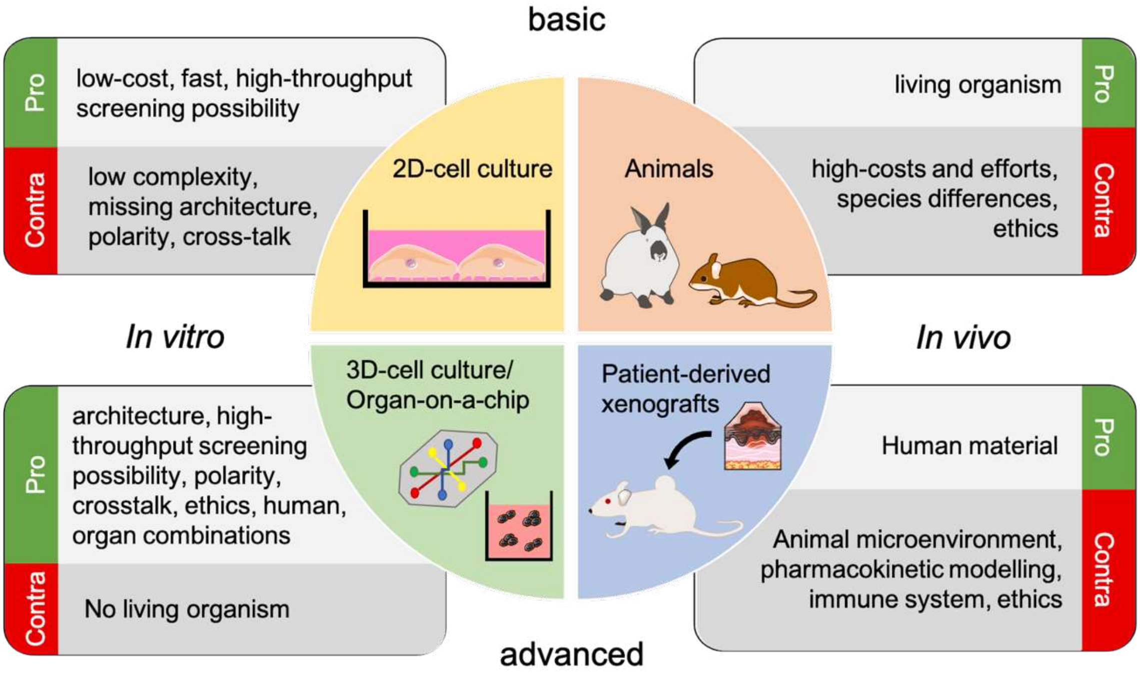

Figure 2 Models for preclinical drug testing and their limitations Traditionally used preclinical models in drug development are 2D- and animal-models, although having many known limitations. Patient-derived xenografts and 3D-modeling, as well as the combined 3D-modeling resulting in Organ-on-a-chip (49), are attempts to overcome these limitations. The advantages and disadvantages of each model system have to be weighed up for every preclinical drug testing experiment. This figure includes images of Servier Medical Art and ChemDraw Professional.

Pharmacokinetic analysis In preclinical drug testing, it is of great importance to know as much as possible about the pharmacokinetic parameters of the drug since the best drug will be useless if it fails to reach the target site, is unstable, or accumulates at undesired tissue sites. As the dose makes the poison, pharmacokinetic analyses help in the dose-finding procedure, to investigate all the steps of the so-called ADME, standing for absorption, distribution, metabolism, and elimination. Dose finding can be very difficult since the best possible effect should be achieved with concurrently the least possible side effects. Especially for anti-cancer drugs which mostly have a narrow therapeutic window, showing steep dose-response relationships for efficacy and toxicity (52), it is important to ensure the most suitable amount of the drug inside the human body. Since higher concentrations of cytotoxic agents can result in more cell-kill, it was assumed that the highest possible concentration should be applied to reach the most efficient effect on the tumor cells. As these cytotoxic agents also affect normal cells, the balance between the desired effect and the severe side effects, so-called dose-limiting toxicities (DLT), has to be found (53). Here, the maximally tolerated dose (MTD) can be the optimal drug dosage for the patient.

It is important to identify potential drug candidates with favorable pharmacokinetic profiles early, already in the preclinical phase, since these drugs are more likely to be effective and safe in humans. Here, 3D models could offer a good opportunity, to study the penetration and distribution of a drug in a human tumor tissue, and may give additional important information to the normally used 2D-cell culture and animal model experiments (54). In the development of new cancer therapeutics, the architecture and composition of the tumor have to be kept in mind, since both affect the intratumoral drug distribution and thus its uptake into the tumor cells (55). Here, the tumor vascularity, permeability, as well as tumor mechanisms to get the drug in and out of the tumor tissue and cells, by e.g. efflux-pumps as the P-glycoprotein 1 (56, 57), can influence the drug concentration in the tumor strongly. Furthermore, insufficient drug uptake caused by lysosomal sequestration can reduce the intracellular drug concentration in the tumor tissue (58). This can influence the drug concentration inside the tumor strongly.

To detect the real drug concentration inside the tumor tissue and not only the free drug in the blood plasma, techniques like magnetic resonance imaging (MRI), PET, or microdialysis can be performed. In the microdialysis thin tubular dialysis membranes can be inserted into various tissues like skin or brain, and be perfused by a physiological solution, which then can collect endogenous and exogenous molecules of interest into small vials (59).

Yet, these methods either show a single time point or the samples need elaborated sample preparation and cannot be analyzed automatically, which also limits the number of measurements. Here, small 3D tissue-engineered models, which are adaptable to automatic and highly sensible devices, as used for ultra-high-performance liquid chromatography-tandem mass spectrometry (UHPLC-MS/MS) measurements, could offer a good study design and are discussed in this thesis.

1.3 Drug detection in tissues

Both, on- and off-target effects will only occur, if sufficient drug levels are reached in the target and non-target tissue. Hence, drug levels within these tissues should be quantified in the early phases of drug development. The binding site of the drug to its target has been previously identified in hit-to-lead analyses, but the real drug distribution in complex tissues has to be further elucidated to see if the drug will really reach its target site and to find out accumulation sites. For drug quantification in tissues, tissue homogenization with coupled liquid chromatography and mass spectrometry was the mainstay in the past (60). However, this method loses spatial information and can only roughly map the drug's distribution within the tumor cells. To get more precise information about the drug's distribution, new techniques nowadays focus on the mapping of the drug's distribution inside tissues and single cells, by high-resolution.

Fluorescence lifetime imaging microscopy Fluorescence lifetime imaging (FLIM) allows for analysis of drug distribution inside living tissues and even the localization in single cells (61). The FLIM setup is composed of a confocal laser scanning microscopy, combined with time-correlated single photon-counting, which allows the detection of fluorescence lifetime curves per pixel (62). The FLIM technique already showed its potential in sensing the polarity, pH, molecular interactions, as well as nanoparticle degradation and cargo release in tissues as i.a. skin (63), which makes FLIM a powerful tool for tissue-drug-interaction studies.

Atomic-force microscopy-based infrared spectroscopy If the resolution should be increased to get an even more precise picture of drug localization in a single cell, the atomic force microscopy, allowing for the highest spatial resolution, presents a useful tool (64). The atomic force microscopy-based infrared spectroscopy (AFM-IR) furthermore allows for chemical analysis and therefore enables the detection of drugs and molecules of interest topographically. In this approach, the tip of the AFM (cantilever) first scans the surface of the sample of interest. Then, an infrared laser beam hits the sample which leads to thermal expansion, resulting from molecular movements in the sample. This thermal expansion causes a bending of the cantilever which then can be detected by a deflection laser and allows for chemical mapping of the sample on a high-resolution base (down to 10 nm) (65).

1.4 Tissue-engineered Models for Drug Testing

Tissue engineering The generation of 3D tissues by combining cell culture with a suitable engineered material, called tissue-engineering, has been and still is an exciting research field for the past four decades. Tissue-engineered models can be of use in regenerative medicine, as reconstructed human skin can be transplanted to severe burn wounds, and tissue-engineered cartilage can replace the damaged tissue in patients suffering from arthrosis (66, 67). It all started in the 1980s when biopsies were used to cultivate epithelial sheets of skin (68) and oral mucosa (69) for autologous graft transplantation. Advances in tissue-engineering with the integration of a supporting substructure significantly improved these fragile, contractile, uneasy handling epithelial sheets (70). Many tissues as e.g., from lung, blood vessels, cartilage, and intestine followed, and till now intensive studies are ongoing to improve these constructs for preclinical testing as well (71-74). To make these models more complete and combining different types of models, organ- and human-on-a-chip devices are topics of the current research focus (75). Most tissue-engineered models consist of three components, which are the tissue-specific cells, a matrix where they grow on, and the supportive supplements included in the culture medium. The possibilities in different matrix constructs are unlimited, as they can be made out of liquid biological components like collagen, chitosan, gelatin, or solid synthetic components as e.g., 3D-printed or electrospun polymers (76, 77). Since tissue-engineered models always try as best as possible to emulate the *in vivo* situation, in-depth knowledge of the composition and important features of the respective tissue is of outermost importance.

Oral mucosa and HNSCC *in vivo* In the oral cavity, the main oral mucosa functions are the protection of the underlying tissue from mechanical damage and the entry of microorganisms, as well as the sensation and digestion of nutrients. Here, we differentiate between keratinized and non-keratinized oral mucosa. The keratinized oral mucosa we find at the gingiva and hard palate called masticatory mucosa and on the surface of the tongue, called specialized mucosa. The non-keratinized oral mucosa covers the inner side of the cheeks, the soft palate, and the floor of the mouth and is called lining mucosa (78). All mucosa types have in common to consist of two major compartments, a lamina propria, and an epithelium. The epithelium consists of a basal and spinous layer, and an additional granular and keratinized layer, when it’s a keratinized mucosa type (Figure 3).

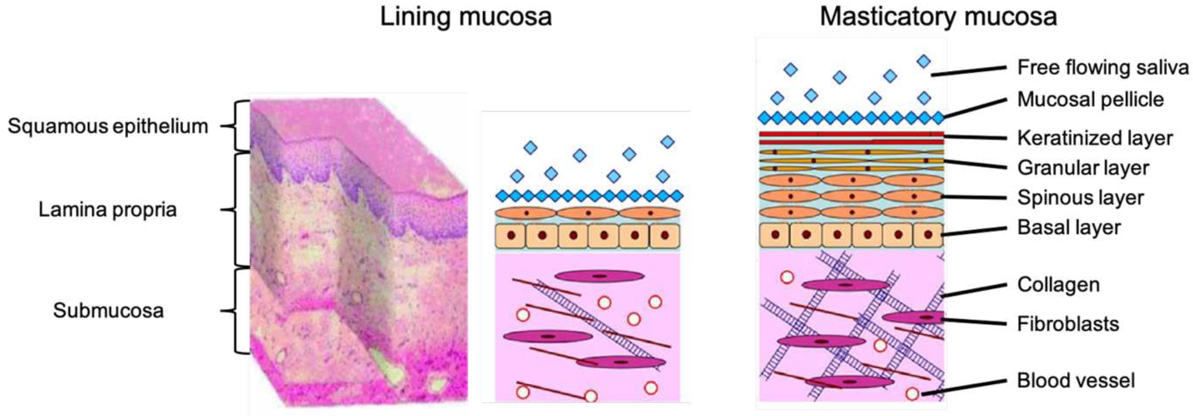

Figure 3 Oral mucosa morphology. The oral mucosa is composed of an epithelium, a lamina propria, and the underneath submucosa. Lining mucosa is non-keratinized and composed of a basal and a spinous layer on top of the lamina propria, while masticatory mucosa is keratinized and has an additional granular and keratinized layer. Images are reprinted from A. T. Cruchley and Y. Otsuka-Tanaka with permission granted by Springer Nature and SAGE Publications (78, 79).

Within these layers, mainly keratinocytes, but also melanocytes, Langerhans cells, and Merkel cells are present. The basal keratinocytes serve as progenitor cells, undergoing differentiation, by concurrently migrating to the epithelial surface. Here, cytokeratins are the most fundamental markers for epithelial differentiation and cell type (80).

Between the basal layer and the lamina propria, there is a connective tissue, the basal membrane consisting of laminin, collagen IV, and fibronectin. The lamina propria mainly consists of oral fibroblasts and collagen I, but vascular and lymphatic vessels, nerves, salivary glands, and occasionally macrophages, mast cells, and lymphocytes are found as well (81). Hereby, fibroblasts play a significant role in the extracellular matrix (ECM) production and the epithelial phenotype, as it was shown that keratinocytes are less able to proliferate and migrate without fibroblasts in the matrix (82) and dermal fibroblasts led to a more differentiated epithelium in contrast to oral keratinocytes co-cultured with mucosal fibroblasts (83). In the submucosa, small and big salivary glands are located and responsible for the saliva production, which is transported via small ducts to the mucosa surface. The saliva protects the mucosa and helps in nutrition uptake. Saliva is mainly composed of glycosylated proteins, antimicrobial peptides, and digestive enzymes, and divided into the mucosal pellicle (high M_w glycoproteins) and the free-flowing saliva (low M_w glycoproteins), building a complex network (84).

In the transformation process from a normal oral keratinocyte to a malignant tumor cell, various possible mutations concerning the hallmarks of cancer, as permanent cell proliferation, resistance to growth suppressors and cell death mechanisms, unlimited replication, and the activation of angiogenesis and invasion, can take place (85). But there are some mutations, which are often present as mutations of the EGFR, which is overexpressed in over 90% HNSCC cases (86), as well as mutations in the *p53* and *phosphatase and tensin homolog* genes. These neoplastic changes then start to get visible in histology by hyperplasia and dysplasia. Tumor cells often show enlarged nuclei with characteristic pleomorphism (Figure 4). Commonly, the atypic cells are first seen in the lower one-third of the epithelium (mild dysplasia), and then spreading into the upper layers (moderate dysplasia) and finally covering the complete epithelial layer (carcinoma in situ). By breaking through the basement membrane, the carcinoma in situ becomes a carcinoma, infiltrating the subepithelial tissue and forming nests and cords (87). With advanced tumor growth, the angiogenesis is increased, and the tumor cells can invade into i.e., skeletal muscles, cranial bones, and lymph nodes, and form secondary tumors.

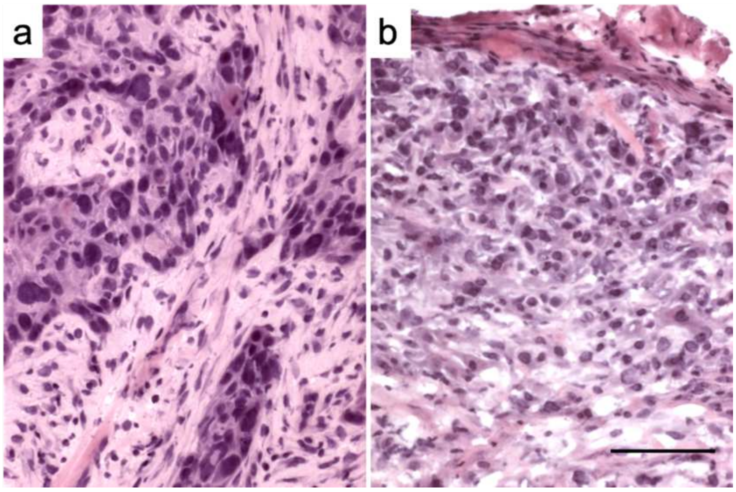

Figure 4 Head and neck squamous cell carcinoma histology. Hematoxylin and eosin staining of a) a T2N0M0, G2 squamous cell carcinoma of the tongue from a 65-year-old man, and b) a further tumor passage which was grown in a patient-derived xenograft. With preparation and permission of Dr. Konrad Klinghammer from Charité Berlin.

Oral mucosa and HNSCC 3D models In recent years various oral mucosa models have been developed, characterized, and analyzed, always keeping the specific research question and purpose in mind. 3D NOM models found their use in various fields like host-pathogen interaction studies (88, 89), dental material toxicity (90), and mouth wash assessment studies (91, 92). There can be for example split-thickened models, only consisting of the epithelial layer and full-thickness models consisting of both, the epithelial layer and the lamina propria. These split-thickened models are also found on the market from Skinethic laboratories (Lyon, France) and MatTek Corp. (Ashland, MA, United States), representing oral and gingival oral mucosa, consisting of 3D multilayered keratinocyte cell lines. The building procedure is very similar to skin models, but the small sizes in donor oral tissues are limiting the available numbers of primary cells for oral mucosa models. Mostly cancer cell lines are used to build up the epithelial layer, which makes it difficult to determine drug impacts on the normal oral mucosa.

Besides the variability of cells, the scaffold selection is an important step for a good tissue-engineered model since various scaffold materials are differing in porosity, mechanical properties, biostability, and biocompatibility, showing high impacts on the model's morphology and longevity. Common scaffolds are based on for example collagen, gelatin, fibrin, or synthetic polymers. The major advantages of collagen-based models are high biocompatibility and a good keratinocyte multilayer formation providence (81).

Tumor microenvironment and the Extracellular matrix

Everything which surrounds a cell has an impact on its morphology and behavior. The tumor microenvironment is the most important key player in tumor progression and drug response (93). Due to its complexity, many factors have to be considered, when trying to reflect the *in vivo* tumor situation. The main components of the tumor microenvironment are stromal fibroblasts, keratinocytes, infiltrating immune cells, the blood and lymphatic network, as well as the ECM. The tumor cells can use these surrounding normal cells for facilitated progression and invasion, by manipulating their secretion of growth factors, chemokines, and ECM degradation enzymes.

The ECM gives structural support to all the cells and facilitates a continuous cellular cross-talk, maintaining tissue homeostasis (93). Since the ECM is a highly dynamic and variable structure that is constantly remodeled, it is difficult to mimic it properly. The ECM is mainly composed of collagen, laminin, fibronectin, and heparan sulfate proteoglycans (94). A specialized ECM is depicted by the basement membrane (BM), which separates the epithelium from the stroma. For the tumor, the BM reflects a border that has to be overcome by BM/ECM remodeling. Thereby, matrix-degrading enzymes, like matrix metalloproteinases (MMPs) or heparanases (95) can help to enable angiogenesis and invasion. All these named components, but also biochemical concentration gradients and tissue polarity have to be considered in tissue-engineered models and preclinical testing, having a high impact on tumor drug response and chemoresistance development (96). Also, the stiffness of the tumor matrix has a strong influence on tumor progression by more likable activation of oncogenic intracellular signaling and the transformation of surrounding fibroblasts to cancer-associated fibroblasts (CAFs) (97, 98).

Being part of the oral mucosa microenvironment, saliva plays a significant role in the maintenance of oral health by protecting the teeth from caries and the oral cavity from bacterial infections. Since the saliva composition can be very diverse, the production of useful artificial saliva is challenging (99). Although saliva production is reduced in oral tumors, the saliva composition can be even changed in patients of HNSCC particularly after radiotherapy treatment (100), which makes it nearly impossible to mimic by artificial saliva. Due to its functions in tissue repair, buffering acid productions by controlling the plaque pH, and digestion by containing enzymes, saliva also has a high impact on drug release and its effects and has to be taken into account in preclinical studies.

1.5 Thesis Aim and Outline

Head and neck cancer is one of the most aggressive cancer types worldwide and associated with high mortality and increasing incidence rates. Current therapy options are associated with severe side effects, and high resistance and recurrence rates. Although intense research is done to improve the patients' situations, the success is kept within a limit, highlighting an urgent need for more effective therapies. Among other reasons, the shortcomings of preclinical test platforms in mimicking the patients' characteristics, currently limit the translational success from bench to bedside.

The aim of this thesis was to develop a full-thickness 3D oral mucosa model with integrated tumor cells to mimic head and neck squamous cell carcinoma for improved preclinical drug testing, which was proofed by various aspects (Figure 5). Normal oral mucosa (NOM) models, serving as healthy control, and tumor oral mucosa (TOM) models, with different HNSCC cell types, have been morphologically characterized and tested for drug application studies. Therefore, two drugs of different sizes and classes, used as standard therapeutics in HNSCC therapy, were selected. Docetaxel, a microtubule inhibitory which belongs to the most effective chemotherapeutics against HNSCC, and cetuximab, an inhibitor of the EGFR and the only approved targeted therapy option in HNSCC treatment, were chosen to analyze the drug testing potential of the established models. Both drugs have been applied systemically and topically to the models, matching clinically used drug concentrations, as described in **chapter 2**.

To elucidate tumor re-growth following initial treatment, long-term cultivation of tumor models is needed. As the tumor microenvironment is a leading factor in tumor cell behavior and protein expression, the ECM as the major component of the tumor microenvironment plays a fundamental role in cancer progression. To clarify the benefit of a fully human-based ECM approach on head and neck cancer models, respective 3D oral mucosa models were developed, cultured for elongated culture periods, and morphologically analyzed, as described in **chapter 3**.

Pharmacokinetic profiling is a very important parameter for the dosing and application periods of new drugs. Pharmacokinetic profiles can be very variable from animals to humans and as well from human to human. For preclinical testing, it would be useful to know the range of drug concentration at the target tissue site. To investigate the pharmacokinetics in preclinical models, testing on 3D oral mucosa models has been combined with online drug analysis by an ultra-high-performance liquid chromatography-tandem mass spectrometry (UHPLC-MS/MS) device, as described in **chapter 4**.

Finally, to take the results from chapter 2-4 together into a greater relation, the findings are related to the existing knowledge about head and neck cancer therapy and the actual preclinical testing opportunities, in **chapter 5**.

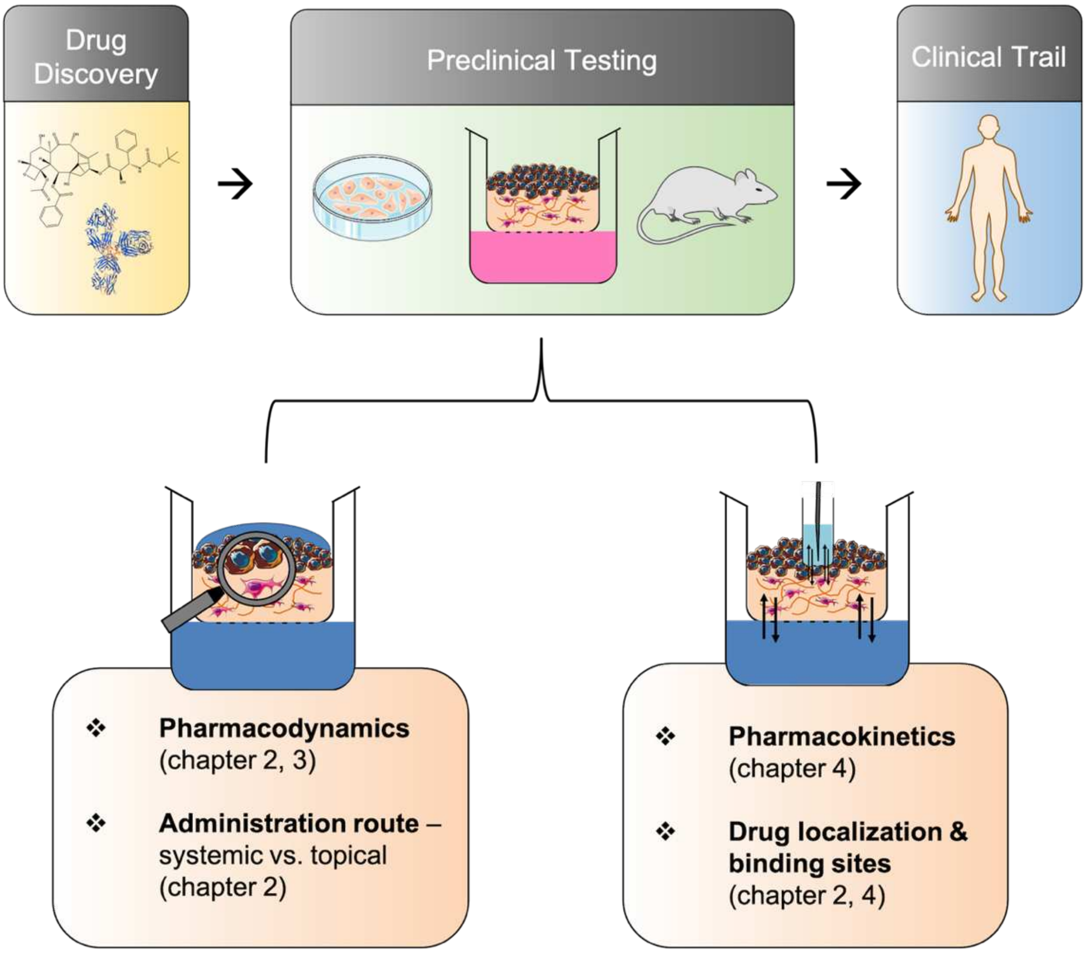

Figure 5 3D Oral Mucosa Models for preclinical drug testing After drug discovery, drugs are usually tested in 2D-cell culture and animal models before it goes into clinical trials. This thesis aimed to investigate the potential of 3D oral mucosa models for preclinical drug testing. The outcomes of the different investigations are presented in chapters 2-4. This figure includes images of Servier Medical Art and ChemDraw Professional.

2. Development and Characterization of Oral Mucosa Models for Advanced Drug Testing

Leonie Gronbach[1], Christopher Wolff[1], Konrad Klinghammer[2], Johannes Stellmacher[3], Philipp Jurmeister[4], Ulrike Alexiev[3], Monika Schäfer-Korting[1], Ingeborg Tinhofer[5,6], Ulrich Keilholz[7], Christian Zoschke[1]

[1] Freie Universität Berlin, Institute of Pharmacy (Pharmacology & Toxicology), Königin-Luise-Str. 2+4, 14195 Berlin, Germany

[2] Charité – Universitätsmedizin Berlin, corporate member of Freie Universität Berlin, Humboldt-Universität zu Berlin, and Berlin Institute of Health, Department of Hematology and Oncology, Berlin, Germany

[3] Freie Universität Berlin, Institute of Experimental Physics, Freie Universität Berlin, Arnimallee 14, 14195 Berlin, Germany

[4] Charité – Universitätsmedizin Berlin, corporate member of Freie Universität Berlin, Humboldt-Universität zu Berlin, and Berlin Institute of Health, Institute of Pathology, Berlin, Germany

[5] Charité – Universitätsmedizin Berlin, corporate member of Freie Universität Berlin, Humboldt-Universität zu Berlin, and Berlin Institute of Health, Department of Radiooncology and Radiotherapy, Berlin, Germany

[6] German Cancer Research Center (DKFZ), Heidelberg and German Cancer Consortium (DKTK) Partner Site Berlin, Berlin, Germany

[7] Charité – Universitätsmedizin Berlin, corporate member of Freie Universität Berlin, Humboldt-Universität zu Berlin, and Berlin Institute of Health, Comprehensive Cancer Center, Berlin, Germany

Biomaterials, 258, 120277

https://doi.org/10.1016/j.biomaterials.2020.120277

2.1 Contribution to Advanced Preclinical Drug Testing

Head and neck cancer is often associated with high recurrence rates and drug resistance. Since only a few drugs are able to pass the clinical trials, we have to improve our pre-clinical test models. In this study, we generated 3D TOM models to improve preclinical drug testing in head and neck cancer therapy, with the attempt of topical treatment. The 3D models emulated closely the *in vivo* situation in morphology with also reflecting the original tumor grading. Docetaxel treatment reduced the tumor volume, decreased the numbers of proliferating cells, increased the numbers of apoptotic cells, and lactate dehydrogenase (LDH) and interleukin-6 (IL-6) values. These effects could be achieved with fewer drug amounts by a topical, compared to a systemic application. Since local application of drugs is generally considered to have less systemic side effects, the high efficacy of topical treatment appears promising for neoadjuvant or add-on therapy of early or non-resectable cancers. Neither systemic nor topical application of cetuximab reduced the tumor cell proliferation, in the 3D TOM models. This cetuximab resistance was inherent to the 3D TOM models, since the binding of cetuximab could be detected in the tumor tissue by FLIM-analysis.

This study was conducted and designed by me under the supervision of Prof. Dr. Monika Schäfer-Korting and Dr. Christian Zoschke. The building and morphological analysis of the models, LDH detection, enzyme-linked immunosorbent assays (ELISA), as well as the TdT-mediated dUTP-biotin nick end labeling (TUNEL) assays, were performed by me, with the support of Christopher Wolff. FLIM analysis of cetuximab detection has been implemented by Prof. Ulrike Alexiev and Johannes Stellmacher. Dr. Konrad Klinghammer provided primary tumor cells from patient-derived xenografts. The model's morphology has been validated by the pathologist, Dr. Philipp Jurmeister. The data have been critically discussed with Prof. Ingeborg Tinhofer-Keilholz and Prof. Ulrich Keilholz. The original paper draft was created by me and Dr. Christian Zoschke and revised together with the co-authors.

2.2 Equity Ratio Statement

Title of the Manuscript

"A multilayered epithelial mucosa model of head and neck squamous cell carcinoma for analysis of tumor-microenvironment interactions and drug development"

Journal Biomaterials

Authorship First author

Status published

Own contribution

- Conception and design of the study together with the co-authors
- Acquisition of the entire data set
    - Model establishment, building, and treatment
    - Morphological and functional characterization
    - LDH release measurements
    - Protein analysis by ELISA and immunofluorescence
- Developing the figures
- Writing original draft together with Christian Zoschke
- Revising the entire manuscript together with the co-authors

2.3 Publication

Biomaterials 258 (2020) 120277

Contents lists available at ScienceDirect

Biomaterials

journal homepage: www.elsevier.com/locate/biomaterials

A multilayered epithelial mucosa model of head neck squamous cell carcinoma for analysis of tumor-microenvironment interactions and drug development

Leonie Gronbach [a], Christopher Wolff [a], Konrad Klinghammer [b], Johannes Stellmacher [c], Philipp Jurmeister [d], Ulrike Alexiev [c], Monika Schäfer-Korting [a], Ingeborg Tinhofer [e,f], Ulrich Keilholz [g], Christian Zoschke [a,*]

[a] Freie Universität Berlin, Institute of Pharmacy (Pharmacology & Toxicology), Königin-Luise-Str. 2+4, 14195, Berlin, Germany
[b] Charité – Universitätsmedizin Berlin, Corporate Member of Freie Universität Berlin, Humboldt-Universität zu Berlin, And Berlin Institute of Health, Department of Hematology and Oncology, Charitéplatz 1, 10117, Berlin, Germany
[c] Freie Universität Berlin, Institute of Experimental Physics, Arnimallee 14, 14195, Berlin, Germany
[d] Charité – Universitätsmedizin Berlin, Corporate Member of Freie Universität Berlin, Humboldt-Universität zu Berlin, And Berlin Institute of Health, Institute of Pathology, Charitéplatz 1, 10117, Berlin, Germany
[e] Charité – Universitätsmedizin Berlin, Corporate Member of Freie Universität Berlin, Humboldt-Universität zu Berlin, And Berlin Institute of Health, Department of Radiooncology and Radiotherapy, Charitéplatz 1, 10117, Berlin, Germany
[f] German Cancer Research Center (DKFZ), Heidelberg and German Cancer Consortium (DKTK) Partner Site Berlin, Berlin, Germany
[g] Charité – Universitätsmedizin Berlin, Corporate Member of Freie Universität Berlin, Humboldt-Universität zu Berlin, And Berlin Institute of Health, Comprehensive Cancer Center, Charitéplatz 1, 10117, Berlin, Germany

ARTICLE INFO

Keywords:
Drug evaluation
Head and neck cancer
Monoclonal antibodies
Taxanes
Tissue engineering

ABSTRACT

Pharmacotherapy of head and neck squamous cell carcinoma (HNSCC) often fails due to the development of chemoresistance and severe systemic side effects of current regimens limiting dose escalation. Preclinical models comprising all major elements of treatment resistance are urgently needed for the development of new strategies to overcome these limitations. For model establishment, we used tumor cells from patient-derived HNSCC xenografts or cell lines (SCC-25, UM-SCC-22B) and characterized the model phenotype. Docetaxel and cetuximab were selected for comparative analysis of drug-related effects at topical and systemic administration. Cetuximab cell binding was mapped by cluster-based fluorescence lifetime imaging microscopy.The tumor oral mucosa (TOM) models displayed unstructured, hyper-proliferative, and pleomorphic cell layers, reflecting well the original tumor morphology and grading. Dose- and time-dependent effects of docetaxel on tumor size, apoptosis, hypoxia, and interleukin-6 release were observed. Although the spectrum of effects was comparable, significantly lower doses were required to achieve similar docetaxel-induced changes at topical compared to systemic application. Despite displaying anti-proliferative effects in monolayer cultures, cetuximab treatment showed only minor effects in TOM models. This was not due to inefficient cetuximab uptake or target cell binding but likely mediated by microenvironmental components.We developed multi-layered HNSCC models, closely reflecting tumor morphology and displaying complex interactions between the tumor and its microenvironment. Topical application of docetaxel emerged as promising option for HNSCC treatment. Aside from the development of novel strategies for topical drug delivery, our tumor model might help to better understand key regulators of drug-tumor-interactions.

1. Introduction

Head and neck cancer is the seventh most common cancer type by incidence and mortality, with 890,000 new cases and 450,000 deaths worldwide in 2018 [1]. Treatment remains challenging since current therapy options including surgery, radiotherapy, chemotherapy or their combination result in five-year survival rates below 50% for patients with locally advanced disease [2]. Drug resistance and toxicity limit the

---

[*] Corresponding author. Freie Universität Berlin, Institute of Pharmacy (Pharmacology & Toxicology), Königin-Luise-Str. 2+4, 14195, Berlin, Germany.
E-mail address: christian.zoschke@fu-berlin.de (C. Zoschke).

https://doi.org/10.1016/j.biomaterials.2020.120277
Received 24 February 2020; Received in revised form 23 June 2020; Accepted 31 July 2020

efficacy of current chemotherapeutics such as cis- or carboplatin, 5-fluorouracil, and taxanes. The introduction of cetuximab, nivolumab, and pembrolizumab improved the outcome but did not overcome the problem of primary or acquired treatment resistance in the majority of patients [3,4]. An improved understanding of the underlying mechanisms is imperative to develop more effective treatment regimens.

Current preclinical models have low power to predict treatment efficacy, especially in oncology. Only 3.4% of investigational new anticancer drugs, which have been effective and safe in pre-clinical studies, successfully complete clinical trials [5]. While animal models are affected by differences to the human pathophysiology [6], monolayers of human tumor cells lack the architecture and the microenvironment of tumors. Three-dimensional (3D) cultures as tumor spheroids can partly overcome these limitations [7]. However, tissue polarity which has an important impact on cell-cell and cell-matrix interactions, as well as on tissue functions [8] is lacking in current 3D models. Thus, multi-layered mucosa models might better imitate the tumor microenvironment in head and neck squamous cell carcinoma (HNSCC) and the biological processes involved in tumor progression and treatment resistance.

In the present study, we aimed at developing a novel multi-layered HNSCC model containing important oral mucosal components, thereby reflecting more closely tumor morphology and microenvironment. After successful establishment and basal characterization of morphology and epithelial gene expression patterns, two drugs from clinical routine treatment (docetaxel and cetuximab) with different pharmacological targets and physicochemical properties were selected for drug testing. We assessed whether these models can be used for the development of topical drug delivery, an approach not yet introduced into clinical practice for HNSCC treatment despite known dose-limiting toxicities of current drug regimens and general evidence of less systemic side effects of topical administration [9,10].

2. Materials and methods

2.1. Materials

Collagen G, DMEM 10x and HEPES buffer were purchased from Biochrom (Darmstadt, Germany). The primary antibodies were purchased from abcam (Cambridge, UK): Hypoxia-inducible factor (HIF)-1α (1:200, ab51608), interleukin (IL)-6 (1:100, ab9324), keratin-13 (1:200, AE8), Ki-67 (1:100, ab16667), laminin-V (1:500, P3H9-2), vascular endothelial growth factor (VEGF, 1:200, ab1316). Anti-mouse and anti-rabbit IgGs (H + L), with F (ab')2 Fragment (Alexa Fluor® 488 and 594 Conjugate) were obtained from Cell Signaling Technology (Danvers, MA, USA).

Human oral keratinocytes from oral mucosa and human oral fibroblasts from the oral cavity were used from one single donor per batch. Cells as well as keratinocyte and fibroblast media were purchased from ScienCell (Carlsbad, CA, USA). The HNSCC cell line SCC-25 (RRID: CVCL_1682 [11]) was a generous gift from Howard Green, Dana-Farber Cancer Institute (Boston, MA, USA) and UM-SCC-22B cells (RRID: CVCL_7732 [12]) were purchased from Sigma-Aldrich (Munich, Germany). HNSCC cells were isolated from two patient-derived xenografts (PDX [13]). The experimental procedures conformed to the principles of the Declaration of Helsinki and informed written consent was obtained from all the donors.

The following medium components were obtained from Sigma Aldrich: Adenine HCl monohydrate, amphotericin B, cholera toxin, DMEM nutrient mixture F-12 Ham, DMEM/F-12 GlutaMAX, hydrocortisone, insulin, L-ascorbic acid, MEM minimum essential medium, transferrin, and triiodo-L-thyronine. Bovine serum albumin solution, collagenase, trypsin solution and the *in situ* cell death detection kit were also purchased from Sigma Aldrich. 12-well plates and 12-well inserts (0.4 µm pore size) were obtained from Greiner bio-one (Leipzig, Germany). EGF and non-essential amino acids were purchased from ThermoFisher Scientific (Waltham, MA, USA).

2.2. Patient-derived xenograft processing

Patient-derived xenograft tissue was cut into 3 mm thick pieces, incubated for 1 h at 37 °C in 0.1% collagenase type IV/trypsin solution, and agitated every 10 min. The reaction was stopped by medium containing 9% fetal calf serum and the suspension centrifuged (1000 g for 5 min) and filtered through a cell strainer (pore size: 0.7 µm). The mouse cell depletion kit (MiltenyiBiotec; Bergisch Gladbach, Germany) was used to remove the remaining mouse cells.

2.3. Cell culture

Human oral keratinocytes and human oral fibroblasts were cultured in oral keratinocyte and fibroblast medium, respectively. The SCC-25 cell line and the PDX-derived tumor cells were grown in DMEM/F-12 Ham medium, supplemented with 9% fetal calf serum, 0.9% L-glutamine, and penicillin/streptomycin. The UM-SCC-22B cell line was grown in MEM, supplemented with 9% fetal calf serum and 0.9% non-essential amino acids at 37 °C in a humidified atmosphere with 5% CO_2. The cell lines were regularly checked by single nucleotide polymorphism authentication (Multiplexion; Heidelberg, Germany). The medium was changed three times a week, and cells were passaged after reaching confluency of 80%. Cell culture was performed according to standard operating procedures and referred to good cell culture practice.

2.4. MTT assay

The inhibitory effect of cetuximab in monolayer cultures of HNSCC cell lines was determined using the MTT assay. Briefly, cells were seeded in a 96-well plate at a density of 500 (SCC-25) or 1000 cells/well (UM-SCC-22B). Twenty-four hours after seeding, cetuximab was added at the indicated concentrations (range: 0.1–100 µg/mL). Cell monolayers were then cultivated for 8 days until reaching confluency of ~80% in untreated controls. At the end of the experiment 3-(4,5-dimethylthiazol-2-yl)-2,5-diphenyltetrazolium bromide reagent (MTT) was added to the cells. After 1 h of incubation, formazan complexes were dissolved in DMSO and absorbance was measured at 595 nm with the AR2001 microplate reader (Anthos Mikrosysteme GmbH; Krefeld, Germany). Survival fractions after cetuximab treatment were calculated based on the survival of untreated cells. Survival fractions at each dose level were determined in sextuplets. At least three independent experiments were carried out.

2.5. Building of multi-layered tumor oral mucosa (TOM) models

Normal multi-layered oral mucosa consists of a lamina propria underneath an epithelium. To build a lamina propria in our *ex vivo* model, 0.1×10^6 human oral fibroblasts per model were embedded in collagen G (Fig. 1a). For normal oral mucosa (NOM) models, 1×10^6 of human oral keratinocytes were seeded onto the lamina propria compartment on day 7. A Teflon ring (Ø 7.5 mm) placed for 4 h on the model surface kept the cell suspension in place. For TOM models, we seeded 0.8×10^6 of human oral keratinocytes on day 7 and added 0.2×10^6 of SCC-25, UM-SCC-22B or PDX-derived tumor cells on day 8 onto the lamina propria compartment. The growth medium for TOM and NOM models consisted of DMEM-F12 GlutaMAX, 9% fetal calf serum, 0.9% L-glutamine, 0.9% penicillin/streptomycin 0.9%, 40 µmol/l adenine HCl monohydrate, 30 µg/l amphotericin B, 0.1 nmol/l cholera toxin, 10 µg/l EGF, 3.5 mL/l hydrocortisone, 4.4 mg/l insulin, 0.5% non-essential amino acids, 4.4 mg/l transferrin and 2 nmol/l triiodothyronine. The growth medium was changed three times a week and replaced by differentiation medium at day 14. The differentiation medium consisted of growth medium completed with 0.25 mmol/l ascorbic acid. From day 14 onwards, the model surface was kept medium-free to expose the epithelium to the air.

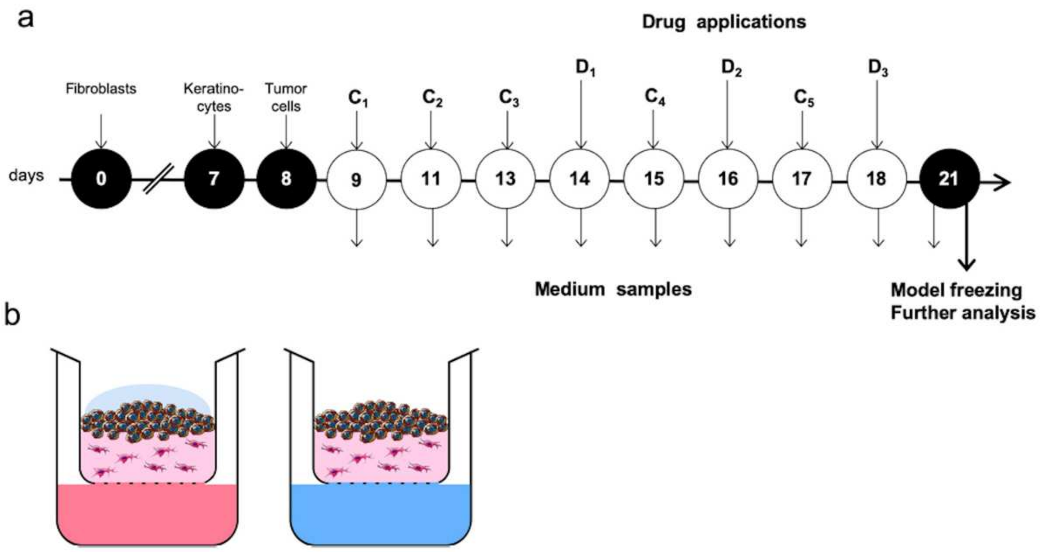

Fig. 1. Procedure outline. (a) For model building fibroblasts were embedded into collagen on day 0. On day 7 the oral keratinocytes and on day 8 the tumor cells were seeded onto the models. Docetaxel (D) was applied three times and cetuximab (C) five times. Medium samples were collected on each day of treatment and on day 21. Models were subjected to morphological analysis on day 21. (b) Schematic cross-section of TOM models following topical and systemic drug administration (green). (For interpretation of the references to color in this figure legend, the reader is referred to the Web version of this article.)

On day 21, the models were frozen and stored at −80 °C (Fig. 1a).

2.6. Drug treatment of TOM models

Docetaxel (M = 808 Da; S1148, Selleckchem, Houston, TX, USA) was dissolved in DMSO to a stock solution of 70 mg/mL and diluted in differentiation medium to final concentrations of 0.007, 0.07, 0.7, 7 μg/mL. Differentiation medium containing 0.01% DMSO served as solvent control since this was the maximum DMSO concentration among all drug doses. Docetaxel was applied three times per model (Fig. 1a).

Cetuximab (M = 146 kDa; A2000, Selleckchem) was solubilized in PBS to a stock solution of 5.2 mg/mL and diluted to 10 and 100 μg/mL to a maximum concentration of 0.2% PBS in differentiation medium. Cetuximab was applied repeatedly five times per model (Fig. 1a).

We administered the drugs every 48 h, considering the doubling time of about 50 h for SCC-25 cells and 34 h for UM-SCC-22B cells [14]. Drug doses corresponded to plasma levels in patients. The steady state concentrations were calculated according to equation (1) with the following parameters: bioavailability F = 1, D = 75 mg/m^2 (docetaxel), 250 mg/m^2 (cetuximab), τ = 48 h, CL = 21 l/h/m^2 (docetaxel), 0.022 l/h/m^2 (cetuximab) [15,16].

$$c_{av}^{ss} = \frac{FD}{\tau CL} \qquad \text{(Eq. 1)}$$

The calculated steady-state concentration for docetaxel was 0.074 μg/mL. Taking into account the clinically observed c_{max} of 3.7 μg/mL and c_{min} of 0.007 μg/mL [17], we decided to test the docetaxel concentration range from 0.007 to 7 μg/mL.

Pharmacokinetic data for cetuximab were more variable. The calculated steady-state concentration of 237 μg/mL was far above the trough value (c_{min}) of 10 μg/mL [18]. Steady-state concentrations from the market authorization studies of cetuximab suggested a concentration, varying between 41 and 156 μg/mL [16]. Consequently, we applied 10 or 100 μg/mL cetuximab to the models.

To test the systemic and topical drug application, both drugs were applied either by administering the drug solution on the model surface or by supplementing the differentiation medium underneath the model (Fig. 1b). The same concentrations of the drug solutions were used in systemic and topical drug application. The topically applied volume was selected to cover the entire surface of the TOM models. Due to the difference in the applied volumes (Table 1, 4,500 μL systemic vs. 40 μL topical), the final drug dose was 112.5-fold higher at systemic compared to topical administration.

2.7. Histochemical and immunofluorescence analyses

At the end of drug exposure, the TOM cultures were snap-frozen and cut into 7 μm slices using a cryotome (Leica CM 1510 S; Leica, Wetzlar, Germany). Cryosections were subjected to staining with hematoxylin-eosin (H/E), fluorescence-labeled antibodies for epithelial cell markers, or periodic acid-Schiff (PAS). To detect the number of apoptotic cells in cryosections of the TOM models, the *in situ* cell death detection kit was used according to the manufacturer's instructions. Apoptosis detection is based on TdT-mediated dUTP-biotin nick end labeling (TUNEL). Pictures were taken with a fluorescence microscope (BZ-8000, Keyence; Neu-Isenburg, Germany) and analyzed for epithelial thickness, proliferation index, and apoptosis using the ImageJ software [19].

2.8. Conditioned medium analyses

Aliquots from the conditioned culture medium were collected at the indicated time points and stored at −80 °C until analysis. Interleukin-6 (IL-6) secretion was quantified by the human IL-6 uncoated ELISA

Table 1
Correlation of drug concentrations (μg/mL) and drug doses (μg). 4.5 mL systemic and 40 μL topical treatments resulted in the doses indicated in the table.

	Docetaxel				Cetuximab	
c_{Drug} [μg/mL]	0.007	0.07	0.7	7	10	100
topical dose [μg]	3×10^{-4}	3×10^{-3}	0.03	0.3	0.4	4
systemic dose [μg]	0.03	0.3	3.2	31.5	45.0	450

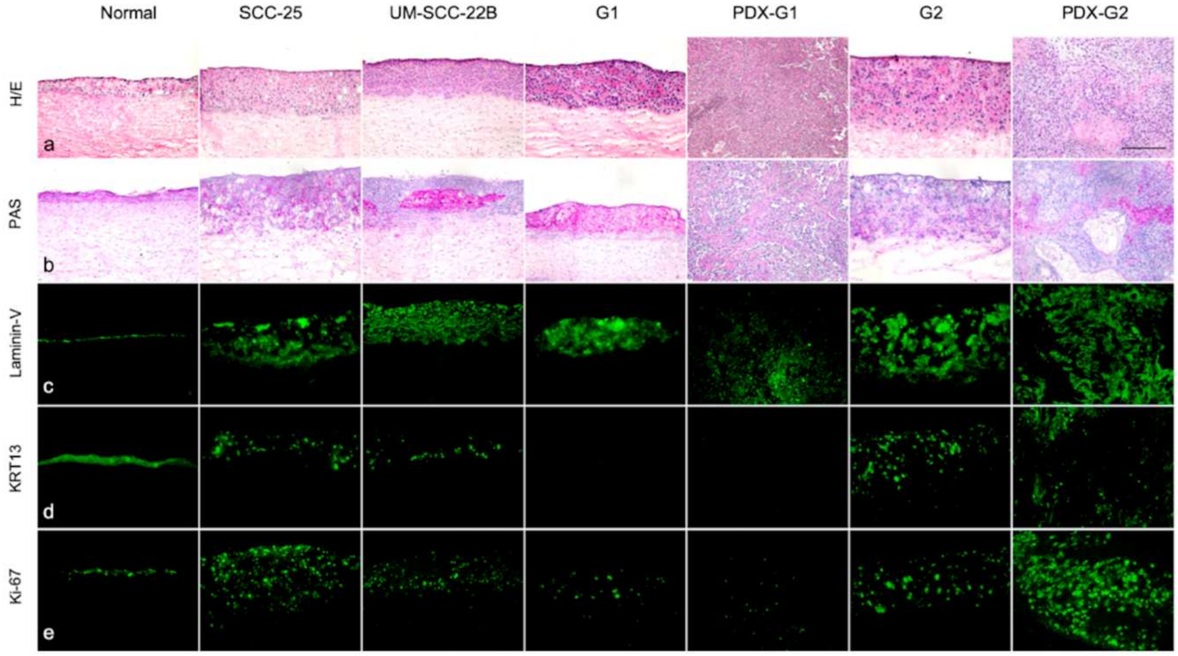

Fig. 2. Morphology of untreated NOM and HNSCC models. Models were cultured with human oral keratinocytes (normal), tumor cell lines (SCC-25 and UM-SCC-22B), primary tumors (G1, G2). For comparison, patient-derived xenografts (PDX-G1, PDX-G2) were characterized before integration into HNSCC models. **(a)** Hematoxylin/eosin (H/E) and **(b)** Periodic acid-Schiff (PAS) staining. Immunolocalization (green) of **(c)** laminin-V, **(d)** cytokeratin-13 (KRT13), **(e)** Ki-67. Images were representative of one to four batches; scale bar = 250 μm. (For interpretation of the references to color in this figure legend, the reader is referred to the Web version of this article.)

(Thermo Fisher Scientific). The CytoTox-ONE homogeneous membrane integrity assay (Promega; Mannheim, Germany) served to quantify lactate dehydrogenase (LDH) secretion. Both analyses were performed using the Optima FluoStar (BMG Labtech; Ortenberg, Germany).

2.9. Fluorescence lifetime imaging microscopy (FLIM)

Cetuximab fluorescence labeling. Cetuximab was labeled with fluorescein isothiocyanate (FITC) yielding cetuximab-FITC. Isothiocyanate reacts with amines to form a stable thiourea linkage [23]. As proteins contain primary amines such as the ε-amino group of lysines, protein fluorescence labeling via isothiocyanates emerged as common protein stain in microscopic experiments [56]. Cetuximab contains 23 lysines from which about 75% are surface exposed and therefore expected to be accessible to fluorescein isothiocyanate (FITC). For the labeling, 1.7 mM FITC was added to 17 μM cetuximab and allowed to incubate for 60 min in 100 mM sodium bicarbonate buffer pH 9.5. Excess dye was removed by gel chromatography with Sephadex G25. Labeling stoichiometry was determined to 6 FITC/cetuximab with UV–Vis spectroscopy. For this, the absorbance spectrum of the unlabeled cetuximab $A_{(280\ \mathrm{nm})\mathrm{cetuximab}}$ is subtracted from the spectrum of the FITC-labeled cetuximab $A_{(280\ \mathrm{nm})\ \mathrm{cetuximab\text{-}FITC}}$ at the maximum wavelength of fluorescein (~500 nm). The extinction coefficient $\varepsilon_{\mathrm{FITC}} = 73{,}000\ \mathrm{M}^{-1}\mathrm{cm}^{-1}$ of FITC at the respective wavelength is used for normalization. Division by the absorbance of cetuximab at 280 nm, normalized to the corresponding extinction coefficient $\varepsilon_{\mathrm{Cetuximab}} = 200{,}583\ \mathrm{M}^{-1}\mathrm{cm}^{-1}$ of cetuximab, yields the molar ratio FITC/cetuximab. Membrane binding of cetuximab-FITC was verified in cell monolayers of SCC-25 cells.

FLIM measurements. Cetuximab-FITC was applied to multi-layered SCC-25 and UM-SCC-22B models for 48 h, either systemically or topically. The models were snap-frozen and cut into 7 μm slices by a cryotome (Leica CM 1510 S). Cryosections were subjected to FLIM and measured with a home-built FLIM setup using time-correlated single-photon counting (TCSPC) [20,21]. A super continuum white-light laser source (NKT SuperK Extreme EXU-3, NKT Photonics; Birkerød, Denmark) generated ps pulses (65 ps FWHM) with a repetition rate of 19.5 MHz. An acousto-optical tunable filter (AOTF, UV-VIS Select, NKT Photonics) selected a narrow (4.6 nm) spectral band at 530 nm to excite the fluorophore FITC. The laser beam was scanned (DCS-120, Becker&Hickl; Berlin, Germany) and focused onto the sample by a 20x or 60x objective (Plan N, Olympus; Tokio, Japan) mounted into an inverted microscope (I×71, Olympus). A hybrid PMT detector (HPM-100-40, Becker & Hickl) detected the filtered emission (545 nm longpass, BrightLine HC, Semrock; Rochester, NY, USA) of cryosections. The collected photons were sorted into 1024 time channels (width 19.5 ps) by TCSPC modules (SPC-160, Becker & Hickl). FLIM data were analyzed using a self-written C++ routine, which sorted pixel into clusters according to their fluorescence decay based on a multivariate pattern recognition method. Clusters were used to generate fluorescence lifetime signatures (FLS), and pixels were colored according to the respective FLS to yield false-color images [22,23].

2.10. Statistical analysis

Data are presented as the mean ± standard deviation (SD) obtained from at least three independent experiments. Statistical analysis was performed using two-way ANOVA, a level of $p \leq 0.05$ was considered to indicate statistical significance (explorative data analysis).

3. Results

3.1. Model characterization

Human tumor cells from different sources reproducibly proliferated in the multi-layered TOM models. The protocols for TOM and NOM models were optimized for a total cultivation time of 21 days (Fig. 1a) since the maximum epithelial thickness was reached at this time point (Figure S1). The multi-layered TOM models preserved the patients' tumor morphology according to the pathologist's evaluation (P.J.). NOM models reflected non-keratinized, lining oral mucosa, consisting of a basal layer with rounded cells and multiple layers of spinous cells as well as abundant cytokeratin-13 (KRT13) expression (Fig. 2).

Moreover, normal morphology was reflected by a thin line of laminin-V between the basal layer and the lamina propria. In contrast, all TOM models depicted an unstructured, hyperproliferative, and thickened epithelial layer with reduced KRT13 and clustered laminin-V expression. The SCC-25 models showed a heterogeneous glycogen distribution, whereas large glycogen clusters were observed in UM-SCC-22B models (Fig. 2b). The G2 tumor model appeared more aggressive than the G1-graded tumor model, as seen in epithelial thickness, pleomorphism, proliferation rate, and laminin-V distribution, reflecting the clinical grading of the patient's tumor. Since the TOM models lacked a distinct basal membrane, we did not classify tumor cell detachment from the epithelial layer (Fig. 2b, G2) as an invasive phenotype. Nevertheless, single tumor cells also separated from the epithelial layer in the SCC-25 model and even more pronounced in the UM-SCC-22B model.

Using the expression of hypoxia-inducible factor (HIF)-1α and vascular endothelial growth factor (VEGF) as surrogate markers of hypoxia, we demonstrated the presence of an oxygen gradient within the TOM models (Figure S2). HIF-1α expression peaked in the apical part of the tumor layer, decreased in the transition zone and was undetectable in the lower parts of the lamina propria, whereas the VEGF expression was most pronounced at the invasion front of the tumor.

3.2. *Efficacy of topical docetaxel treatment in TOM models*

We next determined the effects of docetaxel on tumor size, proliferation, and cell death in TOM and NOM models in a vehicle-controlled study. Three doses of the drug were applied, either by administering the drug solution on the tissue surface (topical) or by supplementing the culture medium (systemic). Four different docetaxel concentrations in the range of clinically observed plasma levels following systemic exposure were selected. In TOM models derived from cell lines, both topical and systemic treatment with docetaxel resulted in a dose-dependent reduction in tumor size, however, lower doses of the topically applied drug were required for the same magnitude of effects (Fig. 3, S3).

Treatment with vehicle control did neither affect the morphology of NOM nor TOM models. Furthermore, docetaxel did not change the morphology of NOM models (Fig. 4, S4).

Docetaxel treatment resulted in abundant epithelial cell death and reduced epithelial thickness (Fig. 3). Moreover, the expression of the basal membrane marker laminin-V appeared more clustered, while HIF-1α expression and the proliferation index (determined by the number of Ki-67 positive cells) decreased (Fig. 5, S5). Lactate dehydrogenase (LDH) release and the portion of apoptotic cells significantly increased which confirmed induction of cell death by docetaxel treatment (Fig. 5). Moreover, interleukin-(IL)-6 release was enhanced. LDH and IL-6 release peaked following two applications of docetaxel on day 18 (Figure S6). Immunofluorescence staining of tissue identified the tumor stroma as a major source of docetaxel-induced IL-6 in the culture medium (Figure S7).

Although the maximum docetaxel effect was similar in both cell line-derived TOM models, SCC-25 models showed effects at lower docetaxel

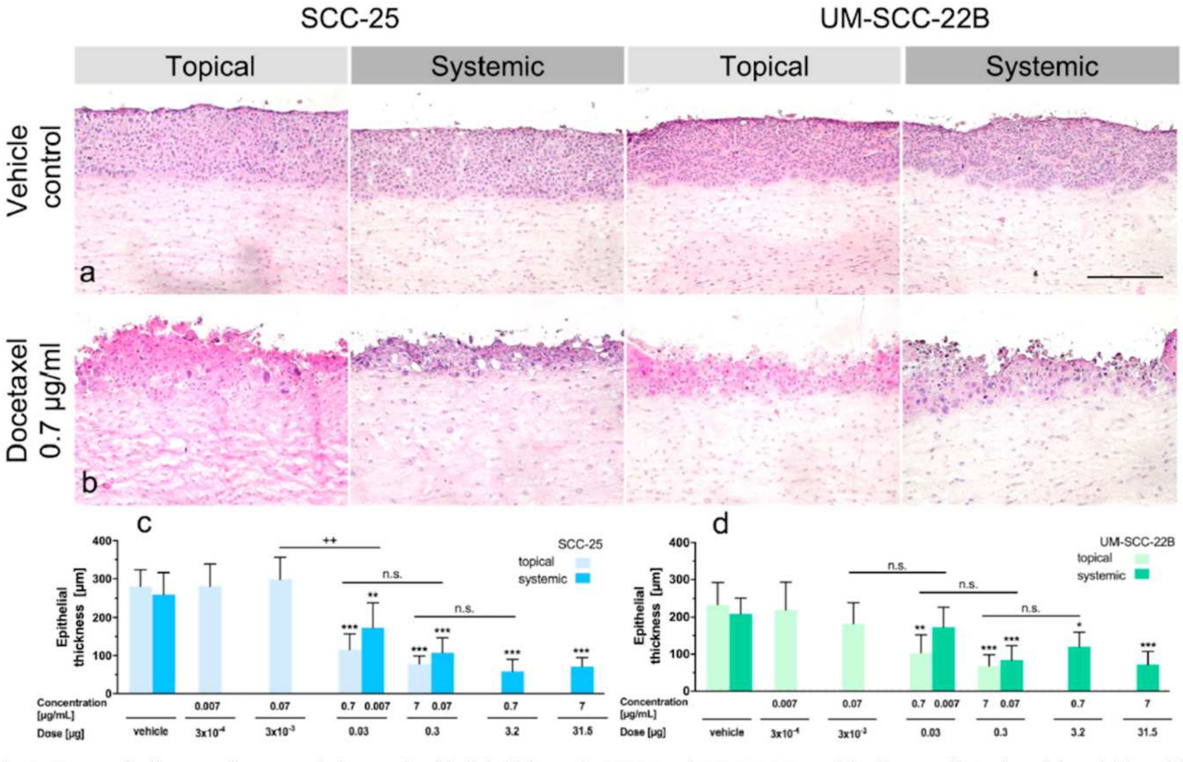

Fig. 3. Docetaxel effects on tissue morphology and epithelial thickness in SCC-25 and UM-SCC-22B models. Hematoxylin/eosin staining of (a) models following vehicle control and (b) 0.7 µg/mL docetaxel treatment. Epithelial thickness post-treatment in (c) SCC-25 and (d) UM-SCC-22B models. Images and data were representative of at least three batches; scale bar = 250 µm; mean + SD; $^{++}p \leq 0.01$, $^{n.s.}p > 0.05$ compared to 10-fold lower dose; $^{*}p \leq 0.05$, $^{**}p \leq 0.01$, $^{***}p \leq 0.001$ compared to vehicle control. (For interpretation of the references to color in this figure legend, the reader is referred to the Web version of this article.)

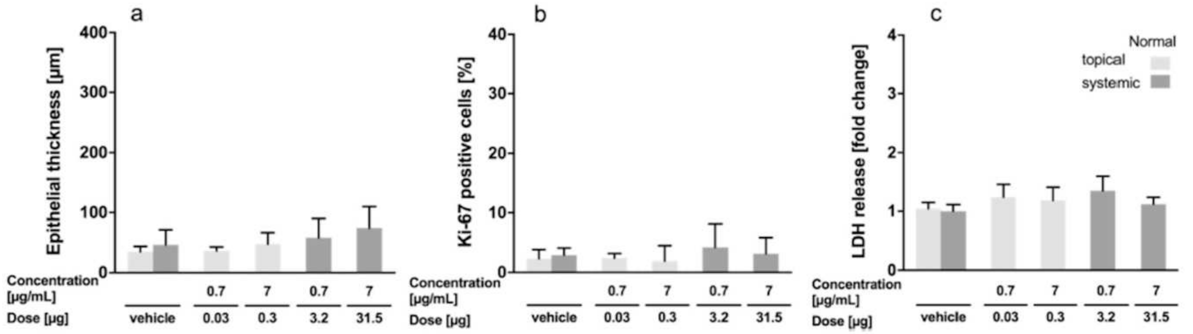

Fig. 4. Docetaxel effects on NOM models. (a) The epithelial thickness and (b) fraction of Ki-67 positive cells at the end of the culture. (c) Lactate dehydrogenase (LDH) release on day 18 normalized to untreated NOM models before treatment. Data are representative of at least three batches and presented as mean + SD.

doses than UM-SCC-22B models concerning epithelial thickness, laminin-V clustering, HIF-1α expression, proliferation, and LDH release. Due to the lower IL-6 baseline levels, responses in the UM-SCC-22B models were more pronounced than in SCC-25 models, with an up to 36-fold increase following docetaxel treatment.

The topical treatment achieved the same effects as the systemic treatment but mostly required a 10-times lower drug dose. For example, a similar reduction in proliferation was observed when applying 0.03 µg (0.7 µg/mL) docetaxel topically or 0.3 µg (0.07 µg/mL) docetaxel systemically (Table 1, Fig. 5a and b).

3.3. *Cetuximab resistance in TOM models*

We then evaluated the effects of cetuximab, representing a challenge for topical drug administration due to its high molecular size. First analysis in monolayer cultures revealed UM-SCC-22B cells to be more sensitive than SCC-25 cells (Fig. 6a).

In the TOM models, even five systemic applications of 100 µg/mL cetuximab resulted in only minor changes of epithelial thickness in UM-SCC-22B models (−31%), but no reduction occurred in SCC-25 models (Fig. 6b). A high proliferation index (Fig. 6c) at the end of the culture period together with high numbers of laminin-V clusters (Figure S8) indicated the selection of cetuximab-resistant tumor cells.

To understand the mechanism of decreased cetuximab efficacy in TOM models compared to the respective monolayer cultures, we next studied the penetration of cetuximab into SCC-25 models by Cluster-FLIM, allowing to quantify drug penetration (Fig. 7) and discrimination from background fluorescence [23,24]. The first inspection of the penetration profiles at a magnification of 20x (Fig. 7a–e) revealed homogeneous but low drug penetration at a dose of 10 µg/mL. At 100 µg/mL, however, a clear difference in the availability of the drug was seen between topical and systemic treatment (Fig. 7b,e). According to the corresponding penetration profiles (gray area as the sum of total fluorescence counts), a factor of about two-fold higher penetration was found for the epithelial layer and a factor of ~ 7-fold in the lamina propria at systemic application. Since Cluster-FLIM allows discrimination between different environments of the labeled drug at a dose of 100 µg/mL in the tissue [25], we analyzed the FLIM clusters at a magnification of 60x (Fig. 7g and h). Among the three FLIM cluster (colored red, cyan, and yellow) we identified a fluorescence lifetime signature (yellow-colored curve in Fig. 7f) that was unique at 48 h exposure times in the epithelial layer and did not overlap with autofluorescence contribution to the cyan and red FLIM cluster (Fig. 7b,g). Thus, based on the spatial localization of the yellow FLIM cluster, we assign this cluster to cetuximab cell interactions. The yellow fluorescence lifetime signature resembled closely the cetuximab-FITC fluorescence lifetime signature in SCC-25 cell monolayers (Fig. 7i). We noted that the amount of these cellular interactions, i.e. yellow cluster, did not vary much between topical and systemic interactions in the upper epithelial layer (Fig. 7b,e). To further investigate cellular effects in UM-SCC-22B models, we compared the dose-dependency at systemic application (Fig. 7j and k). Similar to SCC-25 we found an increase at a higher dose for both penetration (cyan cluster) and cell interaction (yellow cluster, Fig. 7j–l). Taken together, cetuximab was only effective in cell monolayers despite reaching tumor cells in the TOM models at topical or systemic administration.

4. Discussion

We here present a novel multi-layered HNSCC model, showing large similarities in morphology, grading, and protein expression profiles to patients' tumors. We could demonstrate that these models will not only be useful for comprehensive molecular and functional analysis of tumor cell resistance to small pharmacological agents like docetaxel but also antibodies of large molecular weight, a class of therapeutics for which limitations in drug penetration and target cell binding have previously been reported for tumor xenografts and 3D models [26,27].

Multi-layered mucosa models comprise several advantages over currently existing preclinical test systems. Beside matching the morphology of human mucosa they display tissue polarity, a feature found to significantly impact on drug efficacy due to more physiological gradients of nutrients and oxygen [8]. The analysis of glycogen confirmed tissue polarity in the TOM models, which was however lost in models from less differentiated tumors. The altered glucose metabolism in TOM compared to NOM models is in accordance with large quantities of glycogen in breast, kidney, uterus, bladder, ovary, skin and brain cancer cells [28]. Among other factors, HIF-1α can mediate glycogen accumulation [29], pointing to a potential causal relationship between the observed oxygen gradient and the glycogen distribution patterns in the TOM models.

Multi-layered mucosa models have also been shown to outperform monolayer cultures as models for studying the complex processes involved in carcinogenesis [30–32]. We could demonstrate that multi-layered mucosa models of oral cancer show important features of patients' tumors, including increased epithelial thickness, abundant pleomorphism, elevated proliferation rate, and abnormal expression of laminin-V [33–35]. We also showed that these features can be used as surrogate efficacy measures for *in vitro* evaluation of drugs. An additional advantage of the model is the possibility of studying tumor stroma interactions, under steady-state and treatment conditions. We observed relatively high basal IL-6 levels, which have also been previously reported for co-cultures of fibroblasts and tumor cells [36]. The increase in IL-6 production after docetaxel treatment was mainly driven by the stromal compartment and the fold-change in IL-6 expression was comparable to clinical observations [37]. Elevated IL-6 levels are known to contribute to cell migration, invasion, and tumor cell survival via the

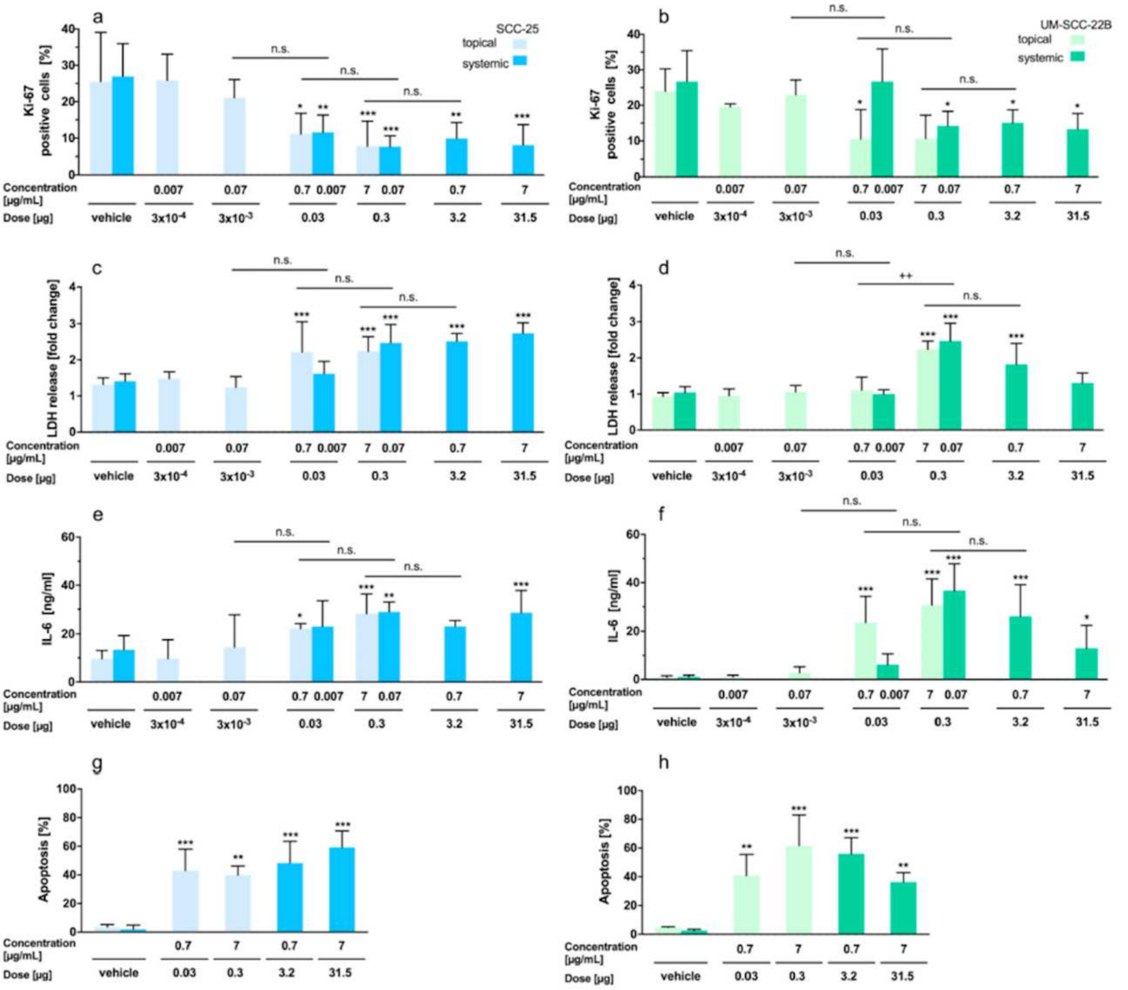

Fig. 5. Docetaxel effects on proliferation, cell death, and inflammation in SCC-25 (a, c, e, g) and UM-SCC-22B (b, d, f, h) models. (a, b) The rate of proliferative, Ki-67 positive cells at the end of the culture. (c, d) Lactate dehydrogenase (LDH) release on day 18 normalized to untreated NOM models before treatment. (e, f) Interleukin-6 (IL-6) release on day 18. (g, h) The fraction of apoptotic cells (TUNEL assay) at the end of the culture. Data are representative of at least three batches and presented as mean + SD; $^{++}p \le 0.01$, $^{\text{n. s.}}p > 0.05$ compared to 10-fold lower dose; $^{*}p \le 0.05$, $^{**}p \le 0.01$, $^{***}p \le 0.001$ compared to vehicle control. (For interpretation of the references to color in this figure legend, the reader is referred to the Web version of this article.)

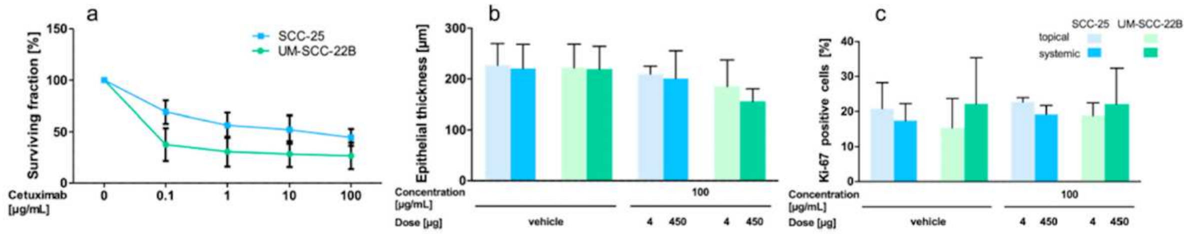

Fig. 6. Cetuximab effects in SCC-25 and UM-SCC22B cells and models. (a) Surviving fraction of SCC-25 cells and UM-SCC-22B cells in monolayer experiments. (b) The epithelial thickness and (c) percentage of proliferative, Ki-67 positive cells in SCC-25 and UM-SCC-22B models at the end of the culture. Data are representative of at least two batches and presented as mean +SD. (For interpretation of the references to color in this figure legend, the reader is referred to the Web version of this article.)

L. Gronbach et al. *Biomaterials 258 (2020) 120277*

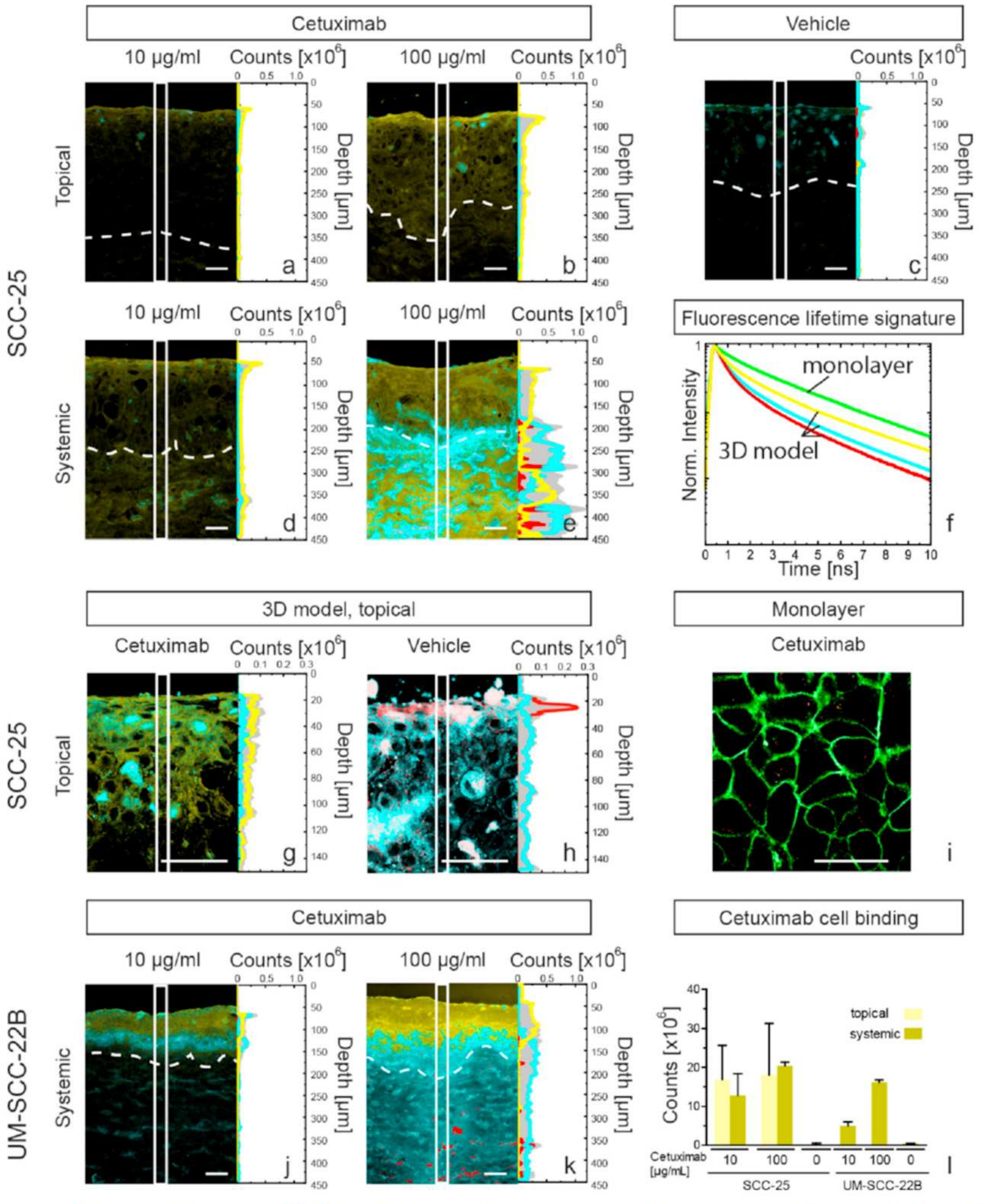

Fig. 7. Cetuximab penetration into SCC-25 and UM-SCC-22B models and cell interaction. Cluster-FLIM images of cetuximab-FITC treated SCC-25 (a, b, d, e) and UM-SCC-22B (j, k) models as well as vehicle sample (c) after 48 h exposure. Penetration profiles (from the white ROI in the images) are given at the right side of the images. Gray is the total intensity in the profiles; the individual FLIM-cluster intensities according to the color of the fluorescence lifetime signatures (f) are given. False-color coding of the images is also according to the color of the fluorescence lifetime signatures. (g–i) Comparison between cell monolayer and tissue experiments at a concentration of 100 µg/mL (model) and 50 µg/mL (monolayer). (l) Quantification of the unique yellow-colored FLIM cluster of cetuximab-FITC in the epithelial layer is quantified. Scale bar = 50 µm. Experimental conditions: objective 20x (a, b, c, d, e, j, k): $\lambda_{ex} = 488$ nm, $\lambda_{em} > 515$ nm, 300 s integration, pinhole = 0.5 ariy units and objective 60x (g, h, i): $\lambda_{ex} = 488$ nm, $\lambda_{em} > 515$ nm, 300 s integration, pinhole = 0.25 ariy units. (For interpretation of the references to color in this figure legend, the reader is referred to the Web version of this article.)

PI3K/Akt pathway and thus to drug resistance [37,38]. Moreover, high levels of IL-6 impair activation of antigen-specific T cells [39].

To date, current topical applications in the oral cavity include mucoadhesive hydro-/oleagels, patches, adhesive tablets, orodispersible films, and electrospinning of ultrathin fibers to treat canker sores and oral thrush [9,10]. Furthermore, nanoparticles or mucolytic enzyme decorated carrier systems have been developed to improve the mucus permeation [40]. However, despite its expectedly favorable toxicity profile, topical cancer treatment remains the exception. It is currently used in skin cancer where it removes the widespread atypical keratinocytes in field-cancerization [41]. Although HNSCC patients also suffer from field-cancerization [42,43] and might also profit from a topical treatment, it has not yet been introduced in HNSCC therapy [44]. The observed effects of low-dose docetaxel in TOM models following topical treatment indicate effectiveness of this administration route in HNSCC. Moreover, the lack of local adverse reactions in NOM models suggests a safe use. Equal efficacy at lower drug doses would significantly diminish systemic side effects of current drug treatment in HNSCC. Dose-limiting neutropenia and further hematologic adverse events causing discontinuation of systemic treatment regimens with taxanes [45] could be avoided by their topical application. While the saliva wash-out might depict one major challenge for this administration route, the generally weakened mucus production in HNSCC patients should guarantee sufficient drug penetration into the tumor lesion. Radiotherapy further decreases salivation [46] which should additionally reduce the natural barrier function of saliva for drug uptake into the oral mucosa. Based on our findings of similar extent of cetuximab binding to tumor cells following topical and systemic drug administration, topical therapy could also be interesting for high-molecular-weight drugs such as monoclonal antibodies.

In line with the clinical observation of modest anti-tumor effects of cetuximab monotherapy in advanced HNSCC patients [47], small inhibitory effects of cetuximab treatment was observed in the cell-line derived TOM models while it significantly inhibited cell proliferation in monolayer cultures. Although similar observations have previously been reported from comparative analyses of 2D and 3D models [48,49], the underlying mechanisms are not yet fully understood. Altered expression of genes related to apoptotic and proteostasis [50] and reorganization of the extracellular matrix [51] might be possible explanations for drug resistance in 3D compared to 2D cultures [52]. Increased HER3/IGF1R and heregulin signaling [53] as well as altered tumor-specific processing of laminin-V and subsequent activation of EGFR [54] might also interfere with drug efficacy in TOM models recapitulating tumor-microenvironment interactions. Certainly, future studies in TOM models will be required to address these unresolved questions.

In this pilot study, we only included cell-line derived TOM models in our drug screening assays since large numbers of cells were necessary for optimization of the experimental settings. The drug screening approach can also be extended to models derived from primary patient material. However, this will require a further miniaturization of the *ex vivo* cultures, in order to reduce the number of tumor cells needed for each individual test well. Even small-scale drug screening tests would require at least 10 model replicas for different drug concentrations, vehicle control and untreated control. This equals to at least two million cells per patient in the described setting. Strategies of model optimization and miniaturization will be evaluated in future studies, in order to generate TOM models from fresh surgical tumor material of patients with non-resectable tumors where only small tumor biopsies will be available. Since TOM models can be generated within a few weeks, they could serve as individual test system for drug screening as basis for individualized therapy recommendations. Future incorporation of other important microenvironment components such as cancer-associated fibroblasts and immune cells might further improve the informative value of the TOM model. Moreover, the use of advanced extracellular matrices could allow extended culture periods of TOM models with the possibility to study the long-term effects of drugs [55].

In conclusion, we established a novel HNSCC model for studying uptake, distribution and anti-tumor efficacy of drugs as well as the biological processes involved in drug resistance. We present first evidence that topical docetaxel application might represent a promising option for improving efficiency and reducing side effects in HNSCC therapy. Future studies in larger numbers of patient-derived oral mucosa as well as orthotopic xenograft models are warranted to confirm these interesting findings.

CRediT authorship contribution statement

Leonie Gronbach: Conceptualization, Investigation, Visualization, Writing - original draft, Writing - review & editing. **Christopher Wolff:** Conceptualization, Writing - original draft. **Konrad Klinghammer:** Investigation. **Johannes Stellmacher:** Investigation, Visualization, Writing - original draft. **Philipp Jurmeister:** Investigation. **Ulrike Alexiev:** Investigation, Visualization, Writing - original draft, Writing - review & editing. **Monika Schäfer-Korting:** Funding acquisition, Writing - original draft, Writing - review & editing. **Ingeborg Tinhofer:** Investigation, Writing - original draft, Writing - review & editing. **Ulrich Keilholz:** Conceptualization, Funding acquisition, Supervision, Writing - review & editing. **Christian Zoschke:** Conceptualization, Investigation, Project administration, Supervision, Visualization, Writing - original draft, Writing - review & editing.

Declaration of competing interest

The authors declare that they have no known competing financial interests or personal relationships that could have appeared to influence the work reported in this paper.

Acknowledgments

This work was supported by the German Federal Ministry of Education and Research (Berlin-Brandenburg research platform BB3R [grant number 031A262A]). The authors highly appreciated the excellent technical assistance of Jill García Miller.

Appendix A. Supplementary data

Supplementary data to this article can be found online at https://doi.org/10.1016/j.biomaterials.2020.120277.

Data availability

The raw and processed data required to reproduce these findings are available from the corresponding author on reasonable request.

References

[1] F. Bray, J. Ferlay, I. Soerjomataram, R.L. Siegel, L.A. Torre, A. Jemal, Global cancer statistics 2018: globocan estimates of incidence and mortality worldwide for 36 cancers in 185 countries, Ca - Cancer J. Clin. 68 (2018) 394–424.
[2] R.L. Siegel, K.D. Miller, A. Jemal, Cancer statistics, Ca - Cancer J. Clin. 69 (2019) 7–34.
[3] E. Alsahafi, K. Begg, I. Amelio, N. Raulf, P. Lucarelli, T. Sauter, M. Tavassoli, Clinical update on head and neck cancer: molecular biology and ongoing challenges, Cell Death Dis. 10 (2019) 540.
[4] T.S. Nowicki, S. Hu-Lieskovan, A. Ribas, Mechanisms of resistance to pd-1 and pd-l1 blockade, Canc. J. 24 (2018) 47–53.
[5] C.H. Wong, K.W. Siah, A.W. Lo, Estimation of clinical trial success rates and related parameters, Biostatistics 20 (2019) 273–286.
[6] J. Bailey, M. Thew, M. Balls, An analysis of the use of animal models in predicting human toxicology and drug safety, Altern Lab Anim 42 (2014) 181–199.
[7] S.A. Langhans, Three-dimensional in vitro cell culture models in drug discovery and drug repositioning, Front. Pharmacol. 9 (2018) 6.
[8] S.A. Lelièvre, T. Kwok, S. Chittiboyina, Architecture in 3d cell culture: an essential feature for in vitro toxicology, Toxicol. Vitro 45 (2017) 287–295.

[9] V. Hearnden, V. Sankar, K. Hull, D.V. Juras, M. Greenberg, A.R. Kerr, P. B. Lockhart, L.L. Patton, S. Porter, M.H. Thornhill, New developments and opportunities in oral mucosal drug delivery for local and systemic disease, Adv. Drug Deliv. Rev. 64 (2012) 16–28.

[10] A. Greiner, J.H. Wendorff, Electrospinning: a fascinating method for the preparation of ultrathin fibers, Angew Chem. Int. Ed. Engl. 46 (2007) 5670–5703.

[11] J.G. Rheinwald, M.A. Beckett, Tumorigenic keratinocyte lines requiring anchorage and fibroblast support cultured from human squamous cell carcinomas, Int. J. Canc. 41 (1981) 1657–1663.

[12] J.C. Brenner, M.P. Graham, B. Kumar, L.M. Saunders, R. Kupfer, R.H. Lyons, C. R. Bradford, T.E. Carey, Genotyping of 73 um-scc head and neck squamous cell carcinoma cell lines, Head Neck 32 (2010) 417–426.

[13] K. Klinghammer, J.-D. Raguse, T. Plath, A.E. Albers, K. Joehrens, A. Zakarneh, B. Brzezicha, A. Wulf-Goldenberg, U. Keilholz, J. Hoffmann, I. Fichtner, A comprehensively characterized large panel of head and neck cancer patient-derived xenografts identifies the mtor inhibitor everolimus as potential new treatment option, Int. J. Canc. 136 (2015) 2940–2948.

[14] P. Artimo, M. Jonnalagedda, K. Arnold, D. Baratin, G. Csardi, E. de Castro, S. Duvaud, V. Flegel, A. Fortier, E. Gasteiger, A. Grosdidier, C. Hernandez, V. Ioannidis, D. Kuznetsov, R. Liechti, S. Moretti, K. Mostaguir, N. Redaschi, G. Rossier, I. Xenarios, H. Stockinger, Expasy: sib bioinformatics resource portal, Nucleic Acids Res. 40 (2012) W597–W603.

[15] Europene Medicines Agency, European public assessment report "taxotere", annex l - summary of product [cited 2020/02/02], 2019.

[16] Europene Medicines Agency, European public assessment report "erbitux", annex l - summary of product characteristics [cited 2020/02/02], 2019.

[17] S.D. Baker, M. Zhao, C.K.K. Lee, J. Verweij, Y. Zabelina, J.R. Brahmer, A.C. Wolff, A. Sparreboom, M.A. Carducci, Comparative pharmacokinetics of weekly and every-three-weeks docetaxel, Clin. Canc. Res. 10 (2004) 1976–1983.

[18] N. Azzopardi, T. Lecomte, D. Ternant, M. Boisdron-Celle, F. Piller, A. Morel, V. Gouilleux-Gruart, C. Vignault-Desvignes, H. Watier, E. Gamelin, G. Paintaud, Cetuximab pharmacokinetics influences progression-free survival of metastatic colorectal cancer patients, Clin. Canc. Res. 17 (2011) 6329–6337.

[19] C.A. Schneider, W.S. Rasband, K.W. Eliceiri, Nih image to imagej: 25 years of image analysis, Nat. Methods 9 (2012) 671–675.

[20] A. Boreham, T.Y. Kim, V. Spahn, C. Stein, L. Mundhenk, A.D. Gruber, R. Haag, P. Welker, K. Licha, U. Alexiev, Exploiting fluorescence lifetime plasticity in flim: target molecule localization in cells and tissues, ACS Med. Chem. Lett. 2 (2011) 724–728.

[21] P. Volz, R. Brodwolf, C. Zoschke, R. Haag, M. Schäfer-Korting, U. Alexiev, White-light supercontinuum laser-based multiple wavelength excitation for tcspc-flim of cutaneous nanocarrier uptake, Z. Phys. Chem. 232 (2018) 671–688.

[22] R. Brodwolf, P. Volz-Rakebrand, J. Stellmacher, C. Wolff, M. Unbehauen, R. Haag, M. Schäfer-Korting, C. Zoschke, U. Alexiev, Faster, sharper, more precise: automated cluster-flim in preclinical testing directly identifies the intracellular fate of theranostics in live cells and tissue, Theranostics 10 (2020) 6322–6336.

[23] P. Volz, P. Schilrreff, R. Brodwolf, C. Wolff, J. Stellmacher, J. Balke, M.J. Morilla, C. Zoschke, M. Schafer-Korting, U. Alexiev, Pitfalls in using fluorescence tagging of nanomaterials: tecto-dendrimers in skin tissue as investigated by cluster-flim, Ann. N. Y. Acad. Sci. 1405 (2017) 202–214.

[24] U. Alexiev, P. Volz, A. Boreham, R. Brodwolf, Time-resolved fluorescence microscopy (flim) as an analytical tool in skin nanomedicine, Eur. J. Pharm. Biopharm. 116 (2017) 111–124.

[25] A. Boreham, J. Pikkemaat, P. Volz, R. Brodwolf, C. Kuehne, K. Licha, R. Haag, J. Dernedde, U. Alexiev, Detecting and quantifying biomolecular interactions of a dendritic polyglycerol sulfate nanoparticle using fluorescence lifetime measurements, Molecules 21 (2016) 22.

[26] M. Schutte, T. Risch, N. Abdavi-Azar, K. Boehnke, D. Schumacher, M. Keil, R. Yildiriman, C. Jandrasits, T. Borodina, V. Amstislavskiy, C.L. Worth, C. Schweiger, S. Liebs, M. Lange, H.J. Warnatz, L.M. Butcher, J.E. Barrett, M. Sultan, C. Wierling, N. Golob-Schwarzl, S. Lax, S. Uranitsch, M. Becker, Y. Welte, J.L. Regan, M. Silvestrov, I. Kehler, A. Fusi, T. Kessler, R. Herwig, U. Landegren, D. Wienke, M. Nilsson, J.A. Velasco, P. Garin-Chesa, C. Reinhard, S. Beck, R. Schafer, C.R. Regenbrecht, D. Henderson, B. Lange, J. Haybaeck, U. Keilholz, J. Hoffmann, H. Lehrach, M.L. Yaspo, Molecular dissection of colorectal cancer in pre-clinical models identifies biomarkers predicting sensitivity to egfr inhibitors, Nat. Commun. 8 (2017) 14262.

[27] T. Magdeldin, V. López-Dávila, C. Villemant, G. Cameron, R. Drake, U. Cheema, M. Loizidou, The efficacy of cetuximab in a tissue-engineered three-dimensional in vitro model of colorectal cancer, J. Tissue Eng. 5 (2014) 1–9.

[28] M. Rousset, A. Zweibaum, J. Fogh, Presence of glycogen and growth-related variations in 58 cultured human tumor cell lines of various tissue origins, Canc. Res. 41 (1981) 1165–1170.

[29] J. Pelletier, G. Bellot, P. Gounon, S. Lacas-Gervais, J. Pouyssegur, N.M. Mazure, Glycogen synthesis is induced in hypoxia by the hypoxia-inducible factor and promotes cancer cell survival, Front Oncol 2 (2012) 18.

[30] M.M. Stevens, Toxicology: testing in the third dimension, Nat. Nanotechnol. 4 (2009) 342.

[31] K. Kim, R. Utoh, K. Ohashi, T. Kikuchi, T. Okano, Fabrication of functional 3d hepatic tissues with polarized hepatocytes by stacking endothelial cell sheets in vitro, J Tissue Eng Regen Med 11 (2017) 2071–2080.

[32] E. Brauchle, H. Johannsen, S. Nolan, S. Thude, K. Schenke-Layland, Design and analysis of a squamous cell carcinoma in vitro model system, Biomaterials 34 (2013) 7401–7407.

[33] S.Q. Ahmed, M. Junaid, S. Awan, M.M. Choudhary, M. Kazi, A. Masoom, H. U. Khan, Relationship of tumor thickness with neck node metastasis in buccal squamous cell carcinoma: an experience at a tertiary care hospital, Int. Arch. Otorhinolaryngol. 21 (2017) 265–269.

[34] T. Harada, M. Shinohara, S. Nakamura, M. Oka, An immunohistochemical study of the extracellular matrix in oral squamous cell carcinoma and its association with invasive and metastatic potential, Virchows Arch. 424 (1994) 257–266.

[35] S. Xie, Y. Liu, X. Qiao, R.-X. Hua, K. Wang, X.-F. Shan, Z.-G. Cai, What is the prognostic significance of ki-67 positivity in oral squamous cell carcinoma? J. Canc. 7 (2016) 758–767.

[36] M. Mirkeshavarz, M. Ganjibakhsh, P. Aminishakib, P. Farzaneh, N. Mahdavi, F. Vakhshiteh, A. Karimi, N.S. Gohari, F. Kamali, M.J. Kharazifard, S.A. Shahzadeh Fazeli, A. Nasimian, Interleukin-6 secreted by oral cancer- associated fibroblast accelerated vegf expression in tumor and stroma cells, Cell. Mol. Biol. 63 (2017) 131–136.

[37] A. Argiris, S.C. Lee, T. Feinstein, S. Thomas, B.F. Branstetter, R. Seethala, L. Wang, W. Gooding, J.R. Grandis, R.L. Ferris, Serum biomarkers as potential predictors of antitumor activity of cetuximab-containing therapy for locally advanced head and neck cancer, Oral Oncol. 47 (2011) 961–966.

[38] T. Jinno, S. Kawano, Y. Maruse, R. Matsubara, Y. Goto, T. Sakamoto, Y. Hashiguchi, N. Kaneko, H. Tanaka, R. Kitamura, T. Toyoshima, A. Jinno, M. Moriyama, K. Oobu, T. Kiyoshima, S. Nakamura, Increased expression of interleukin-6 predicts poor response to chemoradiotherapy and unfavorable prognosis in oral squamous cell carcinoma, Oncol. Rep. 33 (2015) 2161–2168.

[39] Y. Ohno, H. Kitamura, N. Takahashi, J. Ohtake, S. Kaneumi, K. Sumida, S. Homma, H. Kawamura, N. Minagawa, S. Shibasaki, A. Taketomi, Il-6 down-regulates hla class ii expression and il-12 production of human dendritic cells to impair activation of antigen-specific cd4(+) t cells, Cancer Immunol. Immunother. 65 (2016) 193–204.

[40] C. Menzel, A. Bernkop-Schnurch, Enzyme decorated drug carriers: targeted swords to cleave and overcome the mucus barrier, Adv. Drug Deliv. Rev. 124 (2018) 164–174.

[41] R.N. Werner, E. Stockfleth, S.M. Connolly, O. Correia, R. Erdmann, P. Foley, A. K. Gupta, A. Jacobs, H. Kerl, H.W. Lim, G. Martin, M. Paquet, D.M. Pariser, S. Rosumeck, H.J. Rowert-Huber, A. Sahota, O.P. Sangueza, S. Shumack, B. Sporbeck, N.A. Swanson, L. Torezan, A. Nast, Evidence- and consensus-based (s3) guidelines for the treatment of actinic keratosis - international league of dermatological societies in cooperation with the european dermatology forum, J. Eur. Acad. Dermatol. Venereol. : JEADV 11 (2015) 2069–2079.

[42] D.P. Slaughter, H.W. Southwick, W. Smejkal, Field cancerization in oral stratified squamous epithelium; clinical implications of multicentric origin, Cancer 6 (1953) 963–968.

[43] B.J. Braakhuis, M.P. Tabor, J.A. Kummer, C.R. Leemans, R.H. Brakenhoff, A genetic explanation of slaughter's concept of field cancerization: evidence and clinical implications, Int. J. Canc. 63 (2003) 1727–1730.

[44] F. Ketabat, M. Pundir, F. Mohabatpour, L. Lobanova, S. Koutsopoulos, L. Hadjiiski, X. Chen, P. Papagerakis, S. Papagerakis, Controlled drug delivery systems for oral cancer treatment-current status and future perspectives, Pharmaceutics 11 (2019) 302.

[45] M.R. Posner, D.M. Hershock, C.R. Blajman, E. Mickiewicz, E. Winquist, V. Gorbounova, S. Tjulandin, D.M. Shin, K. Cullen, T.J. Ervin, B.A. Murphy, L. E. Raez, R.B. Cohen, M. Spaulding, R.B. Tishler, B. Roth, R.d.C. Viroglio, V. Venkatesan, I. Romanov, S. Agarwala, K.W. Harter, M. Dugan, A. Cmelak, A. M. Markoe, P.W. Read, L. Steinbrenner, A.D. Colevas, C.M. Norris, R.I. Haddad, Cisplatin and fluorouracil alone or with docetaxel in head and neck cancer, N. Engl. J. Med. 357 (2007) 1705–1715.

[46] C. Scully, J.V. Bagan, Recent advances in oral oncology 2008; squamous cell carcinoma imaging, treatment, prognostication and treatment outcomes, Oral Oncol. 45 (2009) e25–30.

[47] J.B. Vermorken, J. Trigo, R. Hitt, P. Koralewski, E. Diaz-Rubio, F. Rolland, R. Knecht, N. Amellal, A. Schueler, J. Baselga, Open-label, uncontrolled, multicenter phase ii study to evaluate the efficacy and toxicity of cetuximab as a single agent in patients with recurrent and/or metastatic squamous cell carcinoma of the head and neck who failed to respond to platinum-based therapy, J. Clin. Oncol. 25 (2007) 2171–2177.

[48] V.S. Nirmalanandhan, A. Duren, P. Hendricks, G. Vielhauer, G.S. Sittampalam, Activity of anticancer agents in a three-dimensional cell culture model, Assay Drug Dev. Technol. 8 (2010) 581–590.

[49] C. Wolff, C. Zoschke, S.K. Kalangi, P. Reddanna, M. Schäfer-Korting, Tumor microenvironment determines drug efficacy in vitro - apoptotic and anti-inflammatory effects of 15-lipoxygenase metabolite, 13-hpotre, Eur. J. Pharm. Biopharm. 142 (2019) 1–7.

[50] C. Hausmann, C. Zoschke, C. Wolff, M.E. Darvin, M. Sochorová, A. Kováčik, B. Wanjiku, F. Schumacher, J. Tigges, B. Kleuser, J. Lademann, E. Fritsche, K. Vávrová, N. Ma, M. Schäfer-Korting, Fibroblast origin shapes tissue homeostasis, epidermal differentiation, and drug uptake, Sci. Rep. 9 (2019) 2913.

[51] P.P. Provenzano, K.W. Eliceiri, J.M. Campbell, D.R. Inman, J.G. White, P.J. Keely, Collagen reorganization at the tumor-stromal interface facilitates local invasion, BMC Med. 4 (2006) 38.

[52] S. Nallanthighal, J.P. Heiserman, D.-J. Cheon, The role of the extracellular matrix in cancer stemness, Front Cell Dev Biol 7 (2019).

[53] I. Kjaer, T. Lindsted, C. Frohlich, J.V. Olsen, I.D. Horak, M. Kragh, M.W. Pedersen, Cetuximab resistance in squamous carcinomas of the upper aerodigestive tract is driven by receptor tyrosine kinase plasticity: potential for mab mixtures, Mol. Canc. Therapeut. 15 (2016) 1614–1626.

L. Gronbach et al. *Biomaterials 258 (2020) 120277*

[54] M.P. Marinkovich, Tumour microenvironment: laminin 332 in squamous-cell carcinoma, Nat. Rev. Canc. 7 (2007) 370–380.

[55] H.J. Stark, K. Boehnke, N. Mirancea, M.J. Willhauck, A. Pavesio, N.E. Fusenig, P. Boukamp, Epidermal homeostasis in long-term scaffold-enforced skin equivalents, J. Invest. Dermatol. Symp. Proc. 11 (2006) 93–105.

[56] M Witting, A Boreham, R Brodwolf, K Vavrova, U Alexiev, WS. Hedtrich Friess, Interactions of hyaluronic acid with the skin and implications for the dermal delivery of biomacromolecules, Mol. Pharm. 12 (2015) 1391–1401.

-- Supplementary Information --

Leonie Gronbach[a], Christopher Wolff[a], Konrad Klinghammer[b], Johannes Stellmacher[c], Philipp Jurmeister[d], Ulrike Alexiev[c], Monika Schäfer-Korting[a], Ingeborg Tinhofer[e,f], Ulrich Keilholz[g], Christian Zoschke[a*]

[a] Freie Universität Berlin, Institute of Pharmacy (Pharmacology & Toxicology), Königin-Luise-Str. 2+4, 14195 Berlin, Germany

[b] Charité – Universitätsmedizin Berlin, corporate member of Freie Universität Berlin, Humboldt-Universität zu Berlin, and Berlin Institute of Health, Department of Hematology and Oncology, Charitéplatz 1, 10117 Berlin, Germany

[c] Freie Universität Berlin, Institute of Experimental Physics, Arnimallee 14, 14195 Berlin, Germany

[d] Charité – Universitätsmedizin Berlin, corporate member of Freie Universität Berlin, Humboldt-Universität zu Berlin, and Berlin Institute of Health, Institute of Pathology, Charitéplatz 1, 10117 Berlin, Germany

[e] Charité – Universitätsmedizin Berlin, corporate member of Freie Universität Berlin, Humboldt-Universität zu Berlin, and Berlin Institute of Health, Department of Radiooncology and Radiotherapy, Charitéplatz 1, 10117 Berlin, Germany

[f] German Cancer Research Center (DKFZ), Heidelberg and German Cancer Consortium (DKTK) Partner Site Berlin, Berlin, Germany

[g] Charité – Universitätsmedizin Berlin, corporate member of Freie Universität Berlin, Humboldt-Universität zu Berlin, and Berlin Institute of Health, Comprehensive Cancer Center, Charitéplatz 1, 10117 Berlin, Germany

* Corresponding author: Dr. Christian Zoschke;
Freie Universität Berlin, Institute of Pharmacy (Pharmacology & Toxicology),
Königin-Luise-Str. 2+4, 14195 Berlin, Germany
Phone: +49 30 838-56189; Fax: +49 30 838-456189

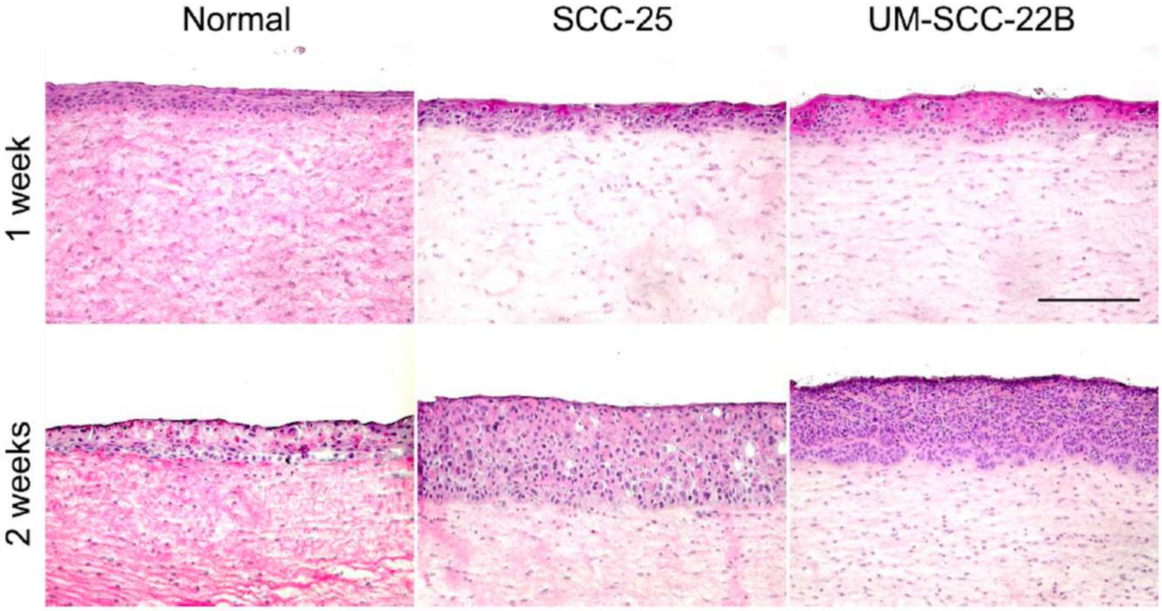

Supplementary Figure 1. Morphology of untreated NOM and TOM models over time. Morphology of models **(a)** one week (day 14) and **(b)** two weeks (day 21) after cell seeding. Images were representative of at least three batches; scale bar = 250 µm.

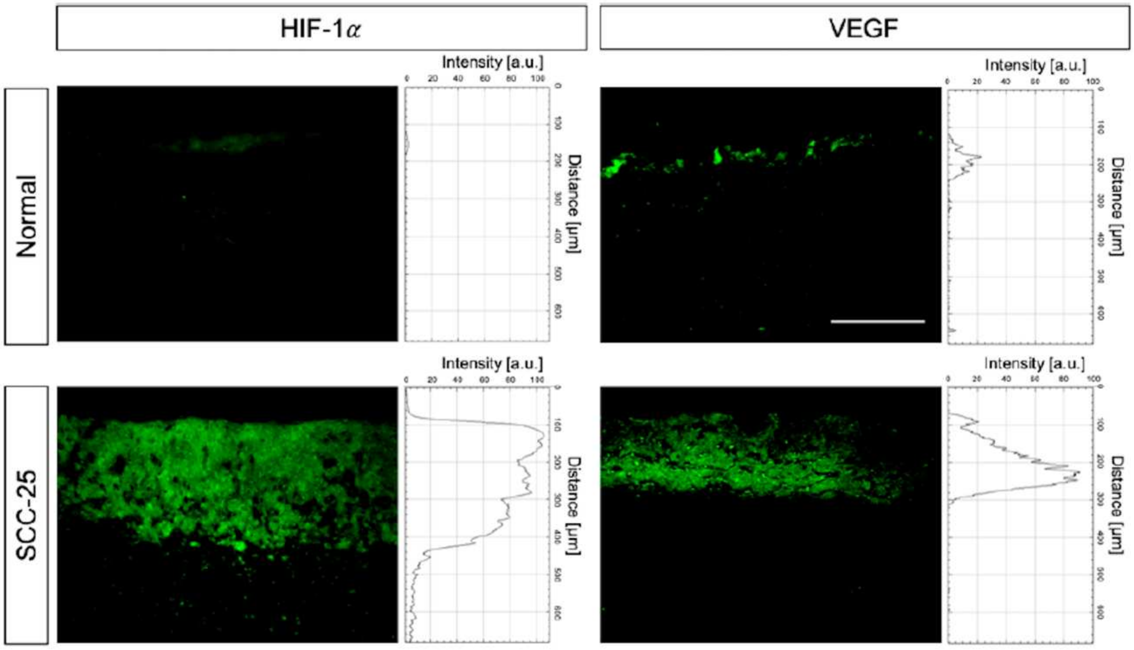

Supplementary Figure 2. Profile of hypoxia-inducible factor (HIF)-1α and vascular endothelial growth factor (VEGF) expression at day 21. Images were representative of three batches; scale bar = 250 µm.

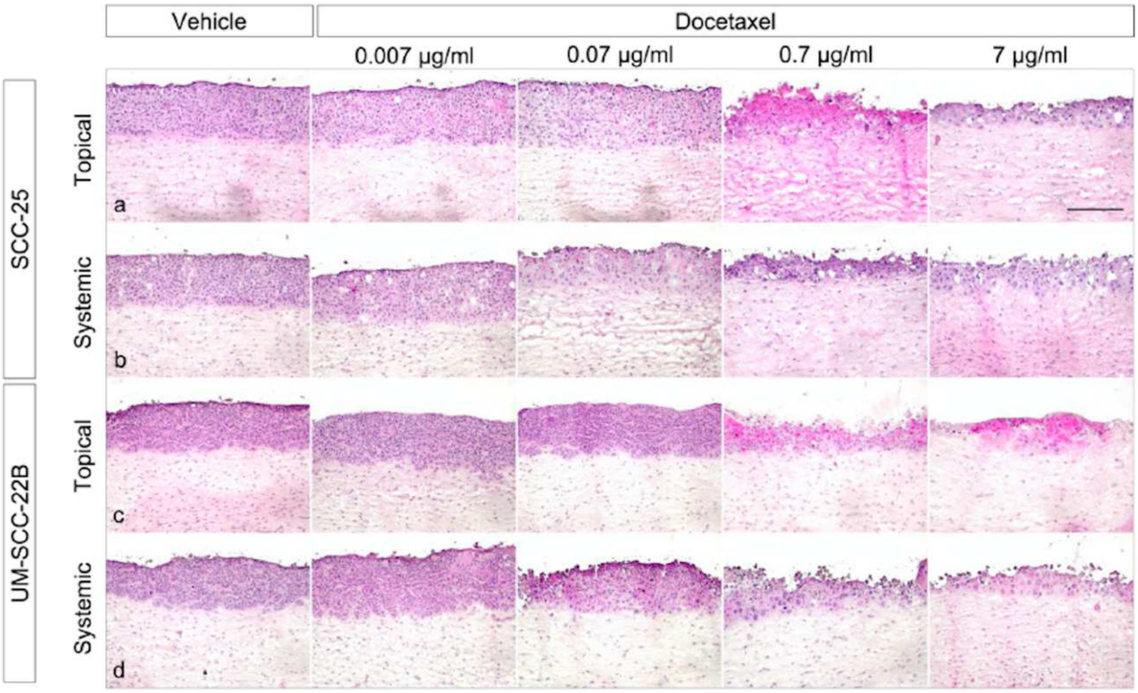

Supplementary Figure 3. Effects of different docetaxel concentrations on HNSCC models and cell monolayers. Morphology of **(a, b)** SCC-25 models and **(c, d)** UM-SCC-22B models following **(a, c)** topical and **(b, d)** systemic treatment. Images were representative of at least three batches; scale bar = 250 µm; for applied drug amounts refer to Table 1.

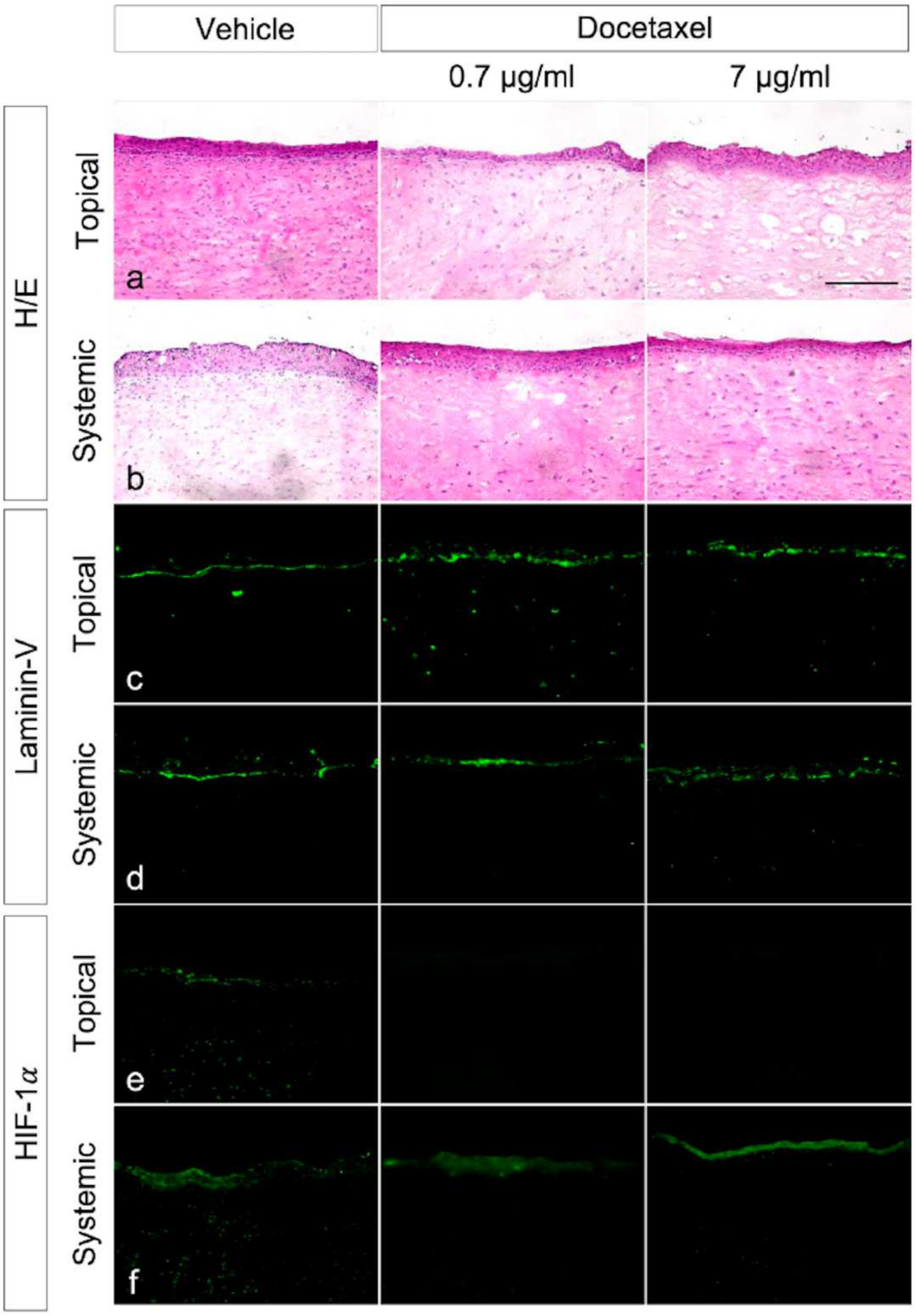

Supplementary Figure 4. Morphology of systemic and topical docetaxel treated NOM models. (a, b) Hematoxylin/eosin (H/E) staining. **(c, d)** Immunolocalization (green) of laminin-V and **(e, f)** HIF-1α following three times of 0.7 or 7 µg/ml docetaxel or vehicle control treatment. Images were representative of at least three batches; scale bar = 250 µm; for applied drug amounts refer to Table 1.

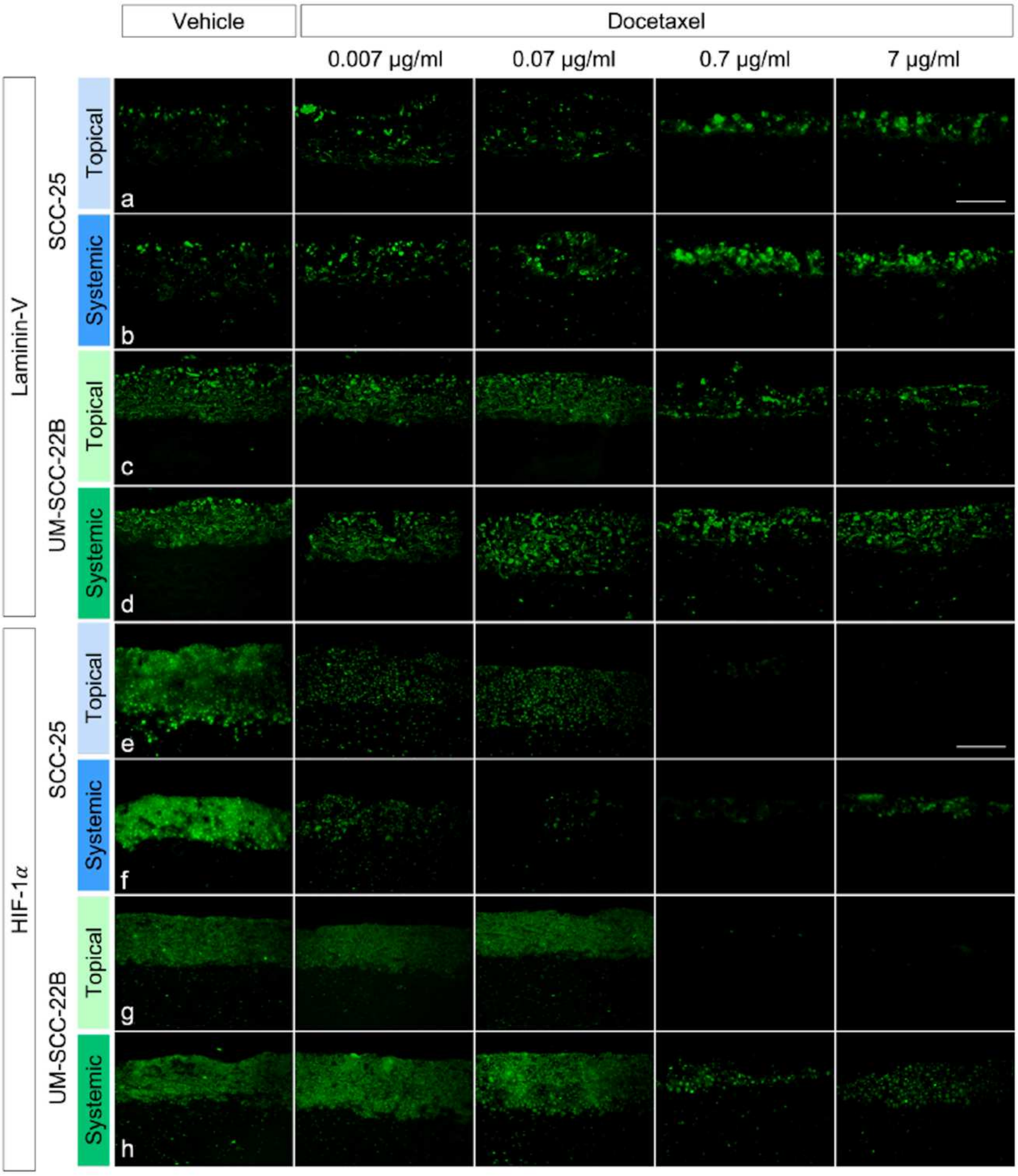

Supplementary Figure 5. Docetaxel effects on the protein expression involved in invasion and hypoxia in SCC-25 and UM-SCC-22B models. Immunolocalization (green) of **(a-d)** laminin-V and **(e-h)** HIF-1α following three times of 0.007 – 7 µg/ml docetaxel or vehicle control treatment. Images were representative of at least three batches; scale bar = 250 µm; for applied drug amounts refer to Table 1.

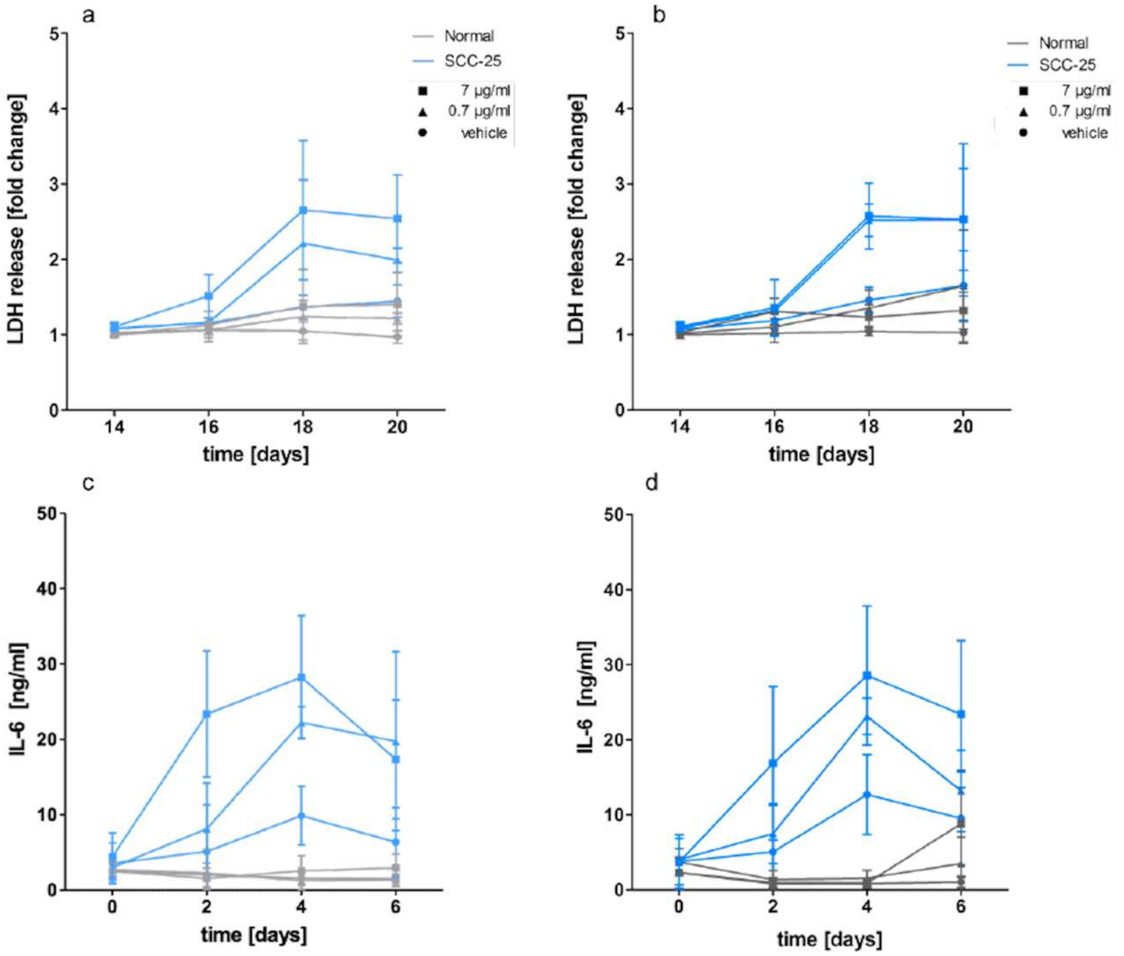

Supplementary Figure 6. Docetaxel effects over time of lactate dehydrogenase (LDH) and interleukin (IL)-6 release of normal (gray) and SCC-25 (blue) models. LDH release following **(a)** topical and **(b)** systemic docetaxel treatment. IL-6 release following **(c)** topical and **(d)** systemic docetaxel treatment. Data were representative of three batches and presented as mean ± SD; for applied drug amounts refer to Table 1.

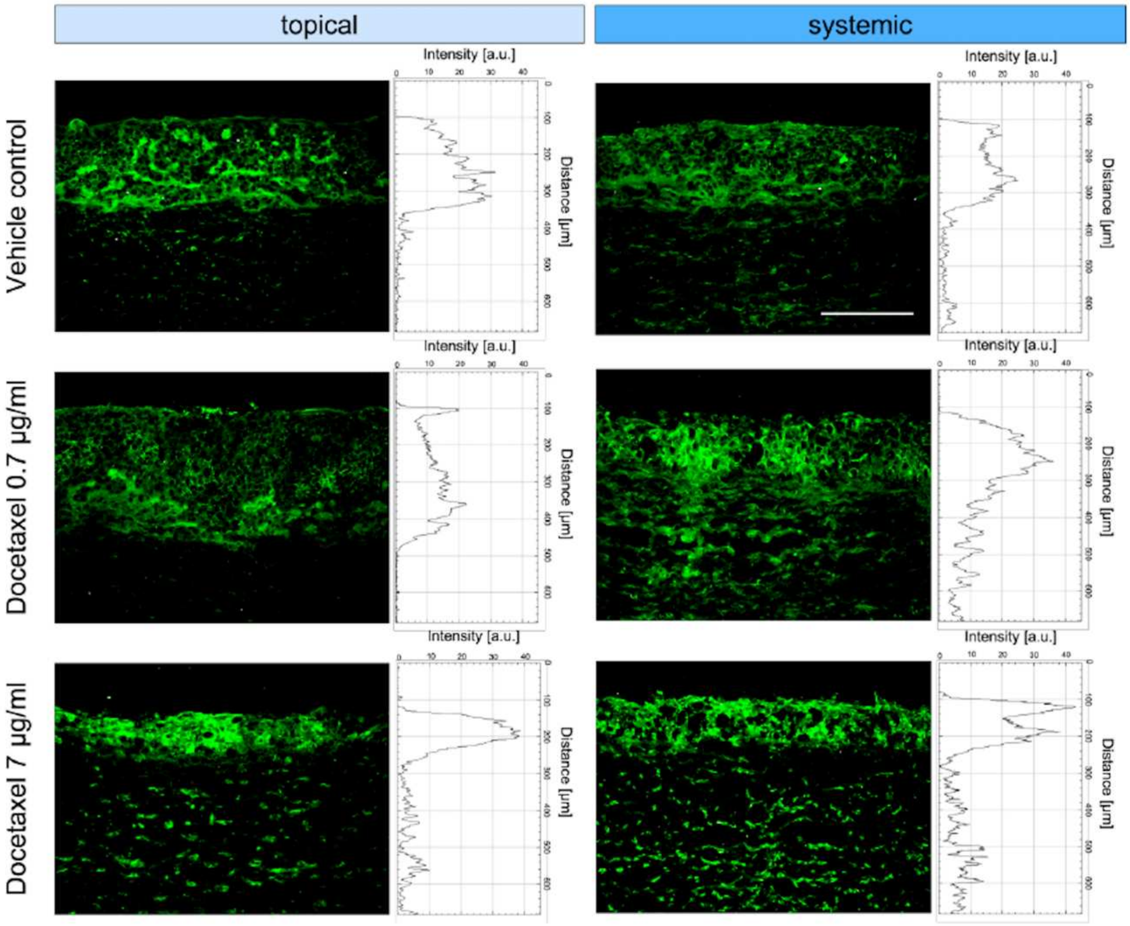

Supplementary Figure 7. Profile of interleukin (IL)-6 production following docetaxel treatment of SCC-25 models. Immunolocalization (green) of IL-6 following three times of 0.7 or 7 µg/ml docetaxel or vehicle control treatment. Images were representative of three batches; scale bar = 250 µm; for applied drug amounts refer to Table 1.

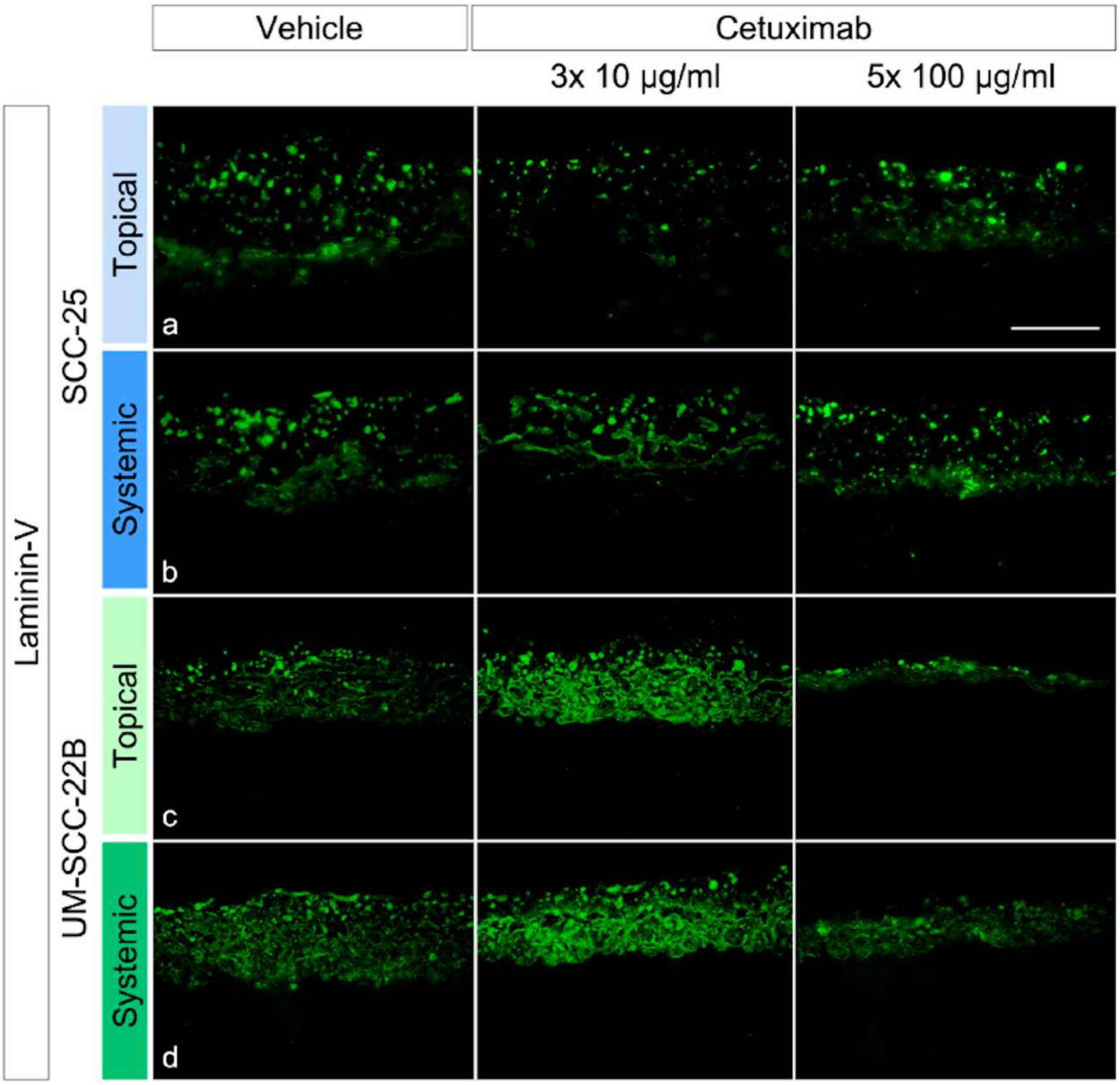

Supplementary Figure 8. Cetuximab effects on laminin-V expression in SCC-25 and UM-SCC-22B models. Immunolocalization (green) of laminin-V staining following **(a, c)** topical and **(b, d)** systemic cetuximab treatment. Images were representative of one to three batches; scale bar = 250 µm; for applied drug amounts refer to Table 1.

3. Extended Cultivation of Oral Mucosa Models

Leonie Gronbach[1], Philipp Jurmeister[2], Monika Schäfer-Korting[1], Ulrich Keilholz[5], Ingeborg Tinhofer[3,4], Christian Zoschke[1*]

[1] Freie Institute of Pharmacy, Pharmacology & Toxicology, Freie Universität Berlin, Germany

[2] Charité – Universitätsmedizin Berlin, corporate member of Freie Universität Berlin, Humboldt-Universität zu Berlin, and Berlin Institute of Health, Institute of Pathology, Germany

[3] Charité – Universitätsmedizin Berlin, corporate member of Freie Universität Berlin, Humboldt Universität zu Berlin, and Berlin Institute of Health, Department of Radiooncology and Radiotherapy, Charitéplatz 1, 10117 Berlin, Germany

[4] German Cancer Research Center (DKFZ), Heidelberg and German Cancer Consortium (DKTK) Partner Site Berlin, Berlin, Germany

[5] Charité – Universitätsmedizin Berlin, corporate member of Freie Universität Berlin, Humboldt-Universität zu Berlin, and Berlin Institute of Health, Comprehensive Cancer Center, Charitéplatz 1, 10117 Berlin, Germany

Frontiers in Bioengineering and Biotechnology, 8, 579896

https://doi.org/10.3389/fbioe.2020.579896

3.1 Contribution to Advanced Preclinical Drug Testing

The cells’ microenvironment is one of the most important driving forces in cell behavior, as well as in disease progression, especially in cancer (101). Consequently, models for preclinical drug testing should try to mimic the original microenvironment as close as possible. The approach of this study was to improve the models’ ECM by the integration of a human-based matrix composed of hyaluronic acid fibers and a mixture of thrombin and fibrinogen, called hyalograft. This approach showed its potential already in skin models, with increased stability and longevity of the models. To discover the benefits of this approach for 3D NOM and TOM models, hyalograft-based models have been built for different cultivation times and compared to collagen-based models. All models have been morphologically characterized and analyzed by detected protein levels and the ratios of proliferating and apoptotic cells. Hyalograft-based models also here showed its potential with an *in vivo* like morphology in the tumor models, and by greater model longevity with the exhibition of proliferating cells at up to 7-weeks of culture. This study was conducted and designed by me under the supervision of Prof. Dr. Monika Schäfer-Korting and Dr. Christian Zoschke. The building and morphological analysis of the models, TUNEL assays, as well as the detection of protein levels and count of proliferating and apoptotic cells, were performed by me. The model’s morphology has been validated by the pathologist, Dr. Philipp Jurmeister. The paper was originally drafted by me and revised together with all the co-authors.

3.2 Equity Ratio Statement

Title of the Manuscript

“Primary extracellular matrix enables long-term cultivation of human tumor oral mucosa models”

Journal	Frontiers in Bioengineering and Biotechnology
Authorship	First author
Status	in press

Own contribution

- Conception and design of the study together with Christian Zoschke
- Acquisition of the entire data set
    - Model establishment and building
    - Morphological and functional characterization
- Data analysis
- Figure development
- Original draft writing together with Christian Zoschke
- Revision of the entire manuscript together with the co-authors

3.3 Publication

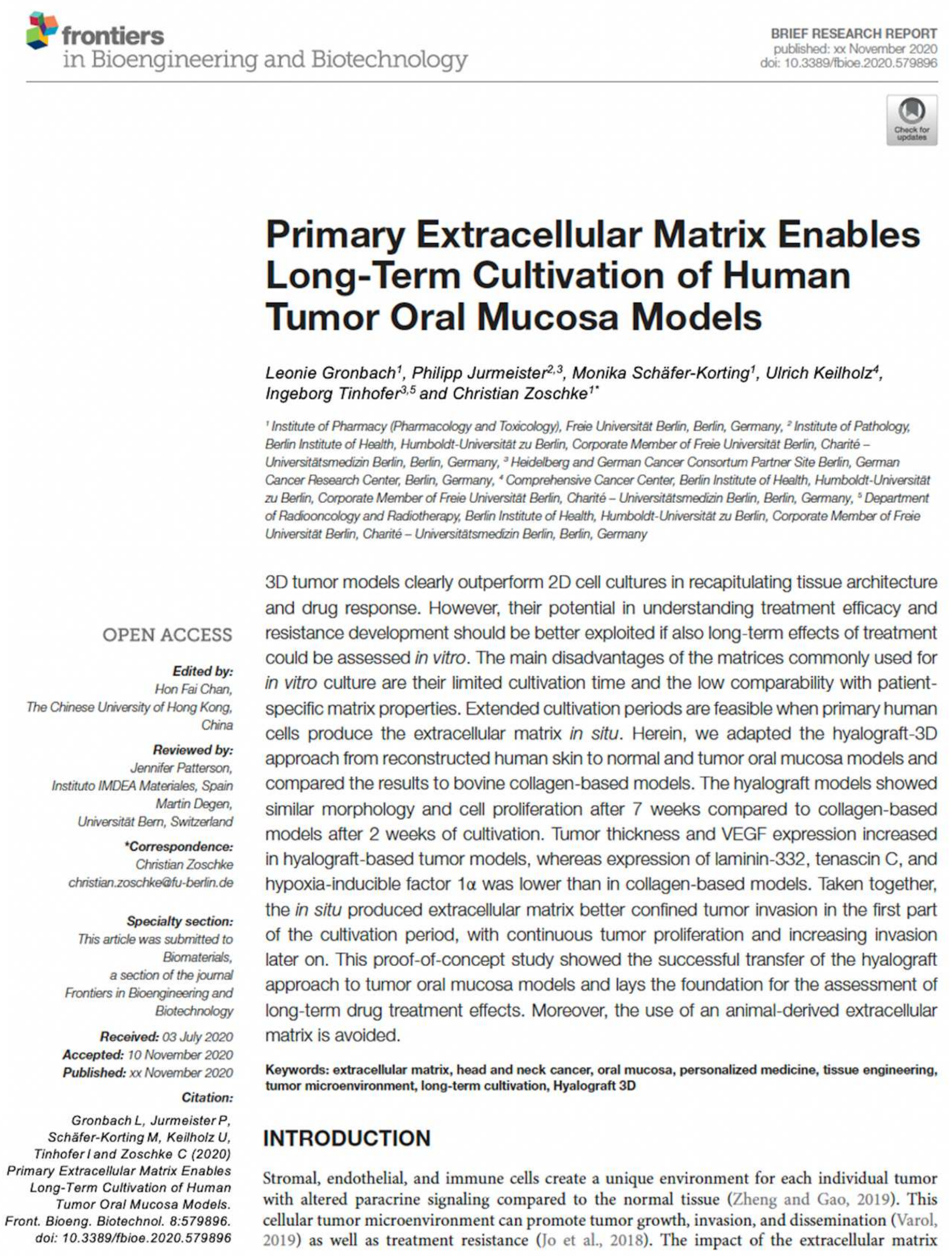

frontiers
in Bioengineering and Biotechnology

BRIEF RESEARCH REPORT
published: xx November 2020
doi: 10.3389/fbioe.2020.579896

Primary Extracellular Matrix Enables Long-Term Cultivation of Human Tumor Oral Mucosa Models

Leonie Gronbach[1], Philipp Jurmeister[2,3], Monika Schäfer-Korting[1], Ulrich Keilholz[4], Ingeborg Tinhofer[3,5] and Christian Zoschke[1]*

[1] Institute of Pharmacy (Pharmacology and Toxicology), Freie Universität Berlin, Berlin, Germany, [2] Institute of Pathology, Berlin Institute of Health, Humboldt-Universität zu Berlin, Corporate Member of Freie Universität Berlin, Charité – Universitätsmedizin Berlin, Berlin, Germany, [3] Heidelberg and German Cancer Consortum Partner Site Berlin, German Cancer Research Center, Berlin, Germany, [4] Comprehensive Cancer Center, Berlin Institute of Health, Humboldt-Universität zu Berlin, Corporate Member of Freie Universität Berlin, Charité – Universitätsmedizin Berlin, Berlin, Germany, [5] Department of Radiooncology and Radiotherapy, Berlin Institute of Health, Humboldt-Universität zu Berlin, Corporate Member of Freie Universität Berlin, Charité – Universitätsmedizin Berlin, Berlin, Germany

3D tumor models clearly outperform 2D cell cultures in recapitulating tissue architecture and drug response. However, their potential in understanding treatment efficacy and resistance development should be better exploited if also long-term effects of treatment could be assessed *in vitro*. The main disadvantages of the matrices commonly used for *in vitro* culture are their limited cultivation time and the low comparability with patient-specific matrix properties. Extended cultivation periods are feasible when primary human cells produce the extracellular matrix *in situ*. Herein, we adapted the hyalograft-3D approach from reconstructed human skin to normal and tumor oral mucosa models and compared the results to bovine collagen-based models. The hyalograft models showed similar morphology and cell proliferation after 7 weeks compared to collagen-based models after 2 weeks of cultivation. Tumor thickness and VEGF expression increased in hyalograft-based tumor models, whereas expression of laminin-332, tenascin C, and hypoxia-inducible factor 1α was lower than in collagen-based models. Taken together, the *in situ* produced extracellular matrix better confined tumor invasion in the first part of the cultivation period, with continuous tumor proliferation and increasing invasion later on. This proof-of-concept study showed the successful transfer of the hyalograft approach to tumor oral mucosa models and lays the foundation for the assessment of long-term drug treatment effects. Moreover, the use of an animal-derived extracellular matrix is avoided.

Keywords: extracellular matrix, head and neck cancer, oral mucosa, personalized medicine, tissue engineering, tumor microenvironment, long-term cultivation, Hyalograft 3D

Edited by:
Hon Fai Chan,
The Chinese University of Hong Kong,
China

Reviewed by:
Jennifer Patterson,
Instituto IMDEA Materiales, Spain
Martin Degen,
Universität Bern, Switzerland

****Correspondence:***
Christian Zoschke
christian.zoschke@fu-berlin.de

Specialty section:
This article was submitted to
Biomaterials,
a section of the journal
Frontiers in Bioengineering and
Biotechnology

Received: *03 July 2020*
Accepted: *10 November 2020*
Published: *xx November 2020*

Citation:
Gronbach L, Jurmeister P,
Schäfer-Korting M, Keilholz U,
Tinhofer I and Zoschke C (2020)
Primary Extracellular Matrix Enables
Long-Term Cultivation of Human
Tumor Oral Mucosa Models.
Front. Bioeng. Biotechnol. 8:579896.
doi: 10.3389/fbioe.2020.579896

INTRODUCTION

Stromal, endothelial, and immune cells create a unique environment for each individual tumor with altered paracrine signaling compared to the normal tissue (Zheng and Gao, 2019). This cellular tumor microenvironment can promote tumor growth, invasion, and dissemination (Varol, 2019) as well as treatment resistance (Jo et al., 2018). The impact of the extracellular matrix

(ECM) as the major component of the tumor microenvironment in these biological processes remains contradictory or unexplored (Pickup et al., 2014; Saggioro et al., 2020). Commonly, tumors dysregulate the composition and structure of the surrounding normal tissue toward an inflamed, hypoxic, and desmoplastic tumor microenvironment (Zheng and Gao, 2019). The effect of the tumor environment on the biology of tumors of the oral cavity remains to be investigated.

Patient-specific tumor ECMs are rarely recapitulated *ex vivo*. Tumor cells are either cultivated in scaffold-free ultra-low attachment plates or embedded in collagen of animal origin, e.g., Matrigel (Langhans, 2018). Furthermore, non-human matrices like cellulose are used as scaffolds for *ex vivo* tumor models (Nath and Devi, 2016). Major drawbacks of these approaches include poor stability, limited lifespan, and underrepresentation of patient-specific tumor microenvironment components. Initially designed to better reconstruct human skin, the hyalograft-3D is a biodegradable, non-immunogenic scaffold, which consists of esterified hyaluronic acid fibers. It is certified for medical use and allows the fibroblasts to produce and assemble their own ECM (Campoccia et al., 1998). Thereby, hyalograft-based skin models extended the life by six times, compared to collagen-based skin models (Stark et al., 2006).

Recently, we developed normal and tumor oral mucosa models emulating head and neck cancer, with a collagen scaffold (Gronbach et al., 2020) to improve non-clinical drug evaluation. The 3D model showed large similarities in morphology, grading, and protein expression profiles to patient's tumors. Moreover, the tumor models recapitulated docetaxel and cetuximab effects in line with clinical observations of head and neck-cancer. However, the cultivation of the collagen-based tumor models for a maximum of 2 weeks enabled only the investigation of short-term drug effects. This represents a major limitation for studies investigating the impact of genetic heterogeneity and therapy-driven clonal evolution in acquired drug resistance in the tumor (Magdeldin et al., 2014; Braig et al., 2017).

Herein, we assessed whether by using the hyalograft-3D approach human tumor oral mucosa models could be maintained in *ex vivo* cultures for up to 7 weeks, without major changes in tumor cell viability and proliferative activity. In addition, the impact of the ECM on tumor growth and invasion in hyalograft-based tumor oral mucosa models was compared with their collagen-based counterparts.

MATERIALS AND METHODS

Materials

Collagen G, DMEM 10× and HEPES buffer were purchased from Merck (Darmstadt, Germany). Hyalograft-3D was purchased from Anika Therapeutics (Bedford, MA, United States). The thrombin-fibrinogen-solution tisseel® was purchased from Baxter (Deerfield, IL, United States).

Human oral keratinocytes and human oral fibroblasts, as well as the respective cell culture media were purchased from ScienCell (Carlsbad, CA, United States). The tumor-cell line SCC-25 from the tongue (RRID: CVCL_1682, Rheinwald and Beckett, 1981) was a generous gift from Howard Green, Dana-Farber Cancer Institute (Boston, MA, United States). The detailed composition and origin of the construct growth and construct differentiation media were described elsewhere (Gronbach et al., 2020). Here, these media were supplemented with the transforming growth factor (TGF)-β1 and aprotinin, obtained from ThermoFisher Scientific (Waltham, MA, United States) and Merck. 12-well plates and 12-well inserts (0.4 μm pore size) were obtained from Greiner bio-one (Leipzig, Germany).

Hematoxylin, eosin, rotihistol, and rotihistokit were purchased from Carl Roth (Karlsruhe, Germany). Periodic acid was from Sigma-Aldrich and Schiff's reagent was obtained from Merck. Primary antibodies were purchased from abcam (Cambridge, United Kingdom): hypoxia-inducible factor 1α (1:200; RRID: AB_880418), Ki-67 (1:100; RRID: AB_302459), laminin-332 (1:500; RRID: AB_1566368), Tenascin C (1:1000; RRID: AB_2043021), vascular endothelial growth factor (1:200; RRID: AB_299738). Cytokeratin Pan Plus KL1 antibody (1:100; RRID: AB_2864507) was from Zytomed (Berlin, Germany). Anti-mouse and anti-rabbit IgGs (H + L), with F(ab')2 Fragment (Alexa Fluor® 488 and 594 Conjugate; RRIDs: AB_1904025, AB_2714182) were obtained from Cell Signaling Technology (Danvers, MA, United States). DAPI (4′,6-Diamidin-2-phenylindol) mounting medium was purchased from dianova (Hamburg, Germany). The *in situ* cell death detection kit (TUNEL assay) was purchased from Sigma-Aldrich (Munich, Germany).

Cell Culture

Human oral keratinocytes and human oral fibroblasts (ScienCell) were cultured in oral keratinocyte and fibroblast medium, respectively, at 37°C with 5% CO_2. The SCC-25 tumor-cell line was grown in DMEM/F-12 Ham medium, supplemented with 9% fetal calf serum, 0.9% L-glutamine, and penicillin/streptomycin. The medium was changed three times a week and the cells were passaged after reaching confluency of 80%. The cell line was tested for mycoplasm and regularly checked by single nucleotide polymorphism authentication (Multiplexion; Heidelberg, Germany). Cell culture was performed according to standard operating procedures and referred to good cell culture practice.

Multilayered Oral Mucosa Model Building

The multi-layered oral mucosa models (**Figure 1A**) were constructed as a lamina propria growing underneath an epithelium. All cultures were kept at 37°C and 5% CO_2 in a humidified atmosphere. The building of collagen-based oral mucosa models was described previously (Gronbach et al., 2020). Briefly, 1×10^5 human oral fibroblasts per model were mixed with a buffered solution and added to collagen. After solidification of the matrix, construct growth medium was added to the model and changed three times until day 7. Thereafter, either 1×10^6 human oral keratinocytes or 1×10^6 SCC-25 cells were seeded onto the lamina propria compartment for normal or tumor oral mucosa models, respectively. From day 14, the construct surface was kept medium-free to expose the epithelium to the air and the construct growth medium was supplemented with 0.25 mmol/l ascorbic acid acting as construct differentiation medium. On day 21, the models were snap frozen and stored at −80°C.

The generation of hyalograft-3D was described previously (Stark et al., 2006). In brief, the hyalograft-3D is a fleece-like matrix, composed of recombinant human hyaluronic acid fibers, esterified with benzylic alcohol to retard its degradation. Here, hyalograft-3D was cut into disks of 10 mm in diameter to fit the size of 12-well cell culture inserts. Next, 1×10^5 human oral fibroblasts per model were resuspended in a thrombin solution (10 international units/ml), mixed with a fibrinogen solution (8 mg/ml) and subsequently added to the pre-cut hyalograft-3D pieces. During the following 7 days, the fibroblasts were allowed to replace the fibrin by *in situ* produced ECM components (Stark et al., 2006). Thereafter, either human oral keratinocytes or SCC-25 cells were seeded onto the lamina propria compartment as described above for the collagen model. The construct growth medium was supplemented with 1 ng/ml transforming growth factor-β1 and 500 international units/ml aprotinin. TGF-β1 reduces keratinocyte differentiation and growth (Dahler et al., 2001). Aprotinin, a serin-protease inhibitor was used to limit fibrinolysis and thus premature model degradation. Medium was changed three times per week. From day 14, the construct surface was kept medium-free and aprotinin was reduced to 200 international units/ml in the construct differentiation medium. At the end of the cultivation period, the models were snap frozen and stored at −80°C.

Morphology and Protein Expression

The models were cut into 7 μm thick slices using a cryotome (Leica CM 1510S; Leica, Wetzlar, Germany) and fixed with 4% paraformaldehyde. The cryosections were subjected to either hematoxylin and eosin (H&E), periodic acid-Schiff (PAS), immunofluorescence staining or immunohistochemistry (IHC). For the H&E staining, slides were successively submerged into hematoxylin (5 min), water (5 min), eosin (30 s), 70 and 99.9% ethanol (2 min) and rotihistol (2 min). Finally, the slides were fixed with the rotihistokit and a cover slide. PAS staining was performed on a Tissue-Tek Prisma Plus Automated Slide Stainer (Sakura Finetech, Staufen, Germany). Slides were incubated with periodic acid for 10 min, followed by staining with Schiff's reagent for 10 min and hematoxylin for 7 min. For immunofluorescence staining, the samples were permeabilized for 5 min by a 0.5% triton solution, blocked for 30 min with 5% goat serum and incubated over night with the primary antibody at 4°C. Afterward the slides were incubated for 1 h with the secondary antibody. In the end, DAPI mounting medium was added to stain cell nuclei and fixed the samples. IHC staining was done on a BOND MAX Automated Slide Stainer (Leica) using the HP1 program and the BOND polymer Refine Detection System (Leica). Images were taken with a fluorescence microscope (BZ-8000; Keyence, Neu-Isenburg, Germany) and analyzed using the ImageJ software (Schneider et al., 2012).

Apoptosis Quantification

For apoptosis measurements, the *in situ* cell death detection kit was used according to the manufacturer's instructions. The kit detects DNA fragments in apoptotic cells based on TdT-mediated dUTP-biotin nick end labeling (TUNEL).

Data Analysis

Data are presented as the mean + standard deviation (SD) obtained from up to three independent experiments. Due to the explorative data analysis, a level of $p \leq 0.05$, calculated using non-parametric Kruskal–Wallis tests and subsequent Dunn's *Post hoc*-tests, was considered to indicate a statistically significant difference.

RESULTS

Morphological Analysis

We extended the culture period from 2 weeks of collagen-based normal oral mucosa models (c-NOM) and tumor oral mucosa models (c-TOM) to 7 weeks in hyalograft-based h-NOM and h-TOM models. To evaluate the impact of the scaffold, we cultured also h-NOM and h-TOM for 2 weeks (**Figure 1A**).

The epithelium of c-NOM models consisted of a basal layer with rounded cells and multiple layers of spinous cells, as found in non-keratinized oral mucosa (**Figure 1B**). All TOM models depicted an unstructured, hyperproliferative, and thickened epithelial layer with atypical, enlarged, irregular tumor cells and hyperchromatic nuclei. The tumor morphology appeared desmoplastic in particular in h-TOM models after 7 weeks of culture (**Figure 1B**, inserts).

The glycogen distribution was confined to the upper epithelial layers of the h-NOM model, while glycogen was found in all epithelial layers of c-NOM models (**Figure 1C**). A similar pattern was observed in TOM models after 2 weeks of culture (**Figure 1C**, inserts). Only after 7 weeks of culture the glycogen distribution became also patchy in h-TOM models. Concurrently, cytokeratin-positive tumor cells penetrated the hyalograft-3D matrix only slightly as tumor nests, but massively invaded the lamina propria compartment as single cells (**Figure 2A**). The final tumor thickness in h-TOM models exceeded tumor thickness of c-TOM models, but the difference was not statistically significant (**Figure 2B**).

The large structures in the lamina propria of hyalograft-based models were hyaluronic ester fibers, which were unspecifically stained by hematoxylin and eosin, periodic acid-Schiff as well as DAPI. The unspecific staining might be explained by the large three-dimensional structure of the fibers and their negative charge, which prevented the washout of stains as well as monoclonal antibodies, and led to the intercalation of DAPI into the fibers.

Protein Expression

The basement membrane protein laminin-332 was expressed in particular between the epithelial layer and the lamina propria in both h-NOM and c-NOM models (**Figure 2B**). In contrast, the expression of laminin-332 was more heterogeneous in TOM models with the highest levels in h-TOM models after 2 weeks of culture, in particular observed in the subepithelial zone in h-TOM models.

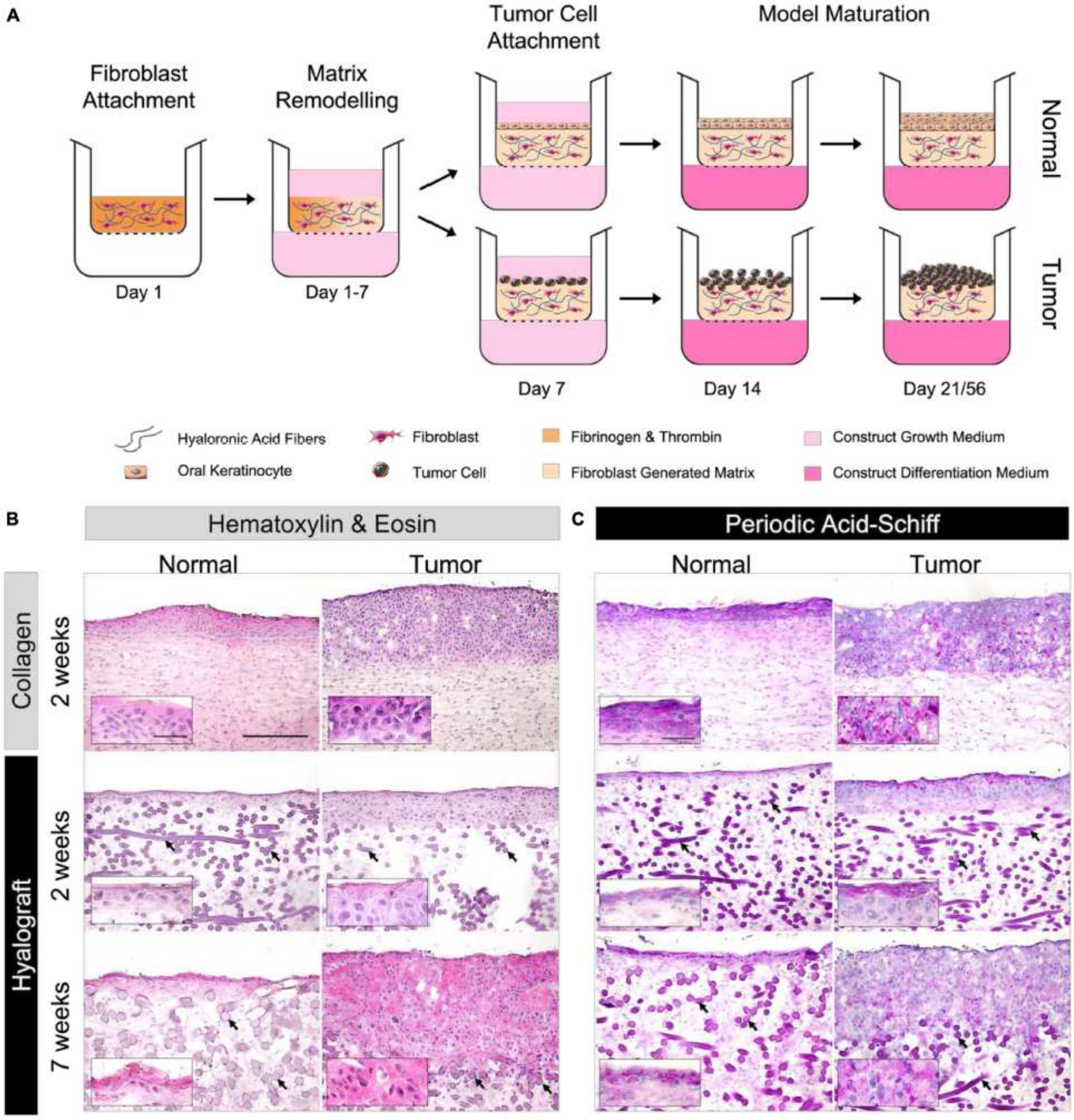

FIGURE 1 | Procedure outline and morphology of NOM and TOM models. **(A)** Human oral fibroblasts were suspended in a fibrinogen/thrombin solution and poured into a patch with esterified hyaluronic acid fibers (Hyalograft-3D). Fibroblasts replaced the fibrin gel by their own extracellular matrix (day 1–7). Normal oral keratinocytes or tumor cells were seeded on day 7 onto the matrix and grew until day 21 or 56 (2 or 7 weeks with tumor cells). **(B)** Hematoxylin and eosin and **(C)** Periodic Acid-Schiff staining. Dark purple structures in both stainings of the lamina propria were hyaluronic acid fibers of the scaffold (black arrows). The inserts show the difference between normal and tumor cell morphology by higher magnification. Representative images from the analysis of up to three batches are presented. Scale bars = 250 and 50 μm in the inserts.

The extracellular matrix protein tenascin C was most abundant in collagen-based models with no difference between NOM and TOM models (**Figure 3A**). Tenascin C expression markedly decreased in hyalograft-based models already after 2 weeks of cultivation and further declined to 33% ($p > 0.05$) after 7 weeks. Again, no relevant difference between NOM and TOM models was observed (**Figure 3B**).

The hypoxia-inducible factor (HIF)-1α was detected in the entire tumor mass of c-TOM models, and particularly in

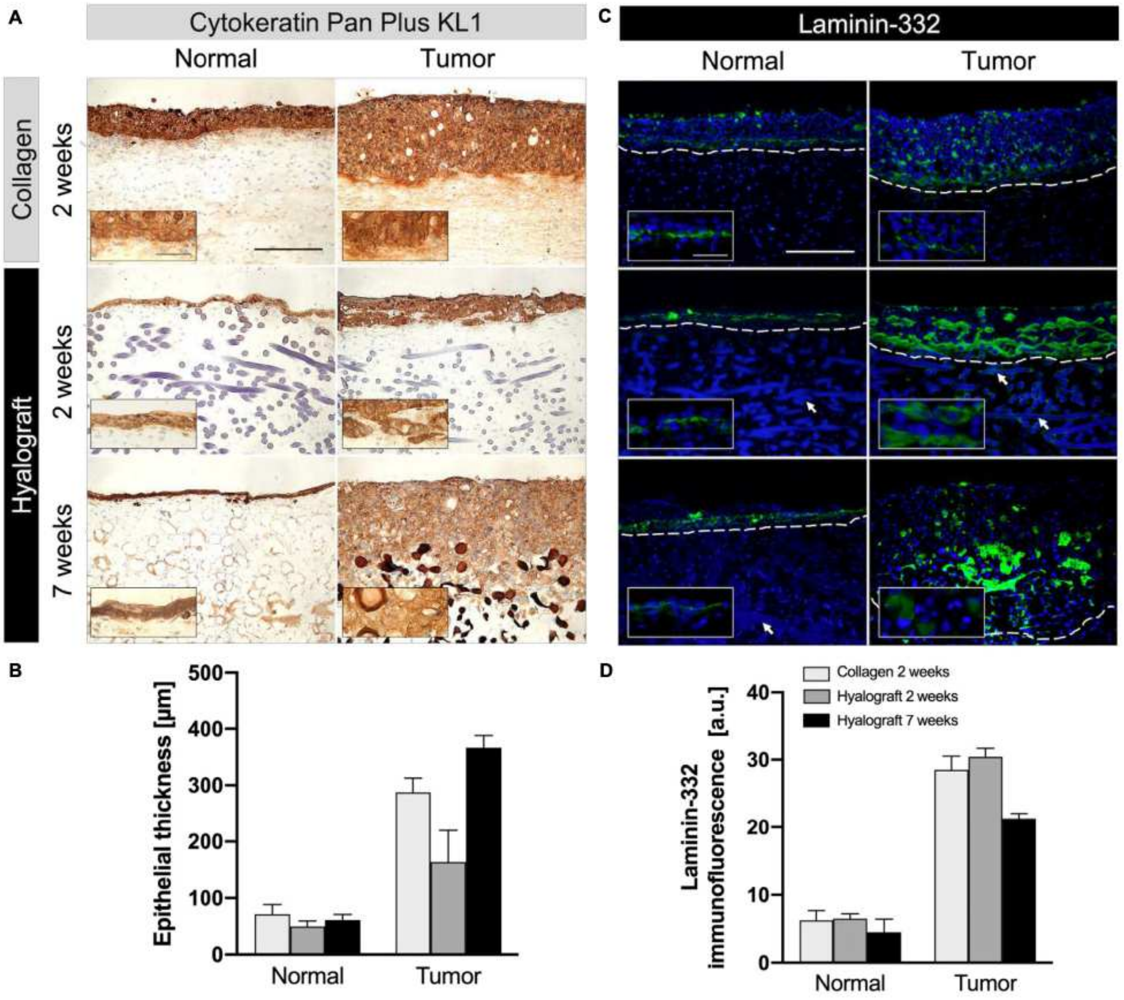

FIGURE 2 | Expression of cytokeratin and laminin-332 in NOM and TOM models. **(A)** Cytokeratin staining (brown) showed the absence of invasive growth in NOM and c-TOM models. In contrast, nests of cytokeratin positive cells started to infiltrate the lamina propria in h-TOM models after 2 weeks and markedly separated into single cells after 7 weeks. **(B)** Epithelial thickness in TOM models exceeded those in NOM models. The highest value occurred in h-TOM models after 7 weeks. **(C)** Laminin-332 (green) expression was restricted to a small layer in NOM models and diffusely clustered in TOM models. DAPI stained nuclei and fibers in blue, which could however be distinguished by their size and shape. The inserts show the border between epithelial cells and the matrix, with highest infiltration of the tumor cells in the 7 weeks cultured hyalograft-models, by higher magnification. White arrows highlight fibers and dashed lines indicate the border between epithelium and lamina propria. Representative images from up to three independent cultures are presented. Scale bars = 250 and 50 µm in the inserts. Bar graphs show the mean + SD from the quantitative analysis of up to six regions of interest.

central tumor areas in h-TOM models (**Figure 3C**). Very low levels of HIF-1α were detected in both c-NOM and h-NOM models (**Figure 3D**).

Overall, vascular endothelial growth factor (VEGF) was expressed at similar levels in the c-TOM and h-TOM models; however, the type of matrix interfered with its localization. While VEGF was detected in the entire tumor areas of c-TOM models, it was restricted to the border between the tumor layer and the lamina propria in h-TOM models (**Figures 4A,B**). VEGF expression further increased after 7 weeks both in NOM and TOM models ($p > 0.05$). Increased VEGF levels were particularly observed close to hyaluronic acid fibers in h-NOM models.

Proliferation and Apoptosis

Proliferation was higher in tumor compared to normal models, irrespective of the used matrix (**Figures 4C,D**). Importantly, tumor cells continued to proliferate excessively in h-TOM models until the end of the 7-week culture within all regions of the culture.

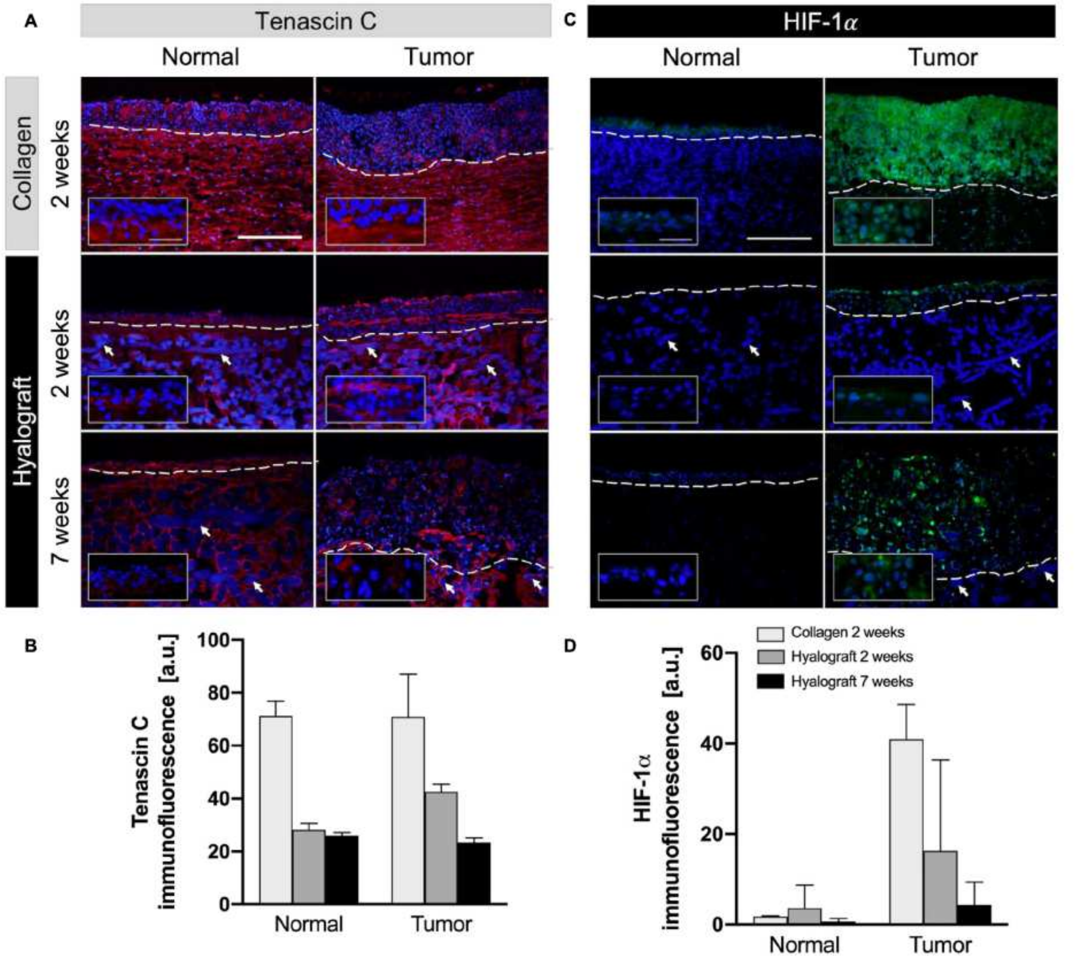

FIGURE 3 | Expression of tenascin c and HIF-1α in NOM and TOM models. **(A,B)** Tenascin c (red) was less expressed in hyalograft-based models than collagen-based models and further decreased during cultivation. **(C,D)** HIF-1α (green) showed increased expression in TOM models, with matrix-dependent differences. DAPI stained nuclei and fibers in blue. The inserts show the border between epithelial cells and the matrix for the tenascin C staining and highlights of the HIF-1α staining by higher magnification. White arrows highlight fibers and dashed lines indicate the border between epithelium and lamina propria. Representative images from up to three independent cultures are presented. Scale bar = 250 and 50 μm in the inserts. Bar graphs show the mean + SD from the quantitative analysis of up to six regions of interest of interest.

In c-NOM and the 7 weeks cultured h-NOM models, only few apoptotic cells could be detected (mean = 2.5%), while in the 2 weeks h-NOM models apoptotic cells made up to 20% of the epithelial cells (**Supplementary Figure 1**).

In TOM models, both 2 weeks cultured c-TOM and h-TOM models depicted less than 5% apoptotic cells, but the 7 weeks cultured h-TOM models showed up to 30% apoptotic cells.

DISCUSSION

We here showed that normal and tumor oral mucosa models can be successfully cultured in a hyalograft-based scaffold, allowing extended *ex vivo* cultivation. Our data corroborate previous findings showing that hyaluronic acid and its derivatives provide a well-defined and tunable scaffold for *ex vivo* tumor models (Fong et al., 2014). Moreover, hyalograft-based models are not affected by the poor adhesion of epithelial layers and the tendency to shrink of collagen-based models (Stark et al., 2004). In contrast, nylon-meshes and collagen-chitosan-sponges, which have been tested for elongated cultivation periods have the disadvantage of requiring long pre-cultivation and displaying considerable stiffness, thus complicating tissue sectioning and analysis (Michel et al., 1999; Stark et al., 2006).

Hyalograft-based tumor models contained high numbers of proliferative cells and recapitulated hallmarks of oral cancer

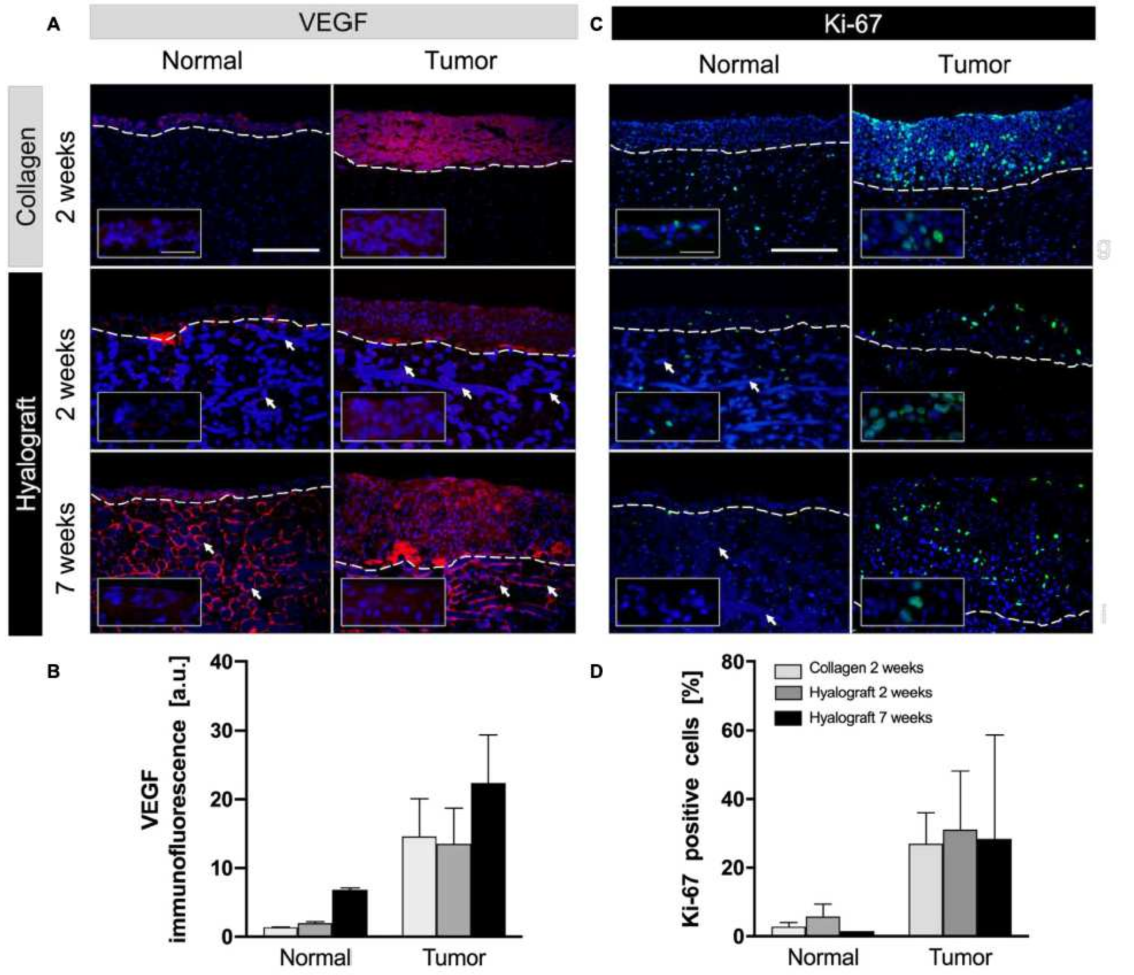

FIGURE 4 | Expression of vascular endothelial growth factor (VEGF) and proliferation (Ki-67) in NOM and TOM models. **(A,B)** Highest expression of VEGF (red) was observed in h-TOM models after 7 weeks. **(C,D)** The number of proliferative cells (Ki-67 positive, green) was increased in TOM models until the end of the cultivation period compared to NOM models. The inserts highlight detected VEGF and Ki-67 in the epithelial layers by higher magnification. Representative images from up to three independent cultures are presented. Scale bars = 250 and 50 μm in the inserts. Bar graphs show the mean + SD from the quantitative analysis of up to six regions of interest.

even after a cultivation period of 7 weeks. In particular, increased epithelial thickness, abundant cellular pleomorphism, and the altered laminin-332 expression, very well reflected the histopathological characteristics of patient tumors (Miyazaki, 2006; Bernstein et al., 2013; Jerjes et al., 2019). Thus, h-TOM models should be suitable to monitor long-term tumor progression as well as the effects of anti-proliferative drugs and the potential tumor re-growth after an initial treatment cycle. An improved understanding of the re-growth kinetics after drug treatment would help to overcome drug resistance, which is currently the major cause of treatment failure (Vasan et al., 2019).

Beside large similarities in protein expression patterns of hyalograft-and collagen-based models, there was a significant difference in tenascin C expression. The increased expression of tenascin C in collagen-based models might explain the faster growth in the epithelial layers of both c-NOM and c-TOM models, since tenascin C is known as a provisional matrix for keratinocyte growth (Pellegrini et al., 1999). Moreover, the expression of the extracellular matrix proteins tenascin c and fibronectin discriminates low- and high-risk tongue cancers (Sundquist et al., 2017). Low tenascin C expression in the h-TOM model established from SCC-25 cells is in line with the previously described poorly invasive phenotype of this cell line model (Ramos et al., 1997).

Normal oral fibroblasts better confined tumor invasion in hyalograft- than in collagen-based models after 2 weeks.

This difference might be related to paracrine signaling between fibroblasts and tumor cells which has been shown to depend on the composition of the ECM (Barcellos-Hoff and Bissell, 1989; Boudreau and Bissell, 1998). Laminin-332 appears to play a key part in the invasion process, in line with its higher expression in h-TOM compared to c-TOM models. While a well-defined laminin-332 expression is typical for normal tissues, clustered laminin-332 expression is known to promote cell survival and tumorigenesis, especially in squamous cell carcinoma (Marinkovich, 2007). In addition, the occurrence of desmoplasia in h-TOM models might contribute to delayed invasive growth and reduced hypoxia compared to c-TOM models. These differences in the ECM of collagen- and hyalograft-based models need to be considered in evaluating drug effects since hypoxia reduces the clinical efficacy of anticancer drugs (Brennan et al., 2005; Johnstone and Logan, 2006).

Although this proof-of-concept study shows the suitability of the hyalograft scaffold for the *ex vivo* cultivation of TOM models, future studies need to elucidate the scaffold effects on patient-derived tumor cells and compare these results to *in vivo* tumors. One limitation of the current h-TOM model is the relative high percentage of apoptotic tumor cells in long-term cultures. Further approaches for model improvement in the future might thus include also testing of additional supplements to the construct growth medium. Moreover, future studies will show whether the hyalograft approach better recapitulates the interaction of immune and tumor cells in an immunocompetent model of oral mucosa tumor, which seems very likely since the scaffold is non-immunogenic (Galassi et al., 2000). Given their close correlation to the individual tumor, long-term cultivation of human TOM models offer the opportunity to study tumor re-growth and alterations in the tumor stroma after initial treatment and thus will help to better understand drug resistance mechanisms.

CONCLUSION

The hyalograft-3D approach recapitulated key features of human oral squamous cell carcinoma in multi-layered *ex vivo* tumor models for up to 7 weeks. The long-term cultivation provides the basis for studying tumor re-growth and stromal alterations following an initial anti-cancer drug therapy. Moreover, the well-defined and tunable hyaluronic acid derivatives might help to better culture patient-derived cells. Finally, hyalograft-based models can be extended by the addition of further tumor stroma components and relinquish the use of animal-based scaffolds.

DATA AVAILABILITY STATEMENT

The raw data supporting the conclusions of this article will be made available by the authors, without undue reservation.

AUTHOR CONTRIBUTIONS

LG and CZ: conceptualization and design. LG, PJ, and CZ: investigation. CZ: project administration. MS-K, UK, and CZ: supervision. LG and CZ: visualization. LG and CZ: writing-original draft preparation. LG, MS-K, IT, and CZ: writing-review and editing. All authors contributed to the article and approved the submitted version.

FUNDING

The authors acknowledge support by the Open Access Publication Fund of the Freie Universität Berlin.

ACKNOWLEDGMENTS

The authors highly appreciated the excellent technical assistance of Jill García-Miller and Leticia M. Cruz.

SUPPLEMENTARY MATERIAL

The Supplementary Material for this article can be found online at: https://www.frontiersin.org/articles/10.3389/fbioe.2020.579896/full#supplementary-material

REFERENCES

Barcellos-Hoff, M. H., and Bissell, M. J. (1989). "A role for the extracellular matrix in Autocrine and Paracrine regulation of tissue-specific functions," in *Autocrine and Paracrine Mechanisms in Reproductive Endocrinology*, eds L. C. Krey, B. J. Gulyas, and J. A. McCracken (Boston, MA: Springer), 137–155.

Bernstein, J. M., Bernstein, C. R., West, C. M., and Homer, J. J. (2013). Molecular and cellular processes underlying the hallmarks of head and neck cancer. *Eur. Arch. Otorhinolaryngol.* 270, 2585–2593.

Boudreau, N., and Bissell, M. J. (1998). Extracellular matrix signaling: integration of form and function in normal and malignant cells. *Curr. Opin. Cell Biol.* 10, 640–646.

Braig, F., Kriegs, M., Voigtlaender, M., Habel, B., Grob, T., Biskup, K., et al. (2017). Cetuximab resistance in head and neck cancer is mediated by EGFR-K(521) Polymorphism. *Cancer Res.* 77, 1188–1199.

Brennan, P. A., Mackenzie, N., and Quintero, M. (2005). Hypoxia-inducible factor 1alpha in oral cancer. *J. Oral Pathol. Med.* 34, 385–389.

Campoccia, D., Doherty, P., Radice, M., Brun, P., Abatangelo, G., and Williams, D. F. (1998). Semisynthetic resorbable materials from hyaluronan esterification. *Biomaterials* 19, 2101–2127.

Dahler, A., Cavanagh, L., and Saunders, N. (2001). Suppression of keratinocyte growth and differentiation by transforming growth factor 1 involves multiple signaling pathways. *JIDEAE* 116, 266–274.

Fong, E. L. S., Martinez, M., Yang, J., Mikos, A. G., Navone, N. M., Harrington, D. A., et al. (2014). Hydrogel-based 3D model of patient-derived prostate xenograft tumors suitable for drug screening. *Mol. Pharm.* 11, 2040–2050.

Galassi, G., Brun, P., Radice, M., Cortivo, R., Zanon, G. F., Genovese, P., et al. (2000). In vitro reconstructed dermis implanted in human wounds: degradation studies of the HA-based supporting scaffold. *Biomaterials* 21, 2183–2191.

Gronbach, L., Wolff, C., Klinghammer, K., Stellmacher, J., Jurmeister, P., Alexiev, U., et al. (2020). A multilayered epithelial mucosa model of head neck squamous cell carcinoma for analysis of tumor-microenvironment interactions and drug development. *Biomaterials* 258:120277.

Jerjes, W., Hamdoon, Z., Yousif, A., Al-Rawi, N., and Hopper, C. (2019). Epithelial tissue thickness improves optical coherence tomography's ability in detecting oral cancer. *Photodiagn. Photodyn. Ther.* 28, 69–74.

Jo, Y., Choi, N., Kim, K., Koo, H.-J., Choi, J., and Kim, H. N. (2018). Chemoresistance of cancer cells: requirements of tumor microenvironment-mimicking in vitro models in anti-cancer drug development. *Theranostics* 8, 5259–5275.

Johnstone, S., and Logan, R. M. (2006). The role of vascular endothelial growth factor (VEGF) in oral dysplasia and oral squamous cell carcinoma. *Oral Oncol.* 42, 337–342.

Langhans, S. A. (2018). Three-dimensional in vitro cell culture models in drug discovery and drug repositioning. *Front. Pharmacol.* 9:6. doi: 10.3389/fphar.2018.00006

Loro, L. L., Vintermyr, O. K., Liavaag, P. G., Jonsson, R., and Johannessen, A. C. (1999). Oral squamous cell carcinoma is associated with decreased bcl-2/bax expression ratio and increased apoptosis. *Hum. Pathol.* 30, 1097–1105.

Magdeldin, T., López-Dávila, V., Villemant, C., Cameron, G., Drake, R., Cheema, U., et al. (2014). The efficacy of cetuximab in a tissue-engineered three-dimensional in vitro model of colorectal cancer. *J. Tissue Eng.* 5, 1–9.

Marinkovich, M. P. (2007). Laminin 332 in squamous-cell carcinoma. *Nat. Rev. Cancer* 7, 370–380.

Michel, M., L'Heureux, N., Pouliot, R., Xu, W., Auger, F. A., and Germain, L. (1999). Characterization of a new tissue-engineered human skin equivalent with hair. *Vitro Cell Dev. Biol. Anim.* 35, 318–326.

Miyazaki, K. (2006). Laminin-5 (laminin-332): unique biological activity and role in tumor growth and invasion. *Cancer Sci.* 97, 91–98.

Nath, S., and Devi, G. R. (2016). Three-dimensional culture systems in cancer research: focus on tumor spheroid model. *Pharmacol. Ther.* 163, 94–108.

Pellegrini, G., Ranno, R., Stracuzzi, G., Bondanza, S., Guerra, L., Zambruno, G., et al. (1999). The control of epidermal stem cells (holoclones) in the treatment of massive full-thickness burns with autologous keratinocytes cultured on fibrin. *Transplantation* 68, 868–879.

Pickup, M. W., Mouw, J. K., and Weaver, V. M. (2014). The extracellular matrix modulates the hallmarks of cancer. *EMBO Rep.* 15, 1243–1253.

Ramos, D. M., Chen, B. L., Boylen, K., Stern, M., Kramer, R. H., Sheppard, D., et al. (1997). Stromal fibroblasts influence oral squamous-cell carcinoma cell interactions with tenascin-C. *Int. J. Cancer* 72, 369–376.

Rheinwald, J. G., and Beckett, M. A. (1981). Tumorigenic keratinocyte lines requiring anchorage and fibroblast support cultured from human squamous cell carcinomas. *Cancer Res.* 41, 1657–1663.

Saggioro, M., D'Angelo, E., Bisogno, G., Agostini, M., and Pozzobon, M. (2020). Carcinoma and sarcoma microenvironment at a glance: where we are. *Front. Oncol.* 10:76. doi: 10.3389/fonc.2020.00076

Schneider, C. A., Rasband, W. S., and Eliceiri, K. W. (2012). NIH Image to ImageJ: 25 years of image analysis. *Nat. Methods* 9, 671–675.

Stark, H.-J., Boehnke, K., Mirancea, N., Willhauck, M. J., Pavesio, A., Fusenig, N. E., et al. (2006). Epidermal homeostasis in long-term scaffold-enforced skin equivalents. *J. Investig. Dermatol. Symp. Proc.* 11, 93–105.

Stark, H. J., Willhauck, M. J., Mirancea, N., Boehnke, K., Nord, I., Breitkreutz, D., et al. (2004). Authentic fibroblast matrix in dermal equivalents normalises epidermal histogenesis and dermoepidermal junction in organotypic co-culture. *Eur. J. Cell Biol.* 83, 631–645.

Sundquist, E., Kauppila, J. H., Veijola, J., Mroueh, R., Lehenkari, P., Laitinen, S., et al. (2017). Tenascin-C and fibronectin expression divide early stage tongue cancer into low- and high-risk groups. *Br. J. Cancer* 116, 640–648.

Varol, C. (2019). Tumorigenic interplay between macrophages and collagenous matrix in the tumor microenvironment. *Methods Mol. Biol.* 1944, 203–220.

Vasan, N., Baselga, J., and Hyman, D. M. (2019). A view on drug resistance in cancer. *Nature* 575, 299–309.

Zheng, J., and Gao, P. (2019). Toward normalization of the tumor microenvironment for cancer therapy. *Integr. Cancer Ther.* 18, 1–13.

Conflict of Interest: The authors declare that the research was conducted in the absence of any commercial or financial relationships that could be construed as a potential conflict of interest.

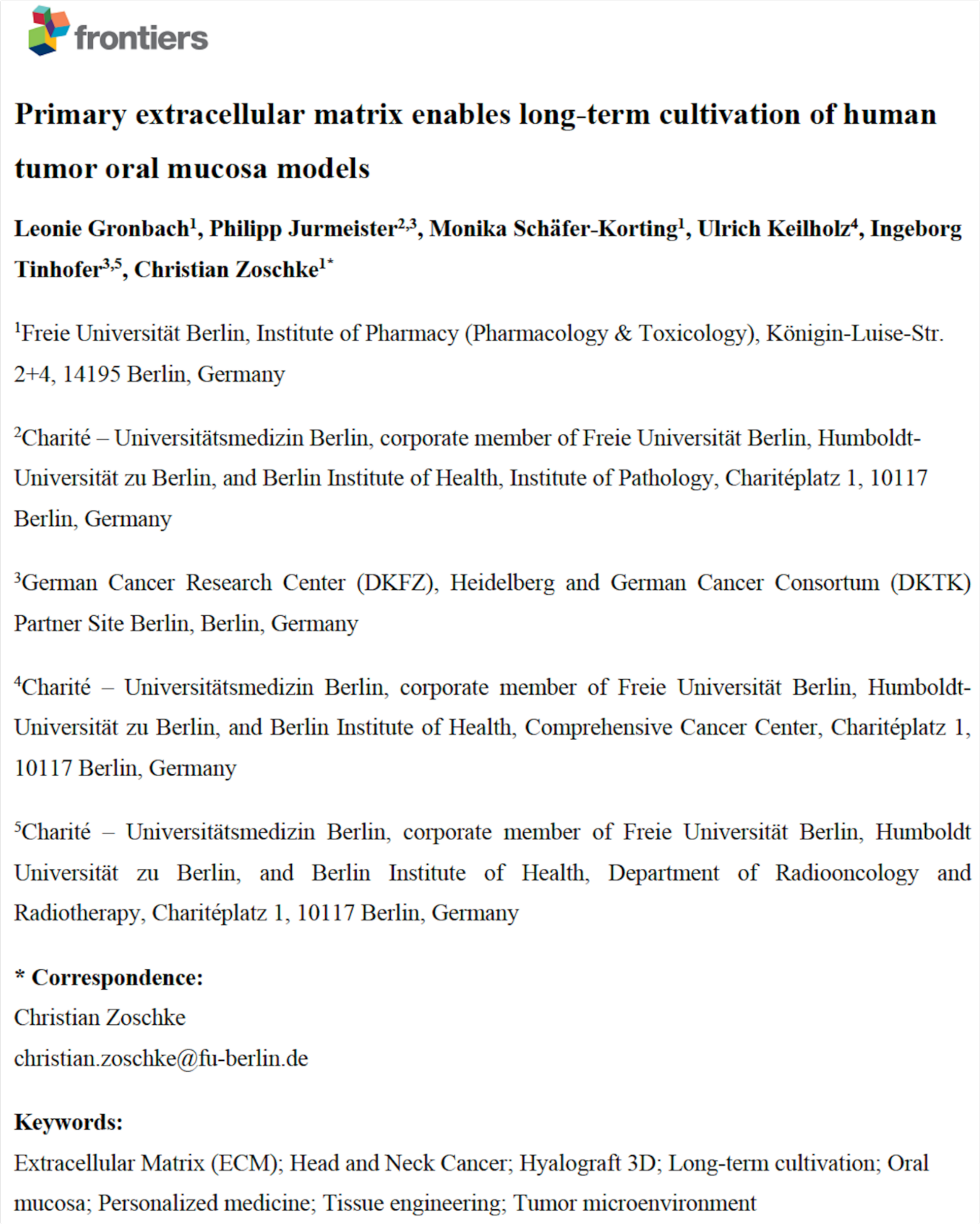

frontiers

Primary extracellular matrix enables long-term cultivation of human tumor oral mucosa models

Leonie Gronbach[1], Philipp Jurmeister[2,3], Monika Schäfer-Korting[1], Ulrich Keilholz[4], Ingeborg Tinhofer[3,5], Christian Zoschke[1*]

[1]Freie Universität Berlin, Institute of Pharmacy (Pharmacology & Toxicology), Königin-Luise-Str. 2+4, 14195 Berlin, Germany

[2]Charité – Universitätsmedizin Berlin, corporate member of Freie Universität Berlin, Humboldt-Universität zu Berlin, and Berlin Institute of Health, Institute of Pathology, Chariteplatz 1, 10117 Berlin, Germany

[3]German Cancer Research Center (DKFZ), Heidelberg and German Cancer Consortum (DKTK) Partner Site Berlin, Berlin, Germany

[4]Charité – Universitätsmedizin Berlin, corporate member of Freie Universität Berlin, Humboldt-Universität zu Berlin, and Berlin Institute of Health, Comprehensive Cancer Center, Chariteplatz 1, 10117 Berlin, Germany

[5]Charité – Universitätsmedizin Berlin, corporate member of Freie Universität Berlin, Humboldt Universität zu Berlin, and Berlin Institute of Health, Department of Radiooncology and Radiotherapy, Chariteplatz 1, 10117 Berlin, Germany

*** Correspondence:**
Christian Zoschke
christian.zoschke@fu-berlin.de

Keywords:
Extracellular Matrix (ECM); Head and Neck Cancer; Hyalograft 3D; Long-term cultivation; Oral mucosa; Personalized medicine; Tissue engineering; Tumor microenvironment

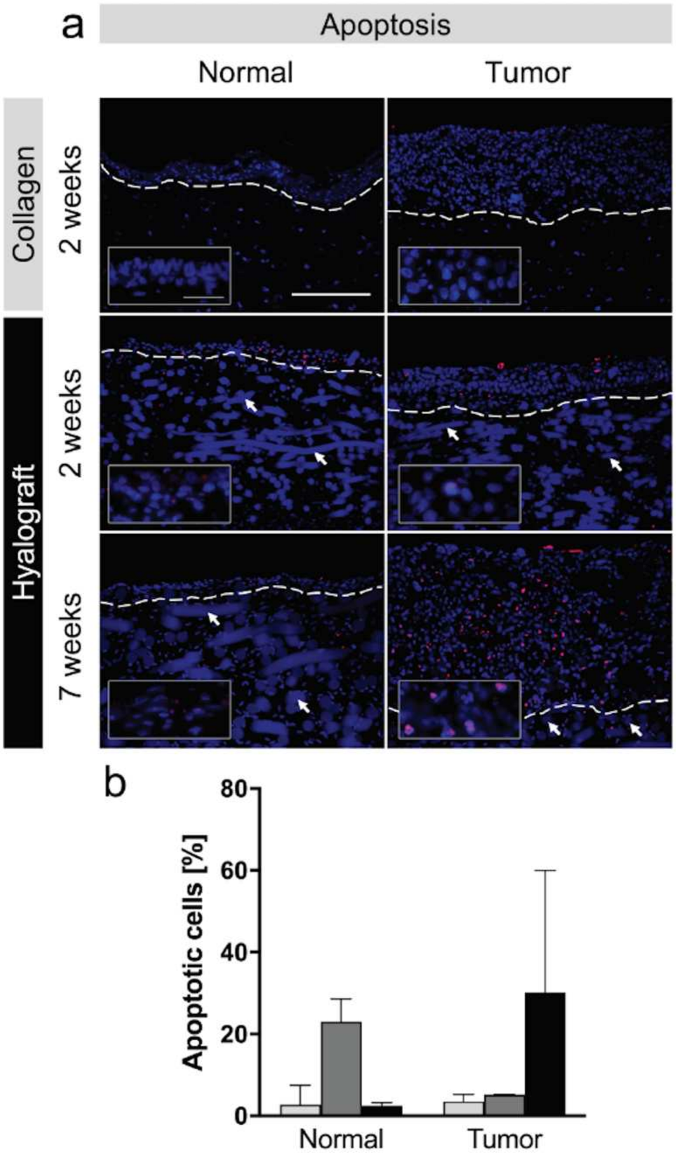

Supplementary Figure 1. Apoptosis in NOM and TOM models. a) Localization of apoptotic cells (red) by TUNEL assay and b) their quantification. The percentage of apoptotic cells peaked in h-NOM models after two weeks cultivation period and in h-TOM models after seven weeks of culture. DAPI stained nuclei and fibers in blue, which could however be distinguished by their size and shape. The inserts highlight detected apoptotic cells in the epithelial layers by higher magnification. White arrows highlight fibers and dashed lines indicate the border between epithelium and lamina propria. Representative images from up to three independent cultures are presented. Scale bar = 250 µm and 50 µm in the insert. Bar graphs show the mean + SD from the quantitative analysis of up to six regions of interest.

4. Automated Real-time Pharmacokinetic Drug Profiling in Tumor Oral Mucosa Models by UHPLC-MS/MS

Jan Joseph[1,+], Leonie Gronbach[2,+], Jill Garcia-Miller[2], Leticia M. Cruz[2], Ulrich Keilholz[3], Christian Zoschke[2], Maria K. Parr[4]

[1] Freie Universität Berlin, Core Facility BioSupraMol, Berlin, Germany
[2] Freie Universität Berlin, Institute of Pharmacy (Pharmacology & Toxicology), Berlin, Germany
[3] Charité – Universitätsmedizin Berlin, corporate member of Freie Universität Berlin, Humboldt-Universität zu Berlin, and Berlin Institute of Health, Comprehensive Cancer Center, Berlin, Germany
[4] Freie Universität Berlin, Institute of Pharmacy (Pharmaceutical and Medicinal Chemistry), Berlin, Germany
[+] Contributed equally

Pharmaceutics, 12, 413-427.

https://doi.org/10.3390/pharmaceutics12050413

4.1 Contribution to Advanced Preclinical Drug Testing

Pharmacokinetic profiling and the determination of the drug concentration at the target site are important factors in the drug dosage finding procedure. Automated pharmacokinetic sampling with minimal efforts, would facilitate the ability of high-throughput drug screenings and so make preclinical drug testing more efficient.

To aim this goal, 3D TOM models have been built inside a UHPLC-MS/MS device, with an integrated sampling-port. After model treatment with four different docetaxel doses, this construction offered automatic drug concentration measurements, without additional sample preparation, for a period of 96 h. Although the resulted concentration-time curves show variabilities in their profiles, this study represents a first proof-of-concept for automated pharmacokinetic drug profiling of 3D TOM models by UHPLC-MS/MS.

This study was conducted and designed by Prof. Maria Kristina Parr, Dr. Christian Zoschke, Dr. Jan Joseph, and me. The model adaptation with the integration of the sample-port into the model, as well as the building and morphological analysis of the models, were conducted by me, with the support of Leticia da Silva Cruz, and Jill Garcia Miller. The UHPLC-MS/MS measurements were performed by Dr. Jan Joseph. The data were analyzed, and the original paper was drafted by Dr. Jan Joseph, Dr. Christian Zoschke, and me. The critical discussion of the data and the revision of the manuscript were done together with the co-authors.

4.2 Equity Ratio Statement

Title of the Manuscript

"Automated real-time pharmacokinetic profiling in 3D tumor models: a novel approach for personalized medicine"

Journal	Pharmaceutics
Authorship	First author
Status	published

Own contribution

- Conception and design of the study together with Jan Joseph, Bernhard Wuest, Christian Zoschke, and Maria Parr
- Acquisition of the entire data set
    - Model establishment and building
    - Morphological characterization
- Interpretation of the data set together with Jan Joseph, Christian Zoschke, and Maria Parr
- Writing original draft together with Jan Joseph, Christian Zoschke, and Maria Parr
- Revising the entire manuscript together with the co-authors

4.3 Publication

pharmaceutics MDPI

Article

Automated Real-Time Tumor Pharmacokinetic Profiling in 3D Models: A Novel Approach for Personalized Medicine

Jan F. Joseph [1,†], Leonie Gronbach [2,†], Jill García-Miller [2], Leticia M. Cruz [2], Bernhard Wuest [3], Ulrich Keilholz [4], Christian Zoschke [2] and Maria K. Parr [5,*]

1 Core Facility BioSupraMol, Freie Universität Berlin, 14195 Berlin, Germany; jan.joseph@fu-berlin.de
2 Institute of Pharmacy (Pharmacology & Toxicology), Freie Universität Berlin, 14195 Berlin, Germany; leonie.gronbach@fu-berlin.de (L.G.); jillg94@zedat.fu-berlin.de (J.G.-M.); leticia.cruz@fu-berlin.de (L.M.C.); christian.zoschke@fu-berlin.de (C.Z.)
3 Agilent Technologies GmbH, 76337 Waldbronn, Germany; bernhard_wuest@agilent.com
4 Charité–Universitätsmedizin Berlin, corporate member of Freie Universität Berlin, Humboldt-Universität zu Berlin and Berlin Institute of Health, Comprehensive Cancer Center, 10117 Berlin, Germany; Ulrich.Keilholz@charite.de
5 Institute of Pharmacy (Pharmaceutical and Medicinal Chemistry), Freie Universität Berlin, 14195 Berlin, Germany
* Correspondence: maria.parr@fu-berlin.de; Tel.: +49-30-838-51471
† These authors contributed equally to this work.

Received: 31 March 2020; Accepted: 29 April 2020; Published: 30 April 2020

Abstract: Cancer treatment often lacks individual dose adaptation, contributing to insufficient efficacy and severe side effects. Thus, personalized approaches are highly desired. Although various analytical techniques are established to determine drug levels in preclinical models, they are limited in the automated real-time acquisition of pharmacokinetic profiles. Therefore, an online UHPLC-MS/MS system for quantitation of drug concentrations within 3D tumor oral mucosa models was generated. The integration of sampling ports into the 3D tumor models and their culture inside the autosampler allowed for real-time pharmacokinetic profiling without additional sample preparation. Docetaxel quantitation was validated according to EMA guidelines. The tumor models recapitulated the morphology of head-and-neck cancer and the dose-dependent tumor reduction following docetaxel treatment. The administration of four different docetaxel concentrations resulted in comparable courses of concentration versus time curves for 96 h. In conclusion, this proof-of-concept study demonstrated the feasibility of real-time monitoring of drug levels in 3D tumor models without any sample preparation. The inclusion of patient-derived tumor cells into our models may further optimize the pharmacotherapy of cancer patients by efficiently delivering personalized data of the target tissue.

Keywords: automatization; drug absorption; drug dosing; head-and-neck cancer; pharmacokinetics; real-time measurements; taxanes; tissue engineering; UHPLC-MS/MS

1. Introduction

Selecting clinically relevant doses for the evaluation of anticancer drugs remains challenging in preclinical drug development and contributes to the low translatability of effects in vitro to efficacy in patients. While the understanding of cancer biology advances as the complexity of tumor models and analytical techniques increases, the success rate of drug development in oncology remains the lowest among all therapeutic areas.

Historically, anticancer drug doses for clinical trials have been determined by extrapolating the maximum tolerated dose (MTD) in animals to the human patient. Taking the MTD as the starting point, the effective and safe dose for humans was anticipated in the range of −3 to +3, with three concentrations below and three concentrations above. The revision of this concept is urgently needed, since many nonoptimal doses were taken into late stages of drug development. Especially the testing of high-risk drugs requires a more conservative approach, using the minimum anticipated biological effect level (MABEL) in first-in-human trials [1,2].

Up to now, new concepts focused on the improved extrapolation from animal studies to clinical trials, e.g., by introducing drug metabolism and pharmacokinetic studies in early drug development [3]. In particular, model-based, adaptive/Bayesian approaches already helped to better find effective and safe dosage [4]. Nevertheless, animal models are affected by differences in the human pathophysiology and even xenograft models do not fully recapitulate the barriers of drug uptake into human solid tumors [5].

In fact, drug exposure of tumor cells depends on the architecture of solid tumors with cell density, the spatial arrangement of cells and extracellular matrix proteins, interstitial fluid pressure, and vascular supply [6–8]. While 2D monolayer cell culture cannot provide meaningful insights into the pharmacokinetic profiles of solid tumors, sophisticated 3D tumor models such as spheroids or multilayered tumor models could do this, eventually even in a patient-specific manner [9,10].

The introduction of in vitro tumor models into the dose selection for a particular patient requires adapting the protocols to high-content, high-throughput approaches to handle high numbers of tests, e.g., with different drugs and several combinations. However, analytical approaches to quantify drug amounts in tissues comprise imaging- and microdialysis-based methods. While imaging techniques and microdialysis closely map the drug distribution within (tumor) tissues, all methods share the high effort needed in sample preparation [11,12], restricting their use for personalized medicine.

Herein, the development of an in vitro approach for real-time pharmacokinetic investigations in human cell-based models of head-and-neck squamous cell carcinoma is reported. It aims for an automated measurement of docetaxel concentrations within the tumor tissue to quantify the drug absorption. Therefore, an UHPLC-MS/MS method was adapted from clinical practice and optimized for a maximum number of online measurements per time.

2. Materials and Methods

2.1. Materials

Oral fibroblasts and oral fibroblast medium were purchased from ScienCell (Carlsbad, CA, USA). Tongue cancer cells from the SCC-25 cell line (RRID:CVCL_1682) were a generous gift from Howard Green (Dana-Farber Cancer Institute; Boston, MA, USA) [13]. Collagen G was purchased from Biochrom (Berlin, Germany) and consumables for tumor oral mucosa model culture from Greiner bio-one (Leipzig, Germany). Docetaxel was purchased from Selleckchem (Houston, TX, USA). Acetonitrile, formic acid, methanol, and isopropanol, all LC-MS grade, were purchased from Sigma-Aldrich (München, Germany).

2.2. Cell Culture

Oral fibroblasts were precultured in oral fibroblast medium and SCC-25 cells in DMEM/F-12 Ham medium, supplemented with 9% fetal calf serum, 0.9% L-glutamine and 0.9% penicillin/streptomycin at 37 °C and 5% CO_2. The cancer cells were regularly checked by single nucleotide polymorphism authentication (Multiplexion; Heidelberg, Germany). The medium was changed three times a week and the cells were subcultivated after reaching a confluence of 80%. Cell culture was performed according to standard operating procedures and referred to good cell culture practice.

2.3. *Sample Port Integration into Tumor Oral Mucosa (TOM) Models*

Tumor oral mucosa (TOM) models were prepared as described elsewhere [14] but adopted to a 6-well-plate design to handle the integration of the sample port (Figure 1a). In brief, 0.3×10^6 oral fibroblasts were embedded in collagen G and 1×10^6 SCC-25 cells were seeded on top of these lamina propria equivalents one week after. The model growth medium was changed three times a week and replaced by model differentiation medium one week after seeding the tumor cells [14]. The sampling port was created by placing a 24-well insert (400 nm pore size) into the TOM model before the collagen started to solidify. The tumor cells proliferated and migrated into the collagen matrix around the sampling port for seven days, before docetaxel was applied. The 24-well insert was fixed by a custom-made metal support and filled with 600 μL serum-free growth medium. The top of the 6-well plate was sealed with aluminum foil (VWR, Darmstadt, Germany) instead of using the standard plastic lid. TOM models were incubated at 37 °C inside the autosampler of the UHPLC-MS/MS device (Agilent Technologies GmbH, Waldbronn, Germany) for the 96 h observation period in the final week of TOM model culture.

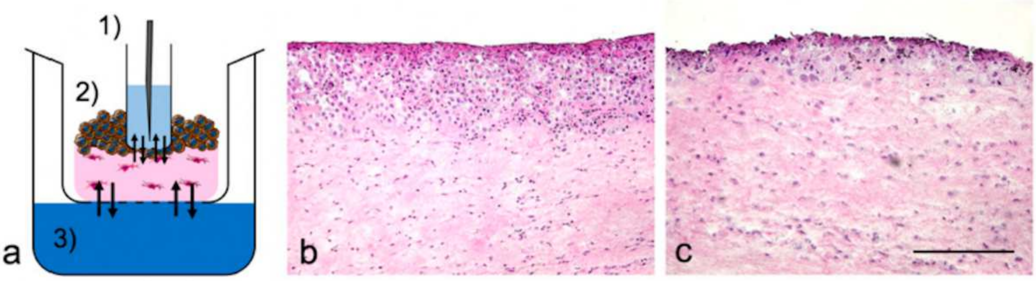

Figure 1. Experimental design and morphology of tumor oral mucosa (TOM) models. (**a**) Schematic cross-section of (1) sampling port with the needle of the autosampler, (2) TOM model with tumor cells (brown) and fibroblasts (magenta) within lamina propria, (3) Reservoir with differentiation medium, supplemented with docetaxel. The arrows indicate drug diffusion equilibria. Hematoxylin and eosin (H&E) staining of TOM models following two applications of (**b**) the vehicle control and (**c**) 7000 ng/mL docetaxel. Images were representative of four batches; scale bar = 250 μm.

2.4. *Docetaxel Treatment of TOM Models*

Docetaxel was dissolved in DMSO to a 70 mg/mL stock solution and diluted with construct differentiation medium to 7; 70; 700; 7000 ng/mL. DMSO, 0.01% in model differentiation medium, served as vehicle control since this was the maximum DMSO concentration among all samples (0.00001%; 0.0001%; 0.001%; and 0.01% DMSO for 7; 70; 700; 7000 ng/mL docetaxel). Docetaxel solutions were applied two times per construct with an application interval of 48 h.

2.5. *Morphological Analysis*

TOM models were snap frozen at the end of the 96 h observation period and cut into 7 μm thick slices using a cryotome (Leica CM 1510 S; Leica, Wetzlar, Germany). Cryosections were analyzed by hematoxylin and eosin (H&E) staining and pictures were taken with a microscope (BZ-8000; Keyence, Neu-Isenburg, Germany).

2.6. *UHPLC-MS/MS Analyses*

Method A: For automated real-time quantitation of docetaxel, an Agilent 1290 UHPLC coupled to an Agilent 6495 triple quadrupole tandem mass spectrometer equipped with a Jet Stream electrospray ionization (ESI) source was used (Agilent Technologies GmbH, Waldbronn, Germany). Separation of docetaxel was achieved on an Agilent Poroshell Phenyl Hexyl column (50 mm × 2.1 mm, 1.9 μm particle size) equipped with a corresponding guard column (5 mm × 2.1 mm, 1.9 μm particle size) using water (solvent A) and acetonitrile (solvent B) each containing 0.1% formic acid (*v/v*) as mobile phase. At a flow rate of 0.350 mL/min, the following gradient was applied: 5% B for 0.5 min, to 100% B at 4 min, 1 min hold, 5% B at 5.1 min, stop time 6.50 min. The column compartment was kept at 40 °C. The injection volume was 5 µL and the autosampler temperature was set to 37 °C. A needle wash (acetonitrile/methanol/isopropanol/water, 25% each, *v/v/v/v*) was applied for 20 s while an additional needle seat backflush using an Agilent Flex Cube was used to minimize carry over (15 s at 2 mL/min with needle wash solvent, pure isopropanol, and a mixture of water/acetonitrile (95/5, *v/v*) containing 0.1% formic acid). The total run time was 9.75 min.

The mass spectrometer was operated in multiple reaction monitoring (MRM) acquisition mode. Positive electrospray ionization mode (ESI+) yielded the sodium adduct of docetaxel $[M + Na]^+$ and was detected at *m/z* 830.3. Source and MRM parameters were optimized using Mass Hunter Source Optimizer software (version 1.1, Agilent Technologies Inc., Santa Clara, CA, USA). Final source parameters were as follows: drying gas temperature: 230 °C, drying gas flow: 20 L/min (nitrogen), nebulizer pressure: 40 psi (nitrogen), sheath gas temperature: 390 °C, sheath gas flow: 12 L/min (nitrogen), capillary voltage: +4,500 V, nozzle voltage: +300 V, high pressure radio frequency (HPRF): 210 V, low pressure radio frequency (LPRF): 160 V. MRM details are listed in Table 1. MassHunter (Quant) software (version B08, Agilent Technologies Inc., Santa Clara, CA, USA) was used for data acquisition and processing.

Table 1. Multiple reaction monitoring (MRM) transitions of docetaxel sodium adduct, used in method A.

Precursor Ion (*m/z*)	Product Ion (*m/z*)	Collision Energy	Cell Accelerator Voltage	Polarity
830.3	549.1	25	4	Positive
830.3	304.1	20	2	Positive

Method B: For identification of degradation products, an Agilent 1290 II HPLC connected to an Agilent 6550 iFunnel QTOF with Agilent Jet Stream source was used (Agilent Technologies Inc., Santa Clara, CA, USA). Separation of docetaxel and its metabolites was achieved on an Agilent Poroshell Phenyl Hexyl column (50 mm × 2.1 mm, 1.9 µm particle size) equipped with a corresponding guard column (5 mm × 2.1 mm, 1.9 µm particle size) using water (solvent A) and acetonitrile (solvent B) each containing 0.1% formic acid (*v/v*) as mobile phase. At a flow rate of 0.350 mL/min, a longer gradient was applied: 5% B for 0.5 min, to 37% B at 5 min, 50% B at 10 min, to 98% B at 15 min, 2 min hold, back to 5% B at 17.1 min, stop time 19 min. The column compartment was kept at 40 °C. The injection volume was 5 µL. A needle wash (acetonitrile, methanol, isopropanol, water) was applied for 20 s. The mass spectrometric parameters were as follows: drying gas temperature: 230 °C, drying gas flow 14 L/min (nitrogen), nebulizer pressure 40 psi (nitrogen), sheath gas temperature: 375 °C, sheath gas flow: 12 L/min (nitrogen), capillary voltage +4,500 V, nozzle voltage +300 V, high pressure radio frequency 200 V, low pressure radio frequency 100 V, fragmentor 365 V. Data acquisition was performed in auto MS/MS mode using a mass range of *m/z* 100–1000 at a scan rate of 1 spectrum/s for MS1 and *m/z* 50–1000 for MS2 experiments at 3 spectra/s. The collision energy was adjusted depending on the target *m/z* value (offset 4 eV, slope 3 eV/*m/z* 100).

2.7. Validation

Method A was used for automated real-time quantitation of docetaxel and validated in terms of selectivity, carry-over, lower limit of quantitation (LLOQ), calibration function, accuracy, and precision following the recommendations of the European Medicines Agency's (EMA) guideline on bioanalytical method validation [15]. All calibration (CAL) and quality control (QC) samples were freshly prepared in serum-free model differentiation medium as sample diluents.

Selectivity and carry-over: The guidelines require the analysis of matrix from four different lots. Since the matrix was artificial, no remarkable differences had to be considered. Thus, only one batch was used for assessing selectivity. Blank samples (serum-free model differentiation medium) were analyzed and compared with samples spiked with docetaxel at the LLOQ. Less than 20% detector response of the LLOQ is required for the blank samples. Carry-over was determined by analyzing blank samples after the injection of a high concentration QC (HQC) sample (7,500 ng/mL). Again, less than 20% detector response of the LLOQ is required to comply with the EMA guidelines.

Lower limit of quantitation and calibration: The LLOQ needs to be determined with sufficient accuracy and precision and with at least 5 times higher detector response than a blank sample. For evaluation, matrix-matched samples of 0.1, 0.25, 0.5, 1.0, 5.0 ng/mL were investigated. Additionally, the limit of detection (LOD) was determined based on calculations according to ICH guidelines [16]. Calibration samples in medium ranged from the LLOQ of 0.001 µg/mL to the upper limit of quantitation (ULOQ) of 10 µg/mL. In addition to an analyte free matrix sample, eight levels of calibration samples were prepared in triplicate and analyzed on two consecutive days.

Accuracy and precision: Accuracy and precision were assessed on serum-free medium samples spiked with docetaxel at 4 different QC levels with 5 replicates per level in a concentration range from the LLOQ to the ULOQ covering the calibration range. Samples were analyzed on two different days. Mean concentrations and the coefficient of variation (CV) of QC samples were required to be within ±15% in general, or ±20% at the LLOQ of the nominal concentrations, respectively. Within-run and between-run accuracy and precision were determined.

2.8. Sample Preparation for the Identification of Degradation Products

The degradation products of docetaxel were analyzed in the differentiation medium cultivated with the models (Table 2). To handle these samples, a protein precipitation procedure was performed. Aliquots of 100 µL of the samples were added to 400 µL of cold acetonitrile and centrifuged at 3328× *g* for 10 min. The serum-free supernatant was then transferred into LC-MS/MS vials for further analysis, according to method B.

Table 2. LC-MS data of docetaxel (highlighted gray) and postulated degradation products, acquired using method B.

Degradation Product	Formula	RT (min)	*m/z*	Exact Mass	Adduct	Mass Accuracy (ppm)
Carbamate	$C_{38}H_{45}NO_{12}$	4.30	708.3010	708.3015	$[M + H]^+$	0.65
10DABIII	$C_{29}H_{36}O_{10}$	4.55	545.2378	545.2381	$[M + H]^+$	0.60
Epi-carbamate	$C_{38}H_{45}NO_{12}$	4.72	708.3004	708.3015	$[M + H]^+$	1.47
Epi-10DABIII	$C_{29}H_{36}O_{10}$	5.31	567.2196	567.2201	$[M + Na]^+$	0.76
Oxo-10DABIII	$C_{29}H_{34}O_{10}$	5.40	565.2041	565.2044	$[M + Na]^+$	0.56
Epi-oxo-10DABIII	$C_{29}H_{34}O_{10}$	5.84	565.2040	565.2044	$[M + Na]^+$	0.67
1-7 Docetaxel	$C_{43}H_{53}NO_{14}$	7.95	830.3374	830.3358	$[M + Na]^+$	−1.9
Epi-Docetaxel	$C_{43}H_{53}NO_{14}$	9.08	830.3377	830.3358	$[M + Na]^+$	−2.26
Oxo-Docetaxel	$C_{43}H_{51}NO_{14}$	9.94	828.3200	828.3202	$[M + Na]^+$	0.19
Epi-oxo-Docetaxel	$C_{43}H_{51}NO_{14}$	11.07	828.3192	828.3202	$[M + Na]^+$	1.16

2.9. Pharmacokinetic Analysis

Pharmacokinetic analyses were conducted in R [17]. First, a non-compartmental analysis was performed. Assumptions were: (i) dose was calculated by concentration in the reservoir x volume (Figure 1a(3)); (ii) area under the concentration curve (AUC) 0–48 h lasted until 48 h and AUC 48–96 h until the end of the experiment; (iii) for the concentration between 48–96 h the unmeasured concentrations were not considered. Afterwards, interval AUCs were calculated. For 0–48 h, the AUC was calculated from 0.0001 h (start of the experiment) to the end of the 1st cycle; for 48–96 h, the AUC was calculated from the time "end of the 1st cycle" to "end of the 2nd cycle". However, the end of the 2nd cycle varied, since in some experiments, the last concentrations could not be measured. The maximum concentration (C_{max}) was determined based on the measured concentrations; time to maximum concentration (t_{max}) was the corresponding time to C_{max}.

3. Results

3.1. TOM Models with Sampling Port

The TOM models reproducibly showed an unstructured and hyperproliferative epithelial layer with pleomorphic tumor cells, also separating from the epithelial layer into the lamina propria. Neither the sampling port nor the cultivation within the autosampler of the UHPLC-MS/MS device influenced the tumor growth. The effects of docetaxel on the tumor size in TOM models by supplementing the differentiation medium with either two drug doses or the vehicle control were determined. Whereas the vehicle control did not change the tumor morphology (Figure 1b), docetaxel caused a dose-dependent reduction of tumor size with abundant epithelial cell death (Figure 1c). The average tumor size declined from 347 ± 72 µm (untreated) to 100 ± 45 µm (max docetaxel concentration, $n = 4$ each).

3.2. Docetaxel Epimerization and Degradation Products

During electrospray ionization, docetaxel mainly forms a sodium adduct ($[M + Na]^+_{theor}$=830.3358), which is used as precursor ion for all MS/MS experiments. As shown in Figure 2 (top), the product ion spectrum of docetaxel shows three major fragments at *m/z* 549.2095 (taxane nucleus (10-deacetylbaccatin III, 10DABIII), $[C_{29}H_{34}O_9 + Na]^+$, exact mass *m/z* 549.2095, mass error $\Delta m/z = 0$ ppm), *m/z* 304.1159 (phenylpropionic acid side chain, $[C_{14}H_{19}NO{+}Na]^+$, exact mass *m/z* 304.1155, $\Delta m/z = -1.17$ ppm), and *m/z* 248.0537 (side chain with loss of the tert-butyl moiety, $[C_{10}H_{11}NO_5 + Na]^+$, exact mass *m/z* 248.0529, $\Delta m/z = -3.05$ ppm). The two main fragments *m/z* 549. 1 and *m/z* 304.1 were later chosen for MRM transitions in real-time quantitation (method A).

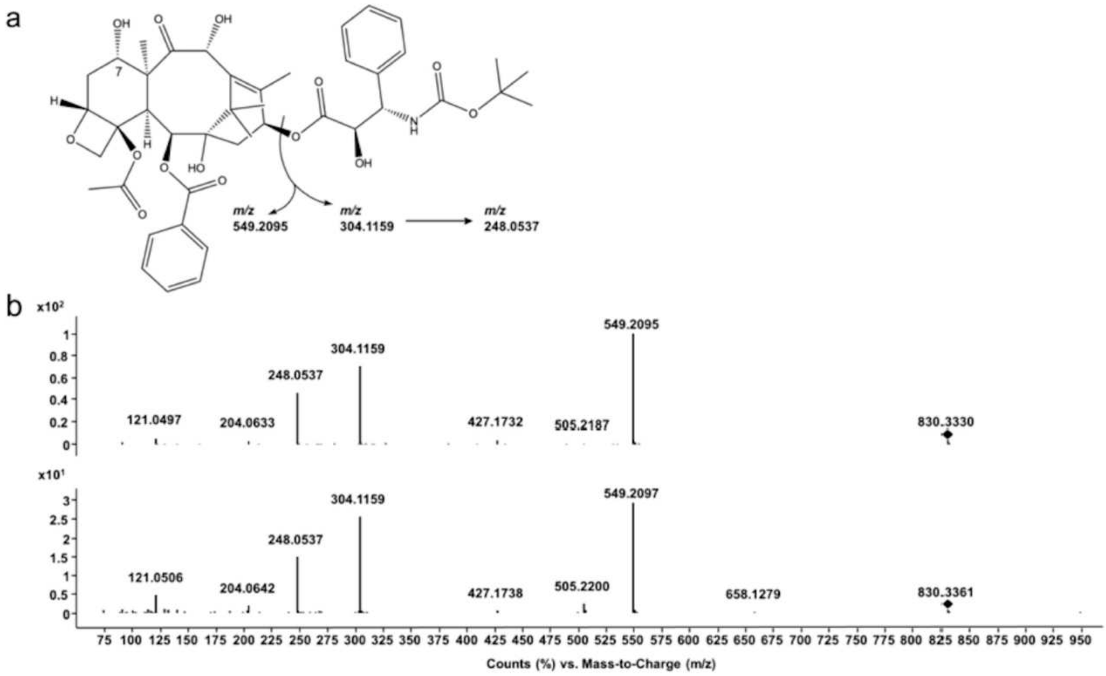

Figure 2. Docetaxel structure fragmentation. (**a**) Chemical structure of docetaxel and main fragmentation products. (**b**) Product ion spectra of docetaxel (top) and its potential 7-epimer (bottom), precursor $[M + Na]^+_{theor}$ = 830.3358 indicated with black rhombus.

Analyses of docetaxel reference substance as well as cell culture media without cells, and TOM models, revealed a second peak with almost identical MRM transitions (method A, chromatogram showing transitions in Figure S1) and product ions (method B, Figure 2 (bottom)). It already appeared only minutes after preparing the samples for analysis with serum-free medium as sample diluent. This degradation product is postulated to be the 7-epimer of docetaxel (epi-docetaxel), which is known to occur in basic and acidic conditions [18,19]. Since the epimerization could not be avoided in calibration or quality control samples as well, the combined peak areas of docetaxel and the 7-epimer were considered for all further quantitation experiments of docetaxel.

Based on accurate mass data, we postulated further degradation products beside the main degradant epi-docetaxel. Oxidized species of docetaxel and several hydrolysis products (ester and carbamate hydrolysis), as well as oxidation of the products of ester hydrolysis and their respective epimers (Table 2, Figures S3 and S4) are assigned. Two oxidized species of docetaxel show abundant sodium adducts in MS1 of *m/z* 828.3200 (oxo-docetaxel, RT: 9.94 min, $[C_{43}H_{51}NO_{14} + Na^+]^+$, exact mass *m/z* 828.3202, $\Delta m/z = 0.19$ ppm) and *m/z* 828.3192 (epi-oxo-docetaxel, RT: 11.07 min, $[C_{43}H_{51}NO_{14} + Na^+]^+$, exact mass *m/z* 828.3192, $\Delta m/z = 1.16$ ppm). Their MS/MS spectra show abundant fragments at $m/z_{\text{oxo-docetaxel}}$ 772.2534 and $m/z_{\text{epi-oxo-docetaxel}}$ 772.2584 ($[C_{39}H_{43}NO_{14} + Na]^+$, exact mass *m/z* 772.2576, $\Delta m/z_{\text{oxo-docetaxel}} = -1.07$ ppm and $\Delta m/z_{\text{epi-oxo-docetaxel}} = 5.41$ ppm), which may originate from the loss of the tert-butyl residue. They both show a fragment corresponding to an oxidation at the taxane nucleus at $m/z_{\text{oxo-docetaxel}}$ 547.1927 and $m/z_{\text{epi-oxo-docetaxel}}$ 547.1955 ($[C_{29}H_{32}O_9 + Na]^+$, exact mass *m/z* 547.1939, $\Delta m/z_{\text{oxo-docetaxel}} = 2.11$ ppm and $\Delta m/z_{\text{epi-oxo-docetaxel}} = -3.01$ ppm). Analogously to docetaxel, the fragment *m/z* 304.1173 originated from the intact phenylpropionic acid side chain ($[C_{14}H_{19}NO_5 + Na]^+$, exact mass *m/z* 304.1155, $\Delta m/z_{\text{oxo-docetaxel}} = -5.77$ ppm).

Further degradation products of docetaxel resulted from the ester hydrolysis of the taxane nucleus and the phenylpropionic acid side chain and are postulated here as 10DABIII (*m/z* 545.2378, RT: 4.55 min, $[C_{29}H_{36}O_{10} + H]^+$, exact mass *m/z* 545.2381, $\Delta m/z = 0.60$ ppm) and epi-10DABIII (*m/z* 567.2196, RT: 5.31 min, $[C_{29}H_{36}O_{10} + Na]^+$, exact mass *m/z* 567.2201, $\Delta m/z = 0.83$ ppm). A loss of benzoic acid, acetic acid and two losses of water from 10DABIII resulted in the fragment *m/z* 327.1587 ($[C_{20}H_{22}O_4 + H]^+$, exact mass *m/z* 327.1591, $\Delta m/z = 1.18$ ppm). Epi-10DABIII showed a fragment at *m/z* 445.1791 ($[C_{22}H_{30}O_8 + Na]^+$, exact mass *m/z* 445.1833, $\Delta m/z = 9.41$ ppm) which may correspond to the loss of the benzoic acid moiety and *m/z* 385.1615 ($[C_{20}H_{26}O_6 + Na]^+$, exact mass *m/z* 385.1622, $\Delta m/z = 1.71$ ppm), which indicates a subsequent loss of acetic acid.

These two hydrolyzed esters most likely exist in an oxidized form as well, which are proposed as oxo-10DABIII (*m/z* 565.2041, RT: 5.40 min, $[C_{29}H_{34}O_{10} + Na]^+$, exact mass *m/z* 565.2044, $\Delta m/z = 0.56$ ppm) and epi-oxo-10DABIII (*m/z* 565.2040, RT: 5.84 min, $[C_{29}H_{34}O_{10} + Na]^+$, exact mass *m/z* 565.2044, $\Delta m/z = 0.74$ ppm) based on their accurate mass data. They both show a distinct fragment at $m/z_{\text{oxo-10DABIII}}$ 443.1661 and $m/z_{\text{epi-oxo-10DABIII}}$ 443.1680 ($[C_{22}H_{28}O_8 + Na]^+$, exact mass *m/z* 443.1676, $\Delta m/z_{\text{oxo-10DABIII}} = 3.47$ ppm and $\Delta m/z_{\text{epi-oxo-10DABIII}} = -0.81$ ppm), most likely originating from the loss of the benzoic acid moiety.

Furthermore, the hydrolysis of the carbamate function of docetaxel revealed two more products: 'Carbamate' showed an *m/z* 708.3010 in MS1 ($[C_{38}H_{45}NO_{12} + H]^+$, exact mass *m/z* 708.3015, $\Delta m/z = 0.64$ ppm), and an abundant fragment of *m/z* 182.0818 in MS/MS which may originate from the cleavage of the remaining phenylpropionic acid side chain and the taxane nucleus ($[C_9H_{11}NO_3 + H]^+$, exact mass *m/z* 182.0812, $\Delta m/z = -3.46$ ppm). 'Epi-carbamate' showed a similar product ion spectrum with the same base peak of *m/z* 182.0820 ($[C_9H_{11}NO_3 + H]^+$, exact mass *m/z* 182.0812, $\Delta m/z = -4.56$ ppm) and *m/z* 708.3004 ($[C_{38}H_{45}NO_{12} + H]^+$, exact mass *m/z* 708.3015, $\Delta m/z = 1.47$ ppm) in MS1.

An exemplary chromatogram of the degradation products following two applications of 70 µg/mL docetaxel for 48 h each is shown in Figure S2. We found only trace amounts of docetaxel degradation products in the TOM model media following the two applications of 7 µg/mL docetaxel for 48 h each. Therefore, we did not consider the degradation products in the real-time pharmacokinetic analyses.

3.3. Validation

As method A is used for quantitation in the online hyphenation of the tumor model with UHPLC based analysis, it was validated according to the guideline of the EMA [15].

Selectivity and carry-over: The method fulfilled the criteria for selectivity (<20% response in blank artificial matrix compared to response obtained at LLOQ) with a maximum of 7.45% detector response. Carry-over was a more critical parameter since the concentration range was very broad. Even after the optimization of the injector wash procedures, the detector response of analyte-free matrix samples exceeded the allowed 20% LLOQ detector response with a maximum of 29.42% after injection of HQC samples. Therefore, additional blank sample injections were included after samples of high concentrations resulted in successful prevention of carry-over.

Lower limit of quantitation and calibration: The concentration of 0.001 µg/mL showed acceptable accuracy (92.42–114.17%) and precision (6.58%CV) and was therefore chosen as the lowest point of the calibration. Based on the EMA guideline, the calculated LLOQ was 0.16 ng/mL and LOD 0.05 ng/mL, respectively.

For the calibration function, a quadratic fit after log-log transformation of the data provided the best results in terms of a combination of low residuals and best overall accuracy. All CAL samples met the requirements by EMA.

Accuracy and precision: The method (A) fulfilled the requirements given by EMA. Calculated concentrations of QC and CAL samples were within ±15% of the nominal values (Table 3), only 8.33% (within-day) and 15% (between-day) with only individual values outside.

Table 3. Accuracy and precision. c: docetaxel concentration, CV: coefficient of variation, RE: Relative error as measure of accuracy, LLOQ: lower limit of quantitation, LQC: lower quality control, MQC: middle quality control, HQC: higher quality control.

QC	Within-Day (n = 5)				Between-Day (n = 5)		
	Expected c (ng/mL)	Mean Calculated c (ng/mL)	CV (%)	RE (%)	Mean Calculated c (ng/mL)	CV (%)	RE (%)
LLOQ	1.00	1.06	7.26	5.71	1.01	11.40	1.62
LQC	3.00	2.76	2.27	−7.87	2.67	3.37	−10.94
MQC	3000	3027	7.83	0.89	3254	9.48	8.48
HQC	7500	6982	7.79	−6.91	7676	9.57	2.35

3.4. Docetaxel Pharmacokinetics in TOM Models

The area under the concentration curves (AUC), the maximum concentration (C_{max}), and the time to maximum concentration (t_{max}) as main pharmacokinetic parameters for the concentration versus time profiles of docetaxel within the sampling port are summarized in Table 4.

The course of the concentration versus time curves was comparable between the applied drug doses (Figure 3). Following the administration of docetaxel by supplementing the differentiation medium of TOM models in the reservoir at 0 h, the drug concentration increased until a plateau phase. The time to maximum concentration t_{max}, 39 ± 7.9 h was almost independent of the administered docetaxel dose, while the C_{max} depended on the administered docetaxel dose. Following the exchange of the differentiation medium, again supplemented with the same docetaxel doses, we detected 2.4- to 9.1-fold increased maximum concentrations and 2.4- to 8.8-fold increased AUCs in the sampling port compared to the respective values following the first docetaxel administration. Furthermore, we detected about 4- to 7-fold higher docetaxel concentrations in the sampling port compared to the applied docetaxel concentration (Figure 3b,c). This effect was not observed when applying 7 or 7000 ng/mL docetaxel (Figure 3a,d). Again, the t_{max} values were close to the end of the treatment cycle with values ranging between 82 and 89 h.

Table 4. Main pharmacokinetic parameters following 1st docetaxel application (0–48 h) and 2nd docetaxel application (48–96 h). c: docetaxel concentration, AUC: area under the curve.

c	AUC (0–48 h)		C_{max} (0–48 h)		t_{max} (0–48 h)	
(ng/mL)	Mean (h × ng/mL)	CV (%)	Mean (ng/mL)	CV (%)	t_{max} (h)	CV (%)
7	66.3	44.6	1.9	194.5	43.9	14.5
70	444.4	12.5	14.4	25.3	39.5	20.7
700	13,324	26.0	461	29.0	41	9.9
7000	85,658	8.3	2492	10.4	32	21.4

c	AUC (48–96 h)		C_{max} (48–96 h)		t_{max} (48–96 h)	
(ng/mL)	Mean (h × ng/mL)	CV (%)	Mean (ng/mL)	CV (%)	t_{max} (h)	CV (%)
7	151.4	84.4	6.0	65.1	82.8	16.2
70	3915.1	75.0	131.4	78.5	82.7	15.5
700	78,890	75.1	2850	66.3	83	16.6
7000	211,171	12.2	5920	7.3	90	13.7

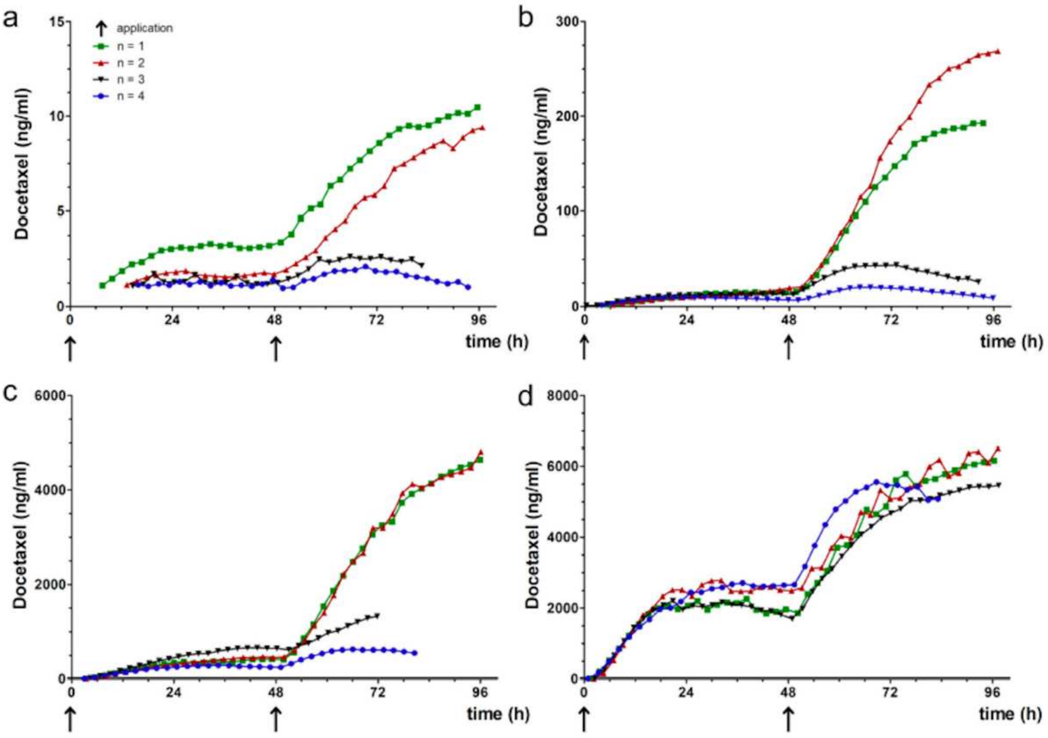

Figure 3. Concentration-time curves of docetaxel. Docetaxel concentrations in the sampling port of TOM models following the application of (a) 7, (b) 70, (c) 700 or (d) 7000 ng/mL docetaxel. Docetaxel was supplemented to the differentiation at 0 and 48 h (arrows), $n = 4$ for each concentration.

Moreover, the concentration versus time curves showed a different shape in two experiments (blue and black curve vs. red and green curve in Figure 3a–c). The slope of the blue and black curves markedly differed from the slope of the red and green curves after the second docetaxel administration. The relatively constant docetaxel concentrations within the sampling port could result from evaporation of medium from the reservoir (Figure 1a(3)), causing in loss of contact of the model with the reservoir.

Evaporation also affected the accessibility of the sample fluid for the autosampler needle, since we did not measure docetaxel from certain time points on (e.g., black curve in Figure 3c).

4. Discussion

An automated UHPLC-MS/MS method with online sampling in TOM models is presented here. This proof-of-concept study demonstrated the feasibility of real-time monitoring of drug levels in TOM models without any sample preparation. To achieve this, both the analytical method for docetaxel quantitation in human blood samples [20] and the culture of TOM models [14] needed to be adapted only slightly. Our approach was validated according to EMA guidelines [15] and is easily transferrable to other in vitro disease models.

In vitro studies frequently use drug doses far higher than the maximum tolerated dose in patients [21]. This overdosing causes effects in vitro that are not reproducible in vivo, contributing to the high attrition rate of investigational new drugs in clinical trials. Even if the patients tolerate such high doses, they will be prone to off-target effects. Aside from the bench-to-bedside extrapolation of drug doses, clinical data can be useful to conduct more relevant studies for investigation of personalized adaptations. Considering the maximum plasma concentration at the highest single dose recommended in the drug product of marketed drugs provides an upper limit for in vitro studies [22]. This concept is particularly useful to test potential new indications for approved drugs. We used docetaxel as a model drug to develop our analytical approach since both the efficacy and the pharmacokinetics of docetaxel are well-known [22]. After calculating a steady-state concentration of 74 ng/mL docetaxel in patients following an intravenous application of 75 mg/m^2 (for details, see [14]), we selected 7; 70; 700; and 7000 ng/mL as test concentrations in TOM models. The AUC within the TOM models ranged between 66.32 and 85,658.15 h × ng/mL following the first, and between 151 and 211,171 h×ng/mL following the second docetaxel application. Together with C_{max} values below 2492 and 5920 ng/mL, these in vitro results were in range of the clinical application of 100 mg/m^2, which results in an AUC of 4600 h × ng/mL and C_{max} of 3700 ng/mL [23].

Focusing on the nominal concentration of 70 ng/mL, we detected less docetaxel in the sampling port than has been found in human blood samples. This discrepancy supports the hypothesis of the poor uptake of anticancer drugs into solid tumors [6]. Likewise, paclitaxel penetrates only to the periphery of spheroids [5]. Nevertheless, docetaxel uptake into the TOM models increased following the second drug application. Since apoptosis results in enhanced drug uptake into inner cell layers of solid tumors [8], tumor cells dying after the first application should favor docetaxel uptake into TOM models.

Moreover, our method provides an in-depth insight into the formation of docetaxel degradation products. Since docetaxel epimerization is associated with a loss of potency and tumor resistance development in vivo [24], the considerable epimer formation will affect the efficacy of docetaxel. In contrast, the trace amounts of oxidation products and carbamates should not limit docetaxel effects in TOM models, although they are 10- to 40-fold less active [25]. The degradation products were identified by QTOF-MS and related to degradation products known from the literature [26]. Nevertheless, our approach allows for only limited insights into clinically relevant clearance due to the absence of hepatic metabolism and biliary excretion. If tumor cells metabolize the applied drugs, the quantitation of local metabolites will be feasible as well, but in the case at hand, we observed docetaxel epimerization and formation of degradation products as artifacts also in cell-free medium.

Differences between docetaxel concentrations in human patients and TOM models also arise from differences in protein binding. Whereas plasma protein binding of docetaxel is 97% in the patients [22], protein binding in medium containing fetal bovine serum is saturable. Paclitaxel, close in chemical structure to docetaxel, shows a protein binding between 79% at 500 ng/mL and 20% at 15,000 ng/mL [27]. Thus, we expect higher amounts of free drug available compared to the patients, especially following the application of 7000 ng/mL docetaxel. Nevertheless, we were not able to discriminate free against total docetaxel concentration, since the membrane of the sampling port has a pore size of 400 nm. Most protein sizes range between 1 and 100 nm, making protein diffusion into the sampling port likely. This might also explain higher C_{max} values in the sampling port than the administered concentration in the reservoir, since we quantified all docetaxel within the sampling port. The first docetaxel administration saturated the protein binding and intracellular fluids, the second application directly increased the concentration in the interstitial fluid of TOM models and the sampling port. However, we assume complete equilibration between the interstitial fluid of the TOM model and the sampling fluid within two hours, equal to the time interval we selected between two measurements. Thus, signals of the concentration over time curve earlier between zero and two hours might not recapitulate the concentration within the interstitial fluid of the TOM model, but provide an insight into the lag-time between docetaxel application and first appearance within the sampling port. As to be expected, the lag-time decreases with increasing docetaxel concentrations: 11.1 ± 3 h (7 ng/mL docetaxel application) compared to 1.82 ± 0.6 h (7000 ng/mL docetaxel application).

Since classical microdialysis already allowed insights into tissue-specific drug [28] and cytokine levels [29], the automated determination of pharmacokinetic profiles will enable patient-specific analyses in higher throughput. PK-PD modelling already improved dose selection and characterization of drug effects on tumor growth, overall survival and safety [30], but requires relevant data for the patient and his/her tumor. Nonclinical testing together with pharmacometrics may provide a more detailed insight by testing drugs in patient-specific models and extrapolating drug concentrations in tumors to adapt dose regimen for patients.

UHPLC-MS/MS again proved as the method of choice as it was already useful for a wide range of applications in pharmacology, toxicology, and forensics [31–33]. Despite first dilute and inject attempts to reduce the time-consuming sample preparation [34–39], UHPLC-MS/MS analyses still often utilizes extensive sample preparation to separate the molecule of interest from interfering proteins and potential enzymatic degradation processes [40]. Our method (A) used for quantitation of docetaxel was successfully validated in terms of selectivity, carry-over, lower limit of quantitation (LLOQ), calibration function, accuracy, and precision according to EMA guidelines for bioanalytical method validation. A very broad concentration range of 1–10,000 ng/mL was covered compared to already published methods [20,41], allowing the analysis of docetaxel administered ranging from 7 to 7000 ng/mL. The method proved to be accurate and precise, showed acceptable carry-over after including blank injections between high and low concentration samples, as well as fitness-for purpose in LLOQ. Furthermore, the method was fast, being able to separate docetaxel and 7-epi-docetaxel in less than 3.7 min (total run-time including cleaning of injector 9.75 min).

Future studies will compare differences between the patients' drug responses and drug delivery systems to optimize the dose regimen and application form. For increased efficacy, model size and sampling volume may be further optimized in the direction of high-throughput, and therefore, enhance personalized medicine.

5. Conclusions

We developed and evaluated a real-time approach to automatically measure docetaxel concentrations in TOM models. Partial epimerization and neglectable amounts of degradation products were detected instantaneously upon application of docetaxel to the medium. The courses of concentration versus time curves for 96 h were comparable among four different docetaxel concentrations. The first drug application resulted in an increase of docetaxel concentration, followed by a plateau phase, and exceeded after the second drug application. This proof-of-concept study paves the way for real-time pharmacokinetic and further online investigations in 3D tumor models and beyond, and thus, helps to improve preclinical drug development and personalized medicine.

Supplementary Materials: The following are available online at http://www.mdpi.com/1999-4923/12/5/413/s1, Figure S1: Multiple reaction monitoring (MRM) chromatogram, Figure S2: Overlay of extracted ion chromatograms of docetaxel and degradation products, Figure S3: Product ion spectra of degradation products, Figure S4:

Suggested chemical structure of docetaxel and degradation products, structural differences in comparison to docetaxel are displayed in red color.

Author Contributions: Conceptualization, J.F.J., L.G., B.W., C.Z., and M.K.P.; methodology, J.F.J., L.G., B.W., C.Z., and M.K.P.; validation, J.F.J., L.G., and C.Z.; formal analysis, J.F.J., L.G. and C.Z.; investigation, J.F.J., L.G., J.G., L.M.C..; resources, C.Z., U.K., M.K.P.; data curation, J.F.J., L.G., J.G.-M., L.M.C.; writing—original draft preparation, J.F.J., L.G., C.Z.; writing—review and editing, J.F.J., L.G., U.K., C.Z., M.K.P.; visualization, J.F.J., L.G., J.G., C.Z.; supervision, C.Z., M.K.P.; project administration, U.K., C.Z., M.K.P.; funding acquisition, C.Z., U.K., M.K.P. All authors have read and agreed to the published version of the manuscript.

Funding: This research was funded by the Freie Universität Berlin (Focus Area Disease in Human Aging, "DynAge").

Acknowledgments: The authors thank Kathleen Sauvetre, Université Angers, France, for technical help with the sampling port and Luis Ilia, Freie Universität Berlin, Germany, for help with the pharmacokinetic analyses. The publication of this article was funded by Freie Universität Berlin.

Conflicts of Interest: The authors declare no conflict of interest. The funders had no role in the design of the study; in the collection, analyses, or interpretation of data; in the writing of the manuscript, or in the decision to publish the results.

References

1. Horvath, C.J.; Milton, M.N. The TeGenero incident and the Duff Report conclusions: A series of unfortunate events or an avoidable event? *Toxicol. Pathol.* **2009**, *37*, 372–383. [CrossRef] [PubMed]
2. Zou, P.; Yu, Y.; Zheng, N.; Yang, Y.; Paholak, H.J.; Yu, L.X.; Sun, D. Applications of Human Pharmacokinetic Prediction in First-in-Human Dose Estimation. *AAPS J.* **2012**, *14*, 262–281. [CrossRef] [PubMed]
3. Andrade, E.L.; Bento, A.F.; Cavalli, J.; Oliveira, S.K.; Schwanke, R.C.; Siqueira, J.M.; Freitas, C.S.; Marcon, R.; Calixto, J.B. Non-clinical studies in the process of new drug development—Part II: Good laboratory practice, metabolism, pharmacokinetics, safety and dose translation to clinical studies. *Braz. J. Med. Biol. Res.* **2016**, *49*, e5646. [CrossRef] [PubMed]
4. Nie, L.; Rubin, E.H.; Mehrotra, N.; Pinheiro, J.; Fernandes, L.L.; Roy, A.; Bailey, S.; de Alwis, D.P. Rendering the 3 + 3 Design to Rest: More Efficient Approaches to Oncology Dose-Finding Trials in the Era of Targeted Therapy. *Clin. Cancer Res.* **2016**, *22*, 2623–2629. [CrossRef]
5. Jang, S.H.; Wientjes, M.G.; Lu, D.; Au, J.L. Drug delivery and transport to solid tumors. *Pharm. Res.* **2003**, *20*, 1337–1350. [CrossRef]
6. Dewhirst, M.W.; Secomb, T.W. Transport of drugs from blood vessels to tumour tissue. *Nat. Rev. Cancer* **2017**, *17*, 738–750. [CrossRef]
7. Saleem, A.; Price, P.M. Early tumor drug pharmacokinetics is influenced by tumor perfusion but not plasma drug exposure. *Clin Cancer Res* **2008**, *14*, 8184–8190. [CrossRef]
8. Jang, S.H.; Wientjes, M.G.; Au, J.L. Determinants of paclitaxel uptake, accumulation and retention in solid tumors. *Invest. New Drugs* **2001**, *19*, 113–123. [CrossRef]
9. Fang, Y.; Eglen, R.M. Three-Dimensional Cell Cultures in Drug Discovery and Development. *SLAS Discov* **2017**, *22*, 456–472. [CrossRef]
10. Schütte, M.; Risch, T.; Abdavi-Azar, N.; Boehnke, K.; Schumacher, D.; Keil, M.; Yildiriman, R.; Jandrasits, C.; Borodina, T.; Amstislavskiy, V.; et al. Molecular dissection of colorectal cancer in pre-clinical models identifies biomarkers predicting sensitivity to EGFR inhibitors. *Nat. Commun.* **2017**, *8*, 14262. [CrossRef]
11. Wang, Q.; Zhang, J.; Pi, Z.; Zheng, Z.; Xing, J.; Song, F.; Liu, S.; Liu, Z. Application of online microdialysis coupled with liquid chromatography-tandem mass spectrometry method in assessing neuroprotective effect of Rhizoma coptidis on diabetic rats. *Anal. Methods* **2015**, *7*, 45–52. [CrossRef]
12. Graf, C.; Rühl, E. Imaging Techniques for Probing Nanoparticles in Cells and Skin. In *Biological Responses to Nanoscale Particles*; Springer: Berlin, Germany, 2019; pp. 213–239.
13. Rheinwald, J.G.; Beckett, M.A. Tumorigenic keratinocyte lines requiring anchorage and fibroblast support cultured from human squamous cell carcinomas. *Cancer Res* **1981**, *41*, 1657–1663. [PubMed]
14. Gronbach, L.; Wolff, C.; Klinghammer, K.; Stellmacherc, J.; Jurmeisterd, P.; Alexievc, U.; Schäfer-Kortinga, M.; Tinhofer, I.; Keilholz, U.; Zoschke, C. A multilayered epithelial mucosa model of head neck squamous cell carcinoma for analysis of tumor-microenvironment interactions and drug development. *Clin. Cancer Res.*. (in revision).

15. EMA. Guideline on Bioanalytical Method Validation. 2011. Available online: ema.europa.eu/en/documents/scientific-guideline/guideline-bioanalytical-method-validation_en.pdf (accessed on 2 February 2020).
16. EMA. ICH Topic Q 2 (R1) Validation of Analytical Procedures: Text and Methodology. 1995. Available online: ema.europa.eu/en/documents/scientific-guideline/ich-q-2-r1-validation-analytical-procedures-text-methodology-step-5_en.pdf (accessed on 2 February 2020).
17. R Development Core Team. *R: A Language and Environment for Statistical Computing*; R Foundation for Statistical Computing: Vienna, Austria, 2019.
18. Rao, B.M.; Chakraborty, A.; Srinivasu, M.K.; Devi, M.L.; Kumar, P.R.; Chandrasekhar, K.B.; Srinivasan, A.K.; Prasad, A.S.; Ramanatham, J. A stability-indicating HPLC assay method for docetaxel. *J. Pharm. Biomed. Anal.* **2006**, *41*, 676–681. [CrossRef]
19. Kumar, D.; Tomar, R.S.; Deolia, S.K.; Mitra, M.; Mukherjee, R.; Burman, A.C. Isolation and characterization of degradation impurities in docetaxel drug substance and its formulation. *J. Pharm. Biomed.* **2007**, *43*, 1228–1235. [CrossRef]
20. Yamaguchi, H.; Fujikawa, A.; Ito, H.; Tanaka, N.; Furugen, A.; Miyamori, K.; Takahashi, N.; Ogura, J.; Kobayashi, M.; Yamada, T.; et al. A rapid and sensitive LC/ESI–MS/MS method for quantitative analysis of docetaxel in human plasma and its application to a pharmacokinetic study. *J. Chromatogr. B Biomed. Appl.* **2012**, *893-894*, 157–161. [CrossRef]
21. Smith, M.A.; Houghton, P. A proposal regarding reporting of in vitro testing results. *Clin. Cancer Res.* **2013**, *19*, 2828–2833. [CrossRef]
22. Liston, D.R.; Davis, M. Clinically Relevant Concentrations of Anticancer Drugs: A Guide for Nonclinical Studies. *Clin. Cancer Res.* **2017**, *23*, 3489–3498. [CrossRef]
23. EMA. European Public Assessment Report "TAXOTERE", Annex I—Summary of Product. 2019. Available online: ema.europa.eu/documents/product-information/taxotere-epar-product-information_en.pdf (accessed on 2 February 2020).
24. Mohsin, S.; Arellano, I.H.; Choudhury, N.R.; Garg, S. Docetaxel epimerization in silicone films: A case of drug excipient incompatibility. *Drug Test. Anal.* **2014**, *6*, 1076–1084. [CrossRef]
25. Vuilhorgne, M.; Gaillard, C.; Sanderink, G.J.; Royer, I.; Monsarrat, B.; Dubois, J.; Wright, M. Metabolism of Taxoid Drugs. In *Taxane Anticancer Agents*; American Chemical Society: Washington, DC, USA, 1994; Volume 583, pp. 98–110.
26. Tian, J.; Stella, V.J. Degradation of paclitaxel and related compounds in aqueous solutions I: Epimerization. *J. Pharm. Sci.* **2008**, *97*, 1224–1235. [CrossRef]
27. Song, D.; Hsu, L.F.; Au, J.L. Binding of taxol to plastic and glass containers and protein under in vitro conditions. *J. Pharm. Sci.* **1996**, *85*, 29–31. [CrossRef] [PubMed]
28. Schuck, V.J.; Rinas, I.; Derendorf, H. In vitro microdialysis sampling of docetaxel. *J Pharm. Biomed. Anal.* **2004**, *36*, 807–813. [CrossRef] [PubMed]
29. Baumann, K.Y.; Church, M.K.; Clough, G.F.; Quist, S.R.; Schmelz, M.; Skov, P.S.; Anderson, C.D.; Tannert, L.K.; Giménez-Arnau, A.M.; Frischbutter, S.; et al. Skin microdialysis: methods, applications and future opportunities—An EAACI position paper. *Clin. Transl. Allergy* **2019**, *9*, 24. [CrossRef] [PubMed]
30. Pasqua, O.E.D. PKPD and Disease Modeling: Concepts and Applications to Oncology. In *Clinical Trial Simulations: Applications and Trends*; Kimko, H.H.C., Peck, C.C., Eds.; Springer: New York, NY, USA, 2011; pp. 281–306. [CrossRef]
31. Patteet, L.; Maudens, K.E.; Stove, C.P.; Lambert, W.E.; Morrens, M.; Sabbe, B.; Neels, H. The use of dried blood spots for quantification of 15 antipsychotics and 7 metabolites with ultra-high performance liquid chromatography - tandem mass spectrometry. *Drug Test. Anal.* **2015**, *7*, 502–511. [CrossRef]
32. Rodriguez-Aller, M.; Gurny, R.; Veuthey, J.L.; Guillarme, D. Coupling ultra high-pressure liquid chromatography with mass spectrometry: constraints and possible applications. *J. Chromatogr. A* **2013**, *1292*, 2–18. [CrossRef]
33. Novakova, L.; Pavlik, J.; Chrenkova, L.; Martinec, O.; Cerveny, L. Current antiviral drugs and their analysis in biological materials—Part II: Antivirals against hepatitis and HIV viruses. *J Pharm. Biomed. Anal.* **2018**, *147*, 378–399. [CrossRef]

34. Gorgens, C.; Guddat, S.; Schanzer, W.; Thevis, M. Screening and confirmation of myo-inositol trispyrophosphate (ITPP) in human urine by hydrophilic interaction liquid chromatography high resolution / high accuracy mass spectrometry for doping control purposes. *Drug Test. Anal.* **2014**, *6*, 1102–1107. [CrossRef]
35. Ambrosio, G.; Joseph, J.F.; Wuest, B.; Mazzarino, M.; de la Torre, X.; Diel, P.; Botre, F.; Parr, M.K. Detection and quantitation of ecdysterone in human serum by liquid chromatography coupled to tandem mass spectrometry. *Steroids* **2020**, *157*, 108603. [CrossRef]
36. Holder, B.R.; McNaney, C.A.; Luchetti, D.; Schaeffer, E.; Drexler, D.M. Bioanalysis of acetylcarnitine in cerebrospinal fluid by HILIC-mass spectrometry. *Biomed. Chromatogr.* **2015**, *29*, 1375–1379. [CrossRef]
37. Kong, T.Y.; Kim, J.H.; Kim, J.Y.; In, M.K.; Choi, K.H.; Kim, H.S.; Lee, H.S. Rapid analysis of drugs of abuse and their metabolites in human urine using dilute and shoot liquid chromatography-tandem mass spectrometry. *Arch. Pharm. Res.* **2017**, *40*, 180–196. [CrossRef]
38. Bourgogne, E.; Wagner, M. [Sample preparation and bioanalysis in mass spectrometry]. *Ann. Biol. Clin. (Paris)* **2015**, *73*, 11–23. [CrossRef] [PubMed]
39. Parr, M.K.; Ambrosio, G.; Wuest, B.; Mazzarino, M.; de la Torre, X.; Sibilia, F.; Joseph, J.F.; Diel, P.; Botrè, F. Targeting the Administration of Ecdysterone in Doping Control Samples. *bioRxiv* **2019**. [CrossRef]
40. Plock, N.; Kloft, C. Microdialysis–theoretical background and recent implementation in applied life-sciences. *Eur. J. Pharm. Sci.* **2005**, *25*, 1–24. [CrossRef] [PubMed]
41. Hendrikx, J.J.; Hillebrand, M.J.; Thijssen, B.; Rosing, H.; Schinkel, A.H.; Schellens, J.H.; Beijnen, J.H. A sensitive combined assay for the quantification of paclitaxel, docetaxel and ritonavir in human plasma using liquid chromatography coupled with tandem mass spectrometry. *J. Chromatogr. B Analyt. Technol. Biomed. Life Sci.* **2011**, *879*, 2984–2990. [CrossRef]

pharmaceutics MDPI

Supplementary Materials: Automated Real-Time Tumor Pharmacokinetic Profiling in 3D Models: A Novel Approach for Personalized Medicine

Jan F. Joseph, Leonie Gronbach, Jill García-Miller, Leticia M. Cruz, Bernhard Wuest, Ulrich Keilholz, Christian Zoschke and Maria K. Parr

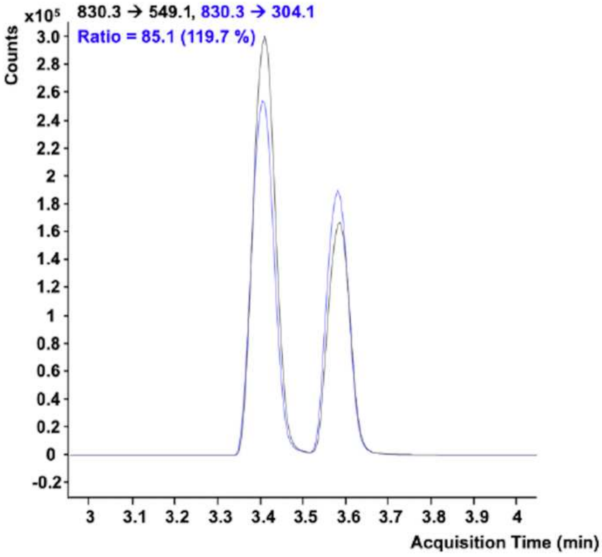

Figure S1. Multiple reaction monitoring (MRM) chromatogram. Product ions of docetaxel (left peak) and epi-docetaxel (right peak) acquired using method A.

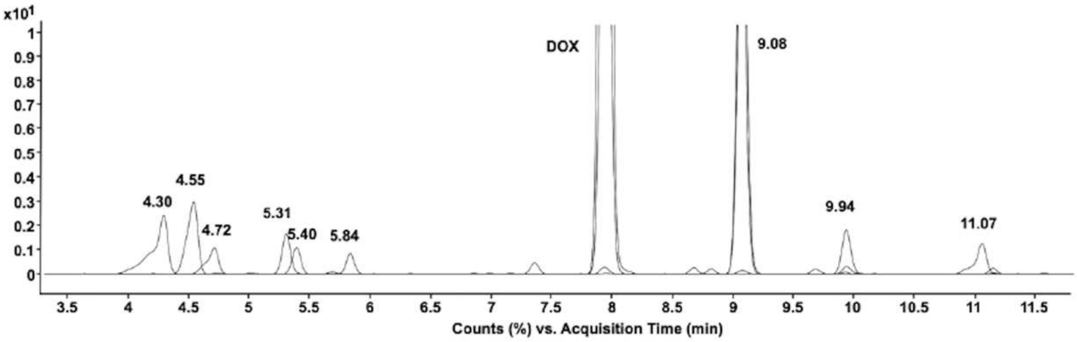

Figure S2. Overlay of extracted ion chromatograms of docetaxel and degradation products, acquired using method B.

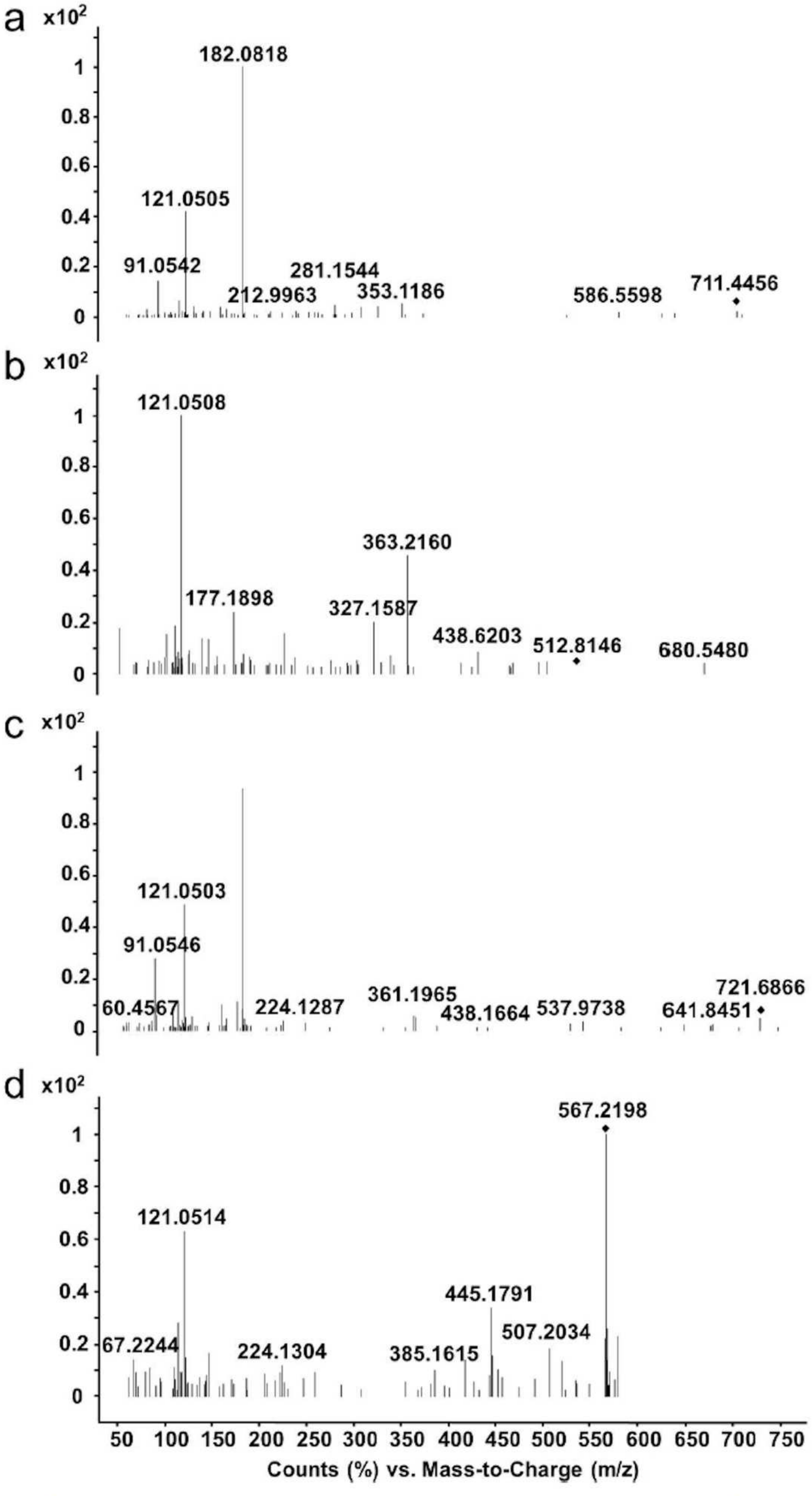

Figure S3. Product ion spectra of degradation products acquired using method B. (**a**) Carbamate (RT: 4.30 min, precursor $[M+H]^+$=708.3010), (**b**) 10-deacetyl baccatin III (RT: 4.55 min, precursor $[M+H]^+$=545.2378), (**c**) epi-carbamate (RT: 4.72 min, precursor $[M+H]^+$=708.3004), (**d**) 7-epi-10-deacetyl baccatin (RT: 5.31 min, precursor $[M+Na]^+$=567.2196).

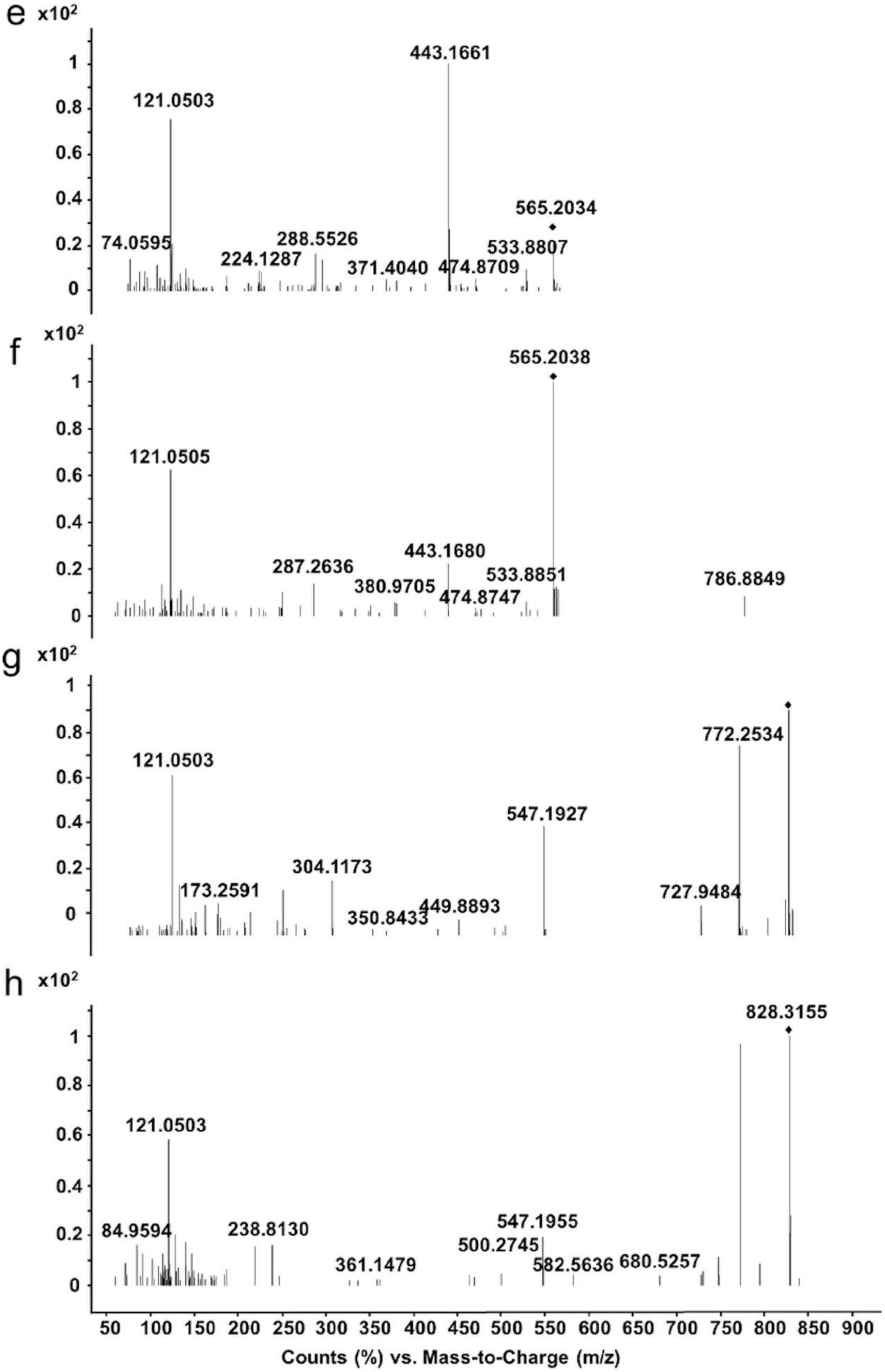

Figure S3. (continued). Product ion spectra of degradation products acquired using method B. (**e**) 10-oxo-10-deacetyl baccatin III (RT: 5.40 min, precursor $[M+Na]^+=565.2041$), (**f**) 7-epi-10-oxo-10-deacetyl baccatin III (RT: 5.84 min, precursor $[M+Na]^+=565.2040$), (**g**) 10-oxo-docetaxel (RT: 9.94 min, precursor $[M+Na]^+=828.3200$), (**h**) 7-epi-10-oxo-docetaxel (RT: 11.07 min, precursor $[M+Na]^+=828.3192$).

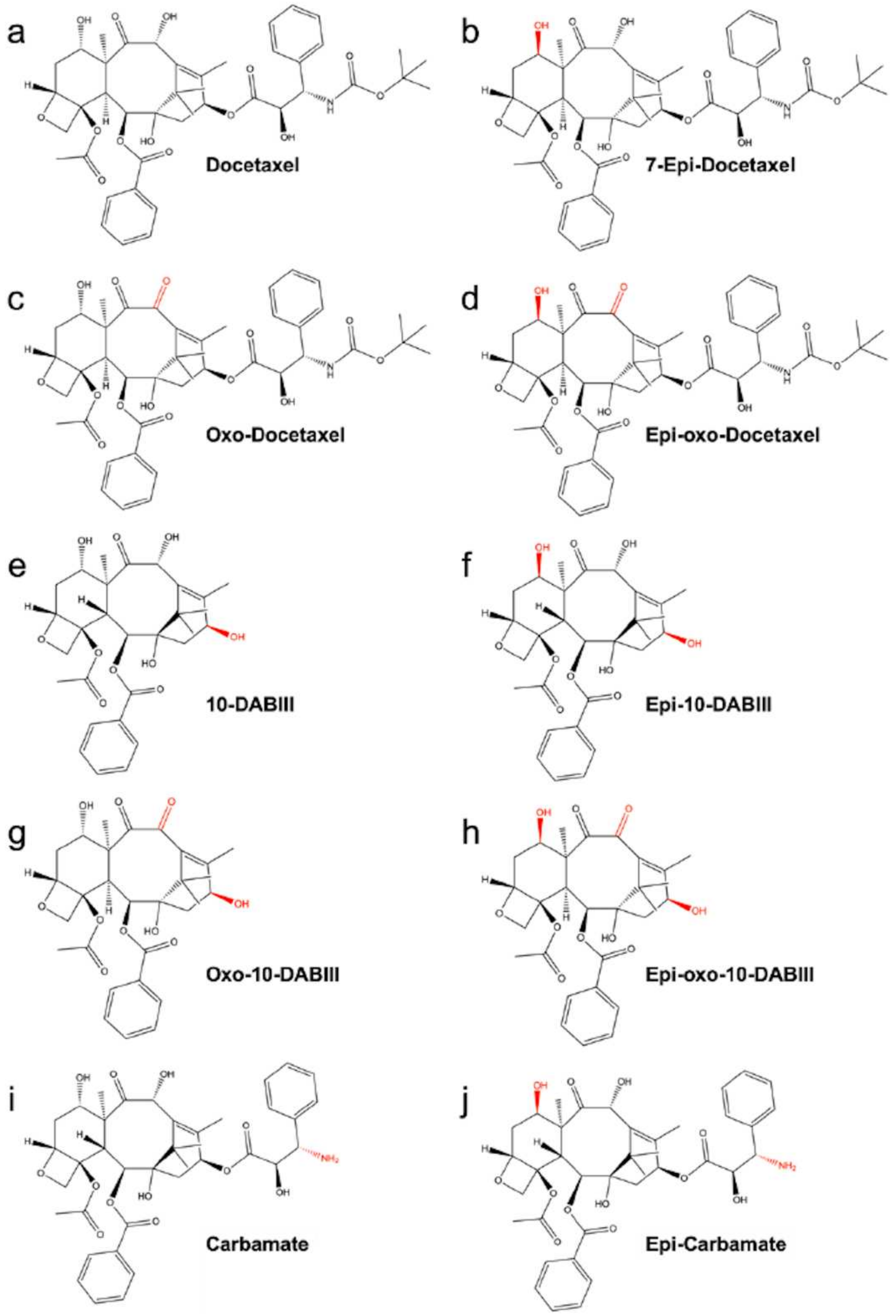

Figure S4. Suggested chemical structure of docetaxel and degradation products, structural differences in comparison to docetaxel are displayed in red color.

5. Discussion

5.1 General Discussion

Head and neck squamous cell carcinomas represent a highly aggressive, heterogeneous group of cancers, which makes them difficult to treat. The current therapy options are associated with high toxicity, resistance, and low efficiency. Due to the current status, the overall aim of this thesis was to establish and assess tissue-engineered 3D NOM and TOM models, for advanced drug predictions in preclinical drug testing, for improved HNSCC therapy.

In the field of tissue engineering, the aim is always to build up a tissue, that mimics the *in vivo* situation as close as possible. But, a complete recapitulation of the *in vivo* situation will probably never be achieved, as the famous aphorism from statistician George Cox "all models are wrong, but some are useful" (102), also can be transferred to tissue-engineered models. This implies, that we should concentrate on the question "is the model good enough for each respective application?", rather than on "is the model true?", because it never will. Therefore, it is important to identify the essential characteristics the model has to have, to answer specific research questions. Additionally, it is of equal importance, to know as well about the limitations of the model. And we also have to keep in mind that, as Paul Valéry said, "What is simple is always wrong. What is not is unusable" (103), meaning the best model will be useless if it is too difficult to build it. In the following, the previously presented results, which are discussed in detail in chapters 2-4, are taken into the perspective of advanced preclinical drug testing by revealing the models' opportunities and limitations.

3D NOM and TOM models closely reflect the *in vivo* morphology The search for good models, recapitulating the main characteristics of human oral mucosa and HNSCC, to improve drug testing, was part of this thesis. Hereby, the cell source is of big importance, since the cells are the main actors in the model. Available NOM models are sometimes built with squamous cell carcinoma cell lines as the SkinEthic™ HOE/Human Oral Epithelium model from SkinEthic, due to the limited number of available normal oral keratinocytes. But, to build a healthy NOM model out of tumor cells, which should later be compared to TOM models, to elucidate tumor-associated effects, would be highly misleading. Or a NOM model, only composed of an epithelial layer, would fail to answer essential questions about the cellular crosstalk.

The here presented NOM models are by morphology and composition similar to other published full-thickness models (92, 104), and count, due to their composition of human, primary, oral fibroblasts, and keratinocytes, to more advanced NOM models. The models nicely presented the characteristic cell layers and protein patterns of lining oral mucosa, as seen by the laminin-332 and cytokeratin-13 markers. The epithelial thickness however was thinner compared to the *in vivo* situation and might be accelerated by improvements of the scaffold, as the integration of elastin-like recombinant polymers (105). Furthermore, high reproducibility, robustness, and good handling characteristics give evidence, that these models might be a good opportunity for preclinical drug testing.

HNSCC *in vitro* models have been built at various stages of carcinogenesis, ranging from mild dysplasia to invasively growing cancer cells (106, 107). Thereby, diverse cancer cell lines have predominantly been used (107), as cancer cell counts from surgical procedures remain low. In this study, I used both, two cell lines from the tongue and hypopharynx and two primary cancer cell types from the tongue and oral cavity, derived in xenografts with various tumor gradings.

All tumor models are highly distinguished from the NOM models in their physiological composition and protein pattern, as diffuse cell stratification and characteristically higher proliferation (Ki-67), resulting in increased epithelial layer thickness. This underlines the usability of the NOM models as a healthy control in preclinical drug testing. Additionally, it came out, that differences in the tumor grading of various tumor cell types could be reflected in the established TOM models as well. So, tumor types of higher grade depicted increased heterogeneity and tumor thickness. Due to the fact, that the tumor cells aren´t changed in their morphology and protein expression, which is very important for the model's validity, these models set the basis for a more complex test platform with the aim of personalized medicine. Concerning the good reproducibility and unlimited availability, the tumor cell line models could serve as a model for advanced preclinical drug testing.

Changes in the microenvironment and ECM influence morphology and longevity The immense influence of the microenvironment on the cells' behavior, as their morphology and protein expression, was recognized decades ago (108). The age and origin of the fibroblasts for example can change the morphology and protein expression of the keratinocytes in 3D skin models considerably (109). Especially in the tumor tissue, the ECM has a high impact on cancer progression, invasion, and drug response (110). This is the reason, why it is of big importance to also integrate normal cells into the 3D-tumor model and to choose the matrix components wisely. In 3D skin models, the replacement of collagen with the hyalograft 3D$^{®}$ technology in the scaffold, improved the tissue stability, differentiation, and homeostasis, leading to increased model longevity (111). The longevity sets the time frame for the drug application, model reactions, and the detection of possible tumor cell re-growth in drug testing experiments. But, most used models, as 2D-cell culture, only have a lifespan of maximal one to two weeks (112), and many preclinical drug evaluation studies only consider a time frame of a few hours or days (113). Here, important information on tumor recurrence and resistance can get lost. There are only a few long-term cultured models published and these are often associated with long pre-cultivation times (4-5 weeks) and difficult sample analysis due to the hardness (nylon mesh) or fragility of the matrix material (114, 115).

In this thesis, the hyalograft 3D approach could be implemented to the NOM and TOM models with similar morphology and protein pattern. Interestingly, the wound marker tenascin C could be reduced in both hyalograft models, which is an advantage since model- and not tumor-dependent tenascin c might distort drug responses. The constant proliferation of the tumor cells in the 7 weeks cultured hyalograft-TOM models gives evidence for an elongated lifetime and the hyalograft models were more stable compared to the collagen models, which tend to shrink over time (116). Nevertheless, the tumor cells as well as the normal oral keratinocytes needed more time to grow, which could be seen by their thinner epithelial layer after two weeks of culture. To conclude, the hyalograft-based models offer the opportunity, to grow NOM and TOM models without the influences of bovine collagen. Moreover, hyalograft-based models allow long-term cultivation of tumors which will be interesting to study pharmacodynamics and tumor re-growth following initial drug treatment. However, the collagen-based models tend to be the better option for short-termed experiments, since the models faster reflect the *in vivo* morphology.

Future studies should investigate the replacement of fetal calf serum to generate a fully human tumor model. Besides the ethical aspect, the composition of fetal calf serum varies from batch to batch and thus reduces the reproducibility of the experiments (117). Furthermore, the cultivation time limit of these models has to be determined and the model's potential, as a drug testing platform, validated.

Docetaxel effects are reflected in 3D NOM and TOM models with higher topical effects

The most important characteristic of a drug testing model is a very close recapitulation of the patients' drug response. Docetaxel, as one of the gold standard chemotherapeutics in HNSCC therapy, belongs to the most effective drugs against HNSCC by today. To prove the here established models towards their ability to closely reflect patients' drug responses, docetaxel was chosen as a first test drug. For the first time, the cytotoxic effect of docetaxel was tested on 3D NOM and TOM models by various application forms and doses. In breast and prostate cancer spheroids, it could already be demonstrated, that docetaxel, like many other drugs, cause lower drug effects compared to 2D-cell culture (118-120), due to the common hypersensitivity to chemotherapeutics and poor resistance prevalence in 2D-cell culture. Docetaxel could also show its intense cytotoxic effects in the TOM models with the SCC-25 and UM-SCC-22B cell line, as it was shown for various xenografts before (40). Hereby, the drug effects could be detected from many sides of the model, like the thickness, morphology, and protein pattern from the model itself, but as well released proteins from the cells into the medium served as response markers. The cytotoxic effects of docetaxel were reflected in TOM models by decreased tumor thickness, Kiel-67 (Ki-67), and hypoxia-inducible factor 1α (HIF-1α) levels, increased LDH, and IL-6 levels in the media, as well as induced apoptosis and modified patterns in laminin-332. Due to the good response rate of TOM models to docetaxel and the possibility to detect a variety of meaningful markers, as well as tumor-stroma interactions, TOM models presented their potential to predict patient drug responses. Interestingly, the NOM models did not show significant drug responses, which indicates weak side effects of the tumor's normal tissue surrounding.

The layered architecture of the TOM models furthermore enabled different application sites as systemic (underneath the model) and topical (on top of the model) application, which is impossible in other 3D models, as spheroids. Remarkably, the topical treatment showed tendential earlier effects with lower dosing in tumor thickness, LDH, and IL-6, compared to systemic treatment, offering a new potential therapeutic strategy. To date, there is no topical treatment option in HNSCC therapy, although systemic side effects already could be reduced by topical treatment in the therapy of actinic keratosis, compared to previous therapy options (121). A topical treatment option in HNSCC therapy could as well reduce systemic toxicities and spare important anatomical structures, like the liver, blood, and nervous system, by acting directly at the tumor site with less necessary doses. Since the oral cavity offers accessibility, a great blood supply, normally rapid repair, and a good permeability profile, a topical treatment option could also be a great opportunity in the head and neck cancer therapy management, with higher drug efficiency (122). A topical treatment further could be used as a neoadjuvant chemotherapy option to reduce the size of non-resectable tumors, or in palliative care to increase the time and quality of life.

Patients with HNSCC of the oral cavity would profit most from a topical application since this is the best accessible region, in the head and neck and the carcinoma incidence is the highest among HNSCC. The salivary washout and local high enzyme activity pose the major challenges for the development of a drug delivery system for local tumor treatment.

Several topical drug delivery systems have already been developed, as mucoadhesive gels, patches, or electrospinning (123, 124), which in future studies would have to be adopted to guarantee a safe and efficient application form in topical anti-cancer treatment.

3D oral mucosa models enable automated real-time drug concentration measuring To find out a safe and efficient drug dose of a new anti-cancer drug, pharmacodynamic values as the maximally tolerated dose, are traditionally first determined in animals and then transferred to humans (125). These preclinical animal toxicity experiments are effortful, and the results are often difficult to transfer to humans correctly. To save money and time, an efficient preclinical drug testing platform, which elucidates precisely the drug concentrations inside the target tissue and depicts the caused drug effects on a human tissue, would be of great advantage. In this thesis, a completely new approach was designed, to measure drug concentrations in real-time, in an automated and effortless way in 3D TOM models, as a first proof-of-concept.

The enablement of fully automated drug detection without sample pretreatment for urine, plasma, and saliva was published in 1981, by integrating a pre-column into HPLC measurements (126). But still, there is no available system that allows for drug quantifications inside a human tissue in real-time. The here presented approach has the advantage to be made of human cells and the possibility to measure drug concentrations inside the tumor tissue automated, and in real-time, without additional sample handling. Furthermore, the drug amounts are measured directly in the extracellular liquid of the tumor tissue, as it is done in microdialysis approaches and not in the blood plasma or urine, which allows for improved evidence of the drug concentration at the target site.

The here presented approach was able to measure docetaxel’s access in the 3D TOM models, by sensitively detecting docetaxel concentrations in real-time. Also, metabolites and isomers of docetaxel could be detected in the model medium. But, noticeable differences in the concentration-time curves of different model-batches could be seen, especially in the lower docetaxel concentrations, which might arise from differences in model contraction and a starting contact loss from the sample port to the model. A constant contact between the model and the sample port has to be guaranteed for correct drug concentration detection since the drug concentrations will be falsified if the drug can´t reach the sample port anymore. In future studies, matrices that don´t contract, as the presented hyalograft approach, could enable more stable replication, and an adopted elimination constant should be considered for trough value and area under the curve (AUC) predictions. This possibly could be achieved by the integration of a flow system of the media. Since a wider range of docetaxel metabolites was found in human liver microsomes, than in TOM models (unpublished own observations in cooperation with Prof. Parr), the connection of TOM models with liver tissue, would further allow for drug metabolism studies. Therefore, the size of TOM models should be decreased, from a 12-well to a 24-well approach, which enables the integration of TOM models into organ-on-a-chip approaches. In the process of downsizing the models, the resulting possibility to integrate patient-derived tumor cells might be also a helpful tool for personalized medicine studies.

Cetuximab can be localized in the tumor stroma Cetuximab, the first targeted therapeutic against HNSCC, and the second used drug in this work did in contrast to docetaxel not lead to any changes in the used markers, predicting no cytostatic, nor cytotoxic effects in our models. These findings correspond to the low response rates in clinical trials with a time-to-treatment failure range of only 5 months (30, 127). In PDXs, however, cetuximab showed promising response rates of 79% (40), which appear misleading considering the patients' responses. Although several findings on resistance mechanisms were made, e.g. the expression of the EGFR-K_{521} polymorphism which is expressed in >40% of HNSCC patients and results in a lower cetuximab affinity (128), or compensation of the inhibitory effect of cetuximab by increased activity of the human epidermal growth factor receptor 3 and insulin-like growth factor 1 receptor (129), the resistance mechanisms are still not fully understood.

As mentioned before, cetuximab did not lead to tumor reduction, nor a reduced tumor proliferation in the presented TOM models, whereby cetuximab in contrast led to a remarkable reduction in living cells in monolayer experiments. To elucidate the reason for the ineffectiveness of a drug, first of all, it has to be guaranteed, that the drug reaches its target site. Therefore, quantitative information on the drug distribution within the tumor and its environment would be of big interest. There are numerous established methods for drug detection. When labeled with a fluorescent dye, cetuximab was found to be localized in EGFR- and oxygen-rich regions, while absent in well-differentiated tumors (130, 131). Our fluorescence lifetime imaging technique (FLIM) measurements showed that cetuximab specifically binds to the cell membrane in monolayer cell culture. And also, in the TOM models, the FLIM results nicely proved the penetration of the fluorescence tagged cetuximab, into the entire tumor tissue, both after systemic and topical administration. Thus, the low efficacy of cetuximab in 3D TOM models is not related to insufficient drug accumulation in the tumor but results from the drug resistance of the tumor cells.

The localization and quantification of drugs and other molecules of interest like metabolites often require the bindings to a label, as in autoradiography, positron emission tomography, or the cluster-based FLIM (62). The impact of this chemical modification on the physicochemical and pharmacokinetic properties of the drug depends on the drug itself. For example, the modification of small molecules like docetaxel would exceed the change of monoclonal antibodies like cetuximab. However, the labeling always goes along with the risk of unknown labeling-stoichiometry and stability. To overcome these limitations, label-free approaches should be considered.

Mass spectrometry imaging (MSI) (132, 133), scanning transmission X-ray microscopy (134) or optical coherence tomography (OCT) (135) are label-free techniques. Nevertheless, these methods have limitations like low reproducibility, intense sample preparation, invasive irritations to the sample, and limited chemical contrast (134-137). Here, the atomic force microscopy-based infrared spectroscopy (AFM-IR) belongs to the techniques with the highest resolution, and the higher affinity to the EGFR of cetuximab compared to EGF was already shown by AFM in lung cells (138).

In cooperation with the workgroup of Prof. Eckart Rühl, cetuximab could as well be detected by label-free AFM-IR measurements in the 3D TOM models. These measurements have been performed and analyzed by Gregor Germer as part of his doctoral thesis. For the atomic force microscopy-based photothermal expansion spectroscopy analysis, measurements of the single components of a model slice, used as references, had to be performed. This included PBS, cetuximab in PBS, cryomedium, silicon substrate, and lastly the untreated tumor model sample (Figure 6a). Then, topography and a hyperspectral imaging recording of the full spectral information in each pixel of a selected tumor cell of a control model and a cetuximab treated model have been measured (Figure 6c). Already by subtracting the spectra of the single reference components from the spectra of the treated tumor cells distinct differences could be observed (black line in Figure 6b). This biological variance might be the result of molecular changes in the cell caused by cetuximab. For a more detailed analysis, the singular value decomposition (SVD) evaluation method was applied to the experimental data (139). Hereby, a pre-factor calculation allowed us to find a weight factor of cetuximab's specific spectrum, corresponding to the local drug concentration, to fit it to the full spectral information of the treated tumor cell. The hyperspectral imaging together with the SVD yielded the detection of cetuximab inside a single tumor cell, with a spatial resolution of 100 and 300 nm, respectively. Here, the 300 nm resolution turned out to be sufficient to identify cetuximab concentration distributions in a single cell and will be used for the next measurements.

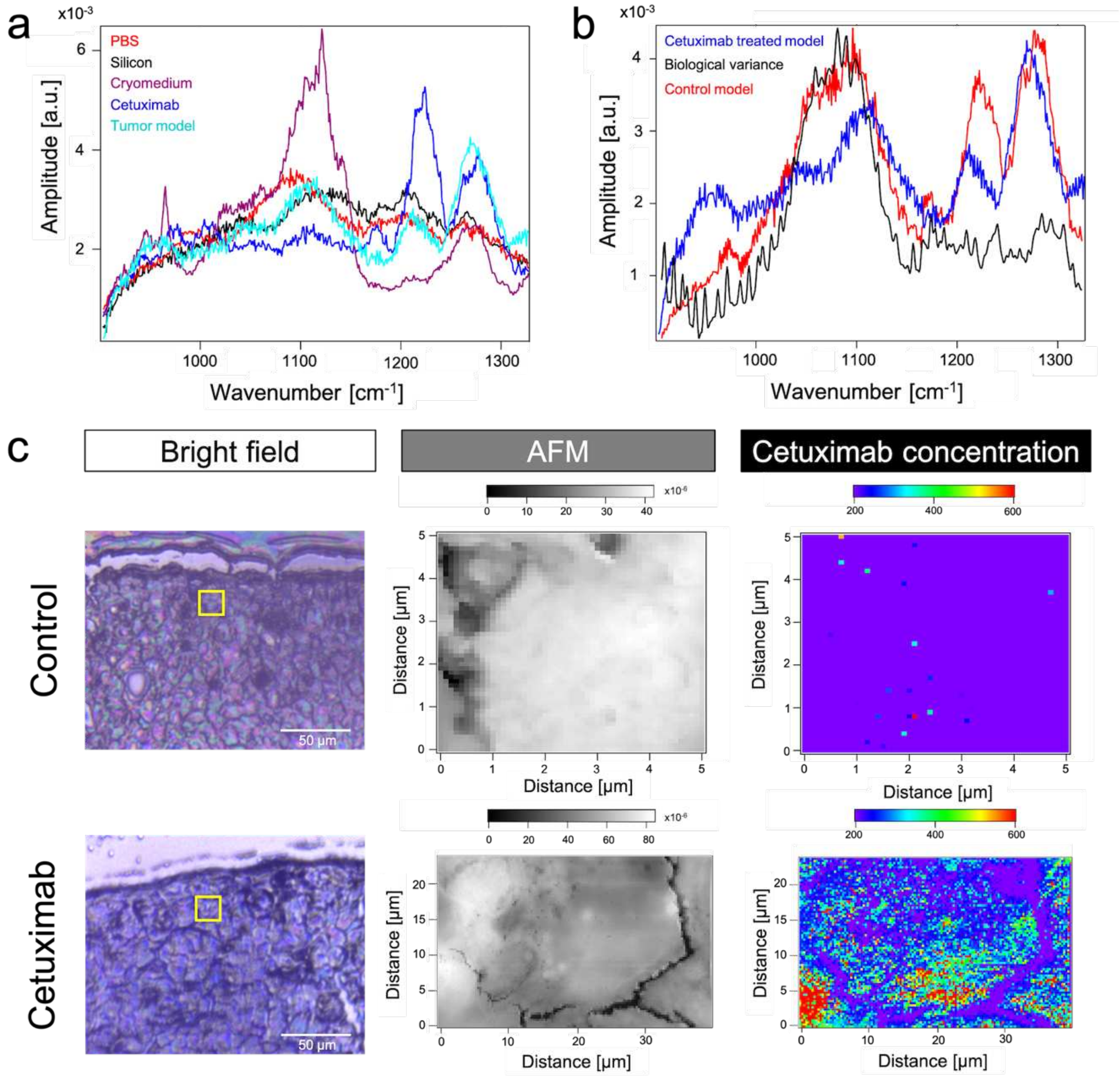

Figure 6 First results on probing of cetuximab within TOM models by atomic force microscopy infrared spectroscopy (AFM-IR) a) photothermal expansion spectra of the single components of the model substrates: PBS (red), silicon substrate (black), cryomedium (pink), cetuximab (blue), and tumor model (light blue) in the range of 900 cm^{-1} to 1316 cm^{-1}; b) AFM-IR spectra of a single cell position in the control model (blue) and in the cetuximab treated model (red), and the biological variance (black) when subtracting single component spectra from the treated model spectra; c) bright-field images of the control model and cetuximab treated model, with marked single tumor cell areas (left), and (right) corresponding AFM topography (grey image), and the calculated local cetuximab concentration as derived from hyperspectral imaging and singular value decomposition within a single cell with a spatial resolution of 100 nm for the control model and 300 nm for the treated model (rainbow scale image). In collaboration with the workgroup of Prof. Dr. E. Rühl and Dr. C. Zoschke (both from Freie Universität Berlin).

In the following, the same hyperspectral imaging measurements together with SVD calculations have been performed on a reference sample, which included the untreated tumor cell model matrix. The calculated pre-factor for proving the local presence of the cetuximab drug resulted in most of the matrix points in values equal to zero (Figure 6c control, rainbow scale image). Interestingly, in the cetuximab treated model, cetuximab could be located at the cells' cytosol, when comparing the AFM topography with hyperspectral imaging of TOM models' local cetuximab concentration, calculated by the SVD method (Figure 6c cetuximab, rainbow scale image). This goes in hand with previous findings, that cetuximab in the first line leads to EGFR inhibition by binding on its extracellular site but further initiates endocytosis of the cetuximab-EGFR complex and intracellular trafficking to the endoplasmatic reticulum (140, 141). Hereby, we proved the use of the established 3D TOM models for high-resolution label-free drug detection techniques. This technique allows for probing drug accumulations and ultimately binding site identifications at a spatial resolution scale reaching possibly down to 10 nm of a single cell in these tissues. Since this method only needs few model slices, the same model can be additionally subjected to further analysis techniques, as histological staining procedures. Future studies have to clarify, whether the distribution of cetuximab is similar in cells of different locations in the tumor model.

5.2 Prospects

In preclinical drug testing 2D- and animal-based experiments are still the main proceedings, while the use of tissue-engineered models remains minimal. Tissue-engineered models have the advantage to be made up of human material by concurrently creating an *in vivo* like surrounding for the cells by their 3D-architecture. Many studies showed the high potential of these models, and this thesis presents the generation and applicability of 3D NOM and TOM models for advanced preclinical drug testing. These models appear highly adaptable to each direction of interest. In the course of bringing more 3D models on the market and to qualify them for the general, standardized preclinical drug testing procedure, the models and the respective test procedure need to be validated in detail.

One essential step to optimize the models, is the integration of immune cells like T-cells and macrophages, to study the effects of promising immune modulators and to investigate immune system reactions caused by drugs. Furthermore, the integration of endothelial cells could allow detailed studies on tumor-induced angiogenesis and invasion. Due to the high heterogeneity of HNSCCs, the trend nowadays goes more and more to personalized medicine. In particular, after model miniaturization, drug responses could be investigated by TOM models with patient-derived tumor cells. If tumor stroma cells are not available in sufficient amounts from patient-derived mucosa, induced pluripotent stem cells (iPSC) might help to generate personalized stroma in TOM models (142). The isolation and enlargement of patient-derived tumor stem cells could furthermore help to overcome the shortage in patients' tumor material for model building procedures (143).

To elucidate the drug's distribution also in other organs and the here caused adverse drug reactions, as well as the tendency of the tumor cells to spread into other body parts, the integration of the here presented models into a multi-organ test-platform as Organ-on-a-chip, could offer further important insights. These test-platforms could additionally investigate the likeability of circulating tumor cells (CTCs) to spread and settle into different organs. Hereby, different organ characteristics like cell type- and matrix-composition, or the influence of medium components and drugs, could be studied in this context. A study about CTC cultivation in a microfluidic co-culture model derived from lung cancer, already proofed potential in the identification of mutations and their associated likeability for systemic metastasis, by next-generation sequencing (144).

Since this thesis gave first evidence about the potency of topical application, intense studies concerning saliva reconstruction and drug administration forms should be undertaken. Furthermore, the impact of the microbiome in the development of oral cancer could be as well examined, and microbiome-based diagnostics and therapeutics further identified, with the help of these models. It is already known that the microbiome is changed in oral cancer by its bacterial composition, with increased genes, favoring inflammation, proliferation, and invasion (145, 146).

To investigate long-term drug responses, the lifetime limit of the hyalograft-based models should be further evaluated. Including only human cells, the NOM and TOM models could reduce many animal-based studies. But still, to make the models completely animal-free, and so excluding the species gap as a source of error and generate models which are more ethical sound, medium components as the fetal calf serum, have to be replaced. The established 3D NOM and TOM models on hand represented their advantages and variable usage in preclinical testing. The models are ethically sound and might save money and time in contrast to the dominantly used animal models, by reducing toxic or ineffective numbers of drugs reaching the clinical phase.

For the integration of tissue-engineered models into standardized preclinical drug testing, the models have to undergo intense validation studies to guarantee the models' quality and reproducibility. Hereby, the introduction of the quality function development (QFD) into the preclinical model procedures might help to early prioritize the model's abilities and requirements, with for example the house of quality (HOQ), as a helpful tool (147). The models need to be matured and costly affordable, that they can qualify for the industry. Thus, downscaling the model size could reduce costs and offer high-throughput screenings. To increase the models' reproducibility and efficiency, automatization technics and compatible read-out techniques should be furthermore integrated into the model building and drug application setups.

5.3 Conclusion

In this thesis, organotypic NOM and TOM models have been developed and characterized, emulating closely normal oral mucosa and HNSCC morphology and protein expression. Additionally, it was possible to integrate primary tumor cells from patient-derived xenografts into the models, by concurrently reflecting different tumor phenotypes, matching to the original tumor characterization. The models offered different drug application routes, while topical administration turned out as promising, by achieving the same effects with less needed dose compared to systemic administration. However, the drug delivery system for local anti-cancer drug administration needs to be developed.

Hereby, docetaxel led to known cytostatic effects as tumor cell reduction and decreased cell proliferation. Furthermore, drug concentration measurements could be performed in automated and in real-time by integrating the model culture into a UHPLC-MS/MS device. Cetuximab, in contrast, neither helped to stop tumor cell growth nor caused tumor reduction. FLIM and AFM-IR measurements identified cetuximab's localization in the tumor epithelia, excluding the inaccessibility of the drug to the target as the reason for resistance, which rather has to be based on a cellular resistance mechanism. To elongate the models' cultivation time for improved analysis of resistance mechanisms, different matrices have been evaluated, by reaching a cultivation time of up to 7 weeks. All in all, the established models reflect closely the *in vivo* situation and allowed the examination of drug effects in various ways and could consequently allow improved preclinical drug testing. In the future, these models could help to identify promising drugs more efficiently by concurrently reducing animal testing on the basis of the 3Rs principle.

6. Summaries

6.1 Summary

Head and neck squamous cell carcinoma (HNSCC) reflect a highly heterogeneous and aggressive group of cancers for which concurrently many therapy options are associated with adverse side effects and resistance mechanisms. Although intense research is performed, the five-year survival rate is stagnating and remains low, with 50% on average. Preclinical drug testing is mainly based on animal testing, even though the gap between the species is known and the results are often misleading. The result thereof is in oncology, a success rate of only 3.4% of the drugs which have been evaluated positively in preclinical studies, in the following clinical phase. Tissue-engineered human-based models get more and more attention, due to their promising results in reflecting the human *in vivo* situation closely.

In my thesis, I developed models of normal oral mucosa (NOM) and tumor oral mucosa (TOM) and studied their suitability for the use in preclinical testing. The NOM models reflect lining mucosa, with a defined basal membrane, the stratum basale, and stratum spinosum. Primary tumor cells from patient-derived xenografts (PDX) and tumor cell lines could be integrated into the models and reflect their original tumor grading-status. The TOM models emulated a tumor characteristic heterogeneous cell mass with increased epithelial layer thickness and proliferating cells.

Besides the precise mimicking of the *in vivo* situation, the longevity of the models is of major significance to elucidate drug responses and tumor recurrences. To elongate the cultivation time, collagen was replaced by a tight-knit web of esterified hyaluronic acid fibers, called Hyalograft 3D®. The development of the epithelium occurred slower but offered a continuous proliferation of up to 7 weeks in culture, in contrast to the 2 weeks limited functionality in the collagen-based models. This shows the high influence and importance of a well-defined extracellular matrix (ECM) for improved 3D-modeling.

Drug effects have been investigated based on docetaxel and cetuximab, which are frequently used against head and neck squamous cell carcinoma, by comparing systemic and topical application routes. Docetaxel presented its potency by tumor mass reduction, with increased cell damage and inflammation as detected by lactate dehydrogenase and interleukin-6 release into the medium. Furthermore, a reduced proliferation (Ki-67), angiogenesis (HIF-1α), and increased apoptosis (TUNEL) could be determined. Interestingly, the topical application often

needed less docetaxel dosage to achieve the same cytostatic effects, compared to systemic application.

For the effectiveness and safety of a drug, the absorbance, distribution, metabolization, and elimination (ADME) of the drug have to be clarified in detail, in preclinical studies. To allow pharmacokinetic measurements in the TOM models, automated sampling for UHPLC-MS/MS analysis was integrated into the models, and docetaxel-concentrations inside the tumor tissue could be measured over 5 days. Since sample preparations are dropped, this approach seems promising for future pharmacokinetic investigations.

In contrast to docetaxel, cetuximab did not inhibit the proliferation of the tumor cells. Since cetuximab frequently triggers tumor resistances, it first had to be guaranteed, that the drug reaches its target site. Therefore, in cooperation with the physical institute of Freie Universität Berlin, the fluorescence-lifetime imaging microscopy and the atomic force microscopy-based infrared spectroscopy served for analysis.

In summary, the established models could improve preclinical drug testing since the models closely reflect the human *in vivo* situation, are easily adaptable, and offer various drug-testings, be it based on morphology, pharmacokinetics, or drug detection. Future minimization of the models might allow high-throughput analysis and approaches for personalized medicine. Moreover, the integration of immune and blood cells could enable the study of a wider drug range and reflect the *in vivo* situation even more detailed. My developed and analyzed NOM and TOM models promise improved preclinical drug testing and promote the principles of 3R as the reduction, replacement, and refinement of animal testing.

6.2 Zusammenfassung

Plattenepithelkarzinome im Kopf- und Halsbereich stellen eine sehr heterogene und aggressive Krebsart dar, bei der derzeitige Therapieoptionen mit starken Nebenwirkungen und Resistenzmechanismen assoziiert sind. Obwohl intensiv Forschung betrieben wird, stagniert die 5-Jahresüberlebensrate und verbleibt niedrig, mit 50% im Durchschnitt. Die präklinische Wirkstofftestung basiert hauptsächlich auf Tierversuchen, obwohl die Kluft zwischen den Spezies bekannt ist und die Ergebnisse meistens irreführend sind. Das Resultat davon ist in der Onkologie eine Erfolgsquote von nur 3,4% der präklinisch positiv bewerteten Wirkstoffe, in der darauffolgenden klinischen Phase. Die Züchtung von humanen Gewebsmodellen erhält immer mehr Aufmerksamkeit, auf Grund ihrer vielversprechenden Ergebnisse, die humane *in vivo* Situation nahe widerzuspiegeln.

In meiner Promotion habe ich Modelle der normalen Mundschleimhaut und von Tumormundschleimhaut entwickelt und ihre Eignung für die präklinische Forschung untersucht. Die normalen Modelle bilden die auskleidende Mundschleimhaut mit einer definierten Basalmembran, dem Stratum basale und dem Stratum spinosum, ab. Primäre Tumorzellen aus Patienten-generierten Xenotransplantaten und Tumorzelllinien konnten in die Modelle integriert werden und deren ursprüngliche Tumor-klassifizierung wiederspiegeln. Die Tumormodelle zeigten eine tumorcharakteristische heterogene Zellmasse mit einer vergrößerten epithelialen Schicht und vermehrt proliferierenden Zellen.

Neben der präzisen Wiedergabe der *in vivo* Situation ist die Langlebigkeit der Modelle von großer Bedeutung, um Wirkstoffeffekte und Tumorresistenzen aufzudecken. Zur Verlängerung der Kultivierungszeit wurde Kollagen durch ein engmaschiges Gewebe aus veresterten Hyaluronsäurefasern, Hyalograft 3D® genannt, ersetzt. Die Ausbildung des Epithels erfolgte langsamer, gewährte aber eine kontinuierliche Proliferation über bis zu 7 Wochen in Kultur, im Gegensatz zu der auf 2 Wochen beschränkten Funktionalität von Kollagen-basierten Modellen. Dies zeigt den großen Einfluss und die Wichtigkeit einer gut definierten extrazellulären Matrix für verbesserte 3D-Modellierung.

Wirkstoffeffekte wurden anhand von Docetaxel und Cetuximab untersucht, die häufig gegen Kopf- und Halskarzinomen eingesetzt werden, indem systemische und topische Applikationen miteinander verglichen wurden. Docetaxel zeigte seine Wirksamkeit durch eine reduzierte Tumormasse, mit erhöhtem Zelluntergang und Entzündungsreaktionen, die durch freigesetzte Laktat Dehydrogenase und Interleukin-6 im Medium detektiert wurden. Weiter konnte eine reduzierte Proliferation (Ki-67) und Angiogenese (HIF-1α) und erhöhte Apoptose (TUNEL)

Rate festgestellt werden. Interessanterweise wurde bei topischer Applikation oft eine geringere Dosis an Docetaxel benötigt, um dieselben zytostatischen Effekte zu erzielen wie bei systemischer Gabe.

Für die Wirksamkeit und Sicherheit des Arzneistoffes müssen in präklinischen Studien Absorption, Verteilung, Metabolisierung und Elimination der Substanz detailliert geklärt werden. Um pharmakokinetische Untersuchungen an den Tumormundschleimhautmodellen zu ermöglichen, wurde ein automatischer Probenzug für die UHPLC-MS/MS Analyse in die Modelle integriert und Docetaxel-Konzentrationen im Tumorgewebe über 5 Tage gemessen. Da Probenaufbereitungen entfielen, erscheint dieser Ansatz erfolgversprechend für zukünftige pharmakokinetische Untersuchungen.

Anders als Docetaxel wirkte Cetuximab nicht proliferationsinhibierend auf die Tumorzellen. Da unter Cetuximab häufig Tumorresistenzen auftreten, musste zunächst gewährleistet werden, dass der Arzneistoff im Testmodell zur Zielstruktur gelangt. Hierfür dienten, in Kooperation mit dem physikalischen Institut der Freien Universität Berlin, die Fluoreszenzlebensdauer-Mikroskopie und Rasterkraftmikroskopie-gekoppelte Infrarotspektroskopie.

Zusammenfassend könnten die etablierten Modelle die präklinische Wirkstofftestung verbessern, da sie die humane *in vivo* Situation nahe widerspiegeln, sie leicht adaptiert werden können und für unterschiedlichste Wirkstofftestungen verwendet werden können, sei es im Zuge der Morphologie, Pharmakokinetik oder Wirkstoffdetektion. Zukünftige Minimierung der Modelle könnte weiterhin Hochdurchsatzanalysen und Ansätze für personalisierte Medizin ermöglichen. Weiter könnte die Integrierung von Immun- und Blutzellen Untersuchungen von weiteren Wirkstoffklassen und eine noch detailliertere *in vivo* Situation Abbildung bewerkstelligen. Meine hier entwickelten normalen Mundschleimhaut und Tumor-Mundschleimhaut Modelle stellen vielversprechende präklinische Testmodelle dar, welche die 3R Prinzipien begünstigt, welche die Vermeidung, Verringerung und Verbesserung von Tierversuchen beinhaltet.

7. References

1. Bray F, Ferlay J, Soerjomataram I, Siegel RL, Torre LA, Jemal A. Global cancer statistics 2018: GLOBOCAN estimates of incidence and mortality worldwide for 36 cancers in 185 countries. CA Cancer J Clin. 2018;68:394-424.
2. Disease GBD, Injury I, Prevalence C. Global, regional, and national incidence, prevalence, and years lived with disability for 310 diseases and injuries, 1990-2015: a systematic analysis for the Global Burden of Disease Study 2015. Lancet. 2016;388:1545-602.
3. Ayaz B, Saleem K, Azim W, Shaikh A. A clinico-pathological study of oral cancers. Biomedica. 2011;27:29-32.
4. Dhanuthai K, Rojanawatsirivej S, Thosaporn W, Kintarak S, Subarnbhesaj A, Darling M, et al. Oral cancer: A multicenter study. Med Oral Patol Oral Cir Bucal. 2018;23:e23-e9.
5. Hashibe M, Brennan P, Chuang S-C, Boccia S, Castellsague X, Chen C, et al. Interaction between tobacco and alcohol use and the risk of head and neck cancer: pooled analysis in the International Head and Neck Cancer Epidemiology Consortium. Cancer Epidemiol Biomarkers Prev. 2009;18:541-50.
6. Lambert R, Sauvaget C, de Camargo Cancela M, Sankaranarayanan R. Epidemiology of cancer from the oral cavity and oropharynx. Eur J Gastroenterol Hepatol. 2011;23:633-41.
7. Shaw R, Beasley N. Aetiology and risk factors for head and neck cancer: United Kingdom National Multidisciplinary Guidelines. J Laryngol Otol. 2016;130:S9-s12.
8. Warnakulasuriya S. Global epidemiology of oral and oropharyngeal cancer. Oral Oncol. 2009;45:309-16.
9. Brandizzi D, Gandolfo M, Velazco ML, Cabrini RL, Lanfranchi HE. Clinical features and evolution of oral cancer: A study of 274 cases in Buenos Aires, Argentina. Med Oral Patol Oral Cir Bucal. 2008;13:E544-8.
10. Vigneswaran N, Williams MD. Epidemiologic trends in head and neck cancer and aids in diagnosis. Oral Maxillofac Surg Clin North Am. 2014;26:123-41.
11. Di Credico G, Polesel J, Dal Maso L, Pauli F, Torelli N, Luce D, et al. Alcohol drinking and head and neck cancer risk: the joint effect of intensity and duration. Br J Canc. 2020;123:1456-63.
12. Lea J, Bachar G, Sawka AM, Lakra DC, Gilbert RW, Irish JC, et al. Metastases to level IIb in squamous cell carcinoma of the oral cavity: A systematic review and meta-analysis. Head & Neck. 2010;32:184-90.
13. Duprez F, Berwouts D, De Neve W, Bonte K, Boterberg T, Deron P, et al. Distant metastases in head and neck cancer. Head & Neck. 2017;39:1733-43.
14. Hunter KD, Parkinson EK, Harrison PR. Profiling early head and neck cancer. Nat Rev Cancer. 2005;5:127-35.
15. Shaw RJ, Pace-Balzan A, Butterworth C. Contemporary clinical management of oral squamous cell carcinoma. Periodontol 2000. 2011;57:89-101.

16. Bagan J, Sarrion G, Jimenez Y. Oral cancer: Clinical features. Oral Oncol. 2010;46:414-7.

17. Messadi DV. Diagnostic aids for detection of oral precancerous conditions. Int J Oral Sci. 2013;5:59-65.

18. Konsultationsfassung S3-Leitlinie Diagnostik und Therapie des Mundhöhlenkarzinoms [Internet]. 2019 [cited 2020/07/28].

19. Crozier E, Sumer BD. Head and neck cancer. Med Clin North Am. 2010;94:1031-46.

20. Kowalski LP, Carvalho AL. Natural history of untreated head and neck cancer. Eur J Cancer. 2000;36:1032-7.

21. Argiris A, Karamouzis MV, Raben D, Ferris RL. Head and neck cancer. Lancet. 2008;371:1695-709.

22. Vidhyadharan S, Augustine I, Kudpaje AS, Iyer S, Thankappan K. Site-wise Differences in Adequacy of the Surgical resection Margins in Head and Neck Cancers. Indian J Surg Oncol. 2014;5:227-31.

23. Tolentino EdS, Centurion BS, Ferreira LHC, Souza APd, Damante JH, Rubira-Bullen IRF. Oral adverse effects of head and neck radiotherapy: literature review and suggestion of a clinical oral care guideline for irradiated patients. J Appl Oral Sci. 2011;19:448-54.

24. Bonner JA, Harari PM, Giralt J, Azarnia N, Shin DM, Cohen RB, et al. Radiotherapy plus cetuximab for squamous-cell carcinoma of the head and neck. N Engl J Med. 2006;354:567-78.

25. Taberna M, Oliva M, Mesía R. Cetuximab-Containing Combinations in Locally Advanced and Recurrent or Metastatic Head and Neck Squamous Cell Carcinoma. Front Oncol. 2019;9:383-.

26. Benasso M, Ponzanelli A, Merlano M, Numico G, Ricci I, Vigo V, et al. Paclitaxel, cisplatin and 5-fluorouracil in recurrent squamous cell carcinoma of the head and neck: a phase II trial from an Italian cooperative group. Acta Oncol. 2006;45:168-74.

27. Morse DL, Gray H, Payne CM, Gillies RJ. Docetaxel induces cell death through mitotic catastrophe in human breast cancer cells. Mol Cancer Ther. 2005;4:1495-504.

28. Buey RM, Barasoain I, Jackson E, Meyer A, Giannakakou P, Paterson I, et al. Microtubule Interactions with Chemically Diverse Stabilizing Agents: Thermodynamics of Binding to the Paclitaxel Site Predicts Cytotoxicity. Chem Biol. 2005;12:1269-79.

29. Europene Medicines Agency. European public assessment report "TAXOTERE", Annex l - Summary of product. Available from: https://www.ema.europa.eu/documents/product-information/taxotere-epar-product-information_en.pdf. [cited 2020/02/02] **2019** [

30. Vermorken JB, Mesia R, Rivera F, Remenar E, Kawecki A, Rottey S, et al. Platinum-based chemotherapy plus cetuximab in head and neck cancer. N Engl J Med. 2008;359:1116-27.

31. Europene Medicines Agency. European public assessment report "ERBITUX", Annex l - Summary of product characteristics. Available from: https://www.ema.europa.eu/documents/product-information/erbitux-epar-product-information_en.pdf. [cited 2020/02/02] **2019** [

32. Vermorken JB, Trigo J, Hitt R, Koralewski P, Diaz-Rubio E, Rolland F, et al. Open-Label, Uncontrolled, Multicenter Phase II Study to Evaluate the Efficacy and Toxicity of Cetuximab As a Single Agent in Patients With Recurrent and/or Metastatic Squamous Cell Carcinoma of the Head and Neck Who Failed to Respond to Platinum-Based Therapy. J Clin Oncol. 2007;25:2171-7.

33. Wong CH, Siah KW, Lo AW. Estimation of clinical trial success rates and related parameters. Biostatistics. 2019;20:273-86.

34. Fitzgerald KA, Malhotra M, Curtin CM, O' Brien FJ, O' Driscoll CM. Life in 3D is never flat: 3D models to optimise drug delivery. J Control Release. 2015;215:39-54.

35. Hsieh C-H, Chen Y-D, Huang S-F, Wang H-M, Wu M-H. The Effect of Primary Cancer Cell Culture Models on the Results of Drug Chemosensitivity Assays: The Application of Perfusion Microbioreactor System as Cell Culture Vessel. Biomed Res Int. 2015;2015:470283.

36. Vargesson N. Thalidomide-induced teratogenesis: history and mechanisms. Birth Defects Res C Embryo Today. 2015;105:140-56.

37. Merker H-J, Heger W, Sames K, Stürje H, Neubert D. Embryotoxic effects of thalidomide-derivatives in the non-human primate Callithrix jacchus. Arch Toxicol. 1988;61:165-79.

38. Pompili L, Porru M, Caruso C, Biroccio A, Leonetti C. Patient-derived xenografts: a relevant preclinical model for drug development. J Exp Clin Cancer Res. 2016;35:189-.

39. Hidalgo M, Amant F, Biankin AV, Budinská E, Byrne AT, Caldas C, et al. Patient-Derived Xenograft Models: An Emerging Platform for Translational Cancer Research. Cancer Discov. 2014;4:998-1013.

40. Klinghammer K, Raguse J-D, Plath T, Albers AE, Joehrens K, Zakarneh A, et al. A comprehensively characterized large panel of head and neck cancer patient-derived xenografts identifies the mTOR inhibitor everolimus as potential new treatment option. Int J Cancer. 2015;136:2940-8.

41. Ben-David U, Ha G, Tseng Y-Y, Greenwald NF, Oh C, Shih J, et al. Patient-derived xenografts undergo mouse-specific tumor evolution. Nat Genet. 2017;49:1567-75.

42. Tentler JJ, Tan AC, Weekes CD, Jimeno A, Leong S, Pitts TM, et al. Patient-derived tumour xenografts as models for oncology drug development. Nat Rev Clin Oncol. 2012;9:338-50.

43. Pearson AT, Finkel KA, Warner KA, Nör F, Tice D, Martins MD, et al. Patient-derived xenograft (PDX) tumors increase growth rate with time. Oncotarget. 2016;7:7993-8005.

44. Murayama T, Gotoh N. Patient-Derived Xenograft Models of Breast Cancer and Their Application. Cells. 2019;8:621.

45. Russell WMS, Burch RL. The principles of humane experimental technique: Methuen; 1959.

46. Yoo S, Noh K, Shin M, Park J, Lee K-H, Nam H, et al. In silico profiling of systemic effects of drugs to predict unexpected interactions. Sci Rep. 2018;8:1612.

47. Raunio H. In silico toxicology–non-testing methods. Front Pharmacol. 2011;2:33.

48. Laschke MW, Menger MD. Life is 3D: Boosting Spheroid Function for Tissue Engineering. Trends Biotechnol. 2017;35:133-44.

49. Marcott C, Lo M, Kjoller K, Fiat F, Baghdadli N, Balooch G, et al. Localization of human hair structural lipids using nanoscale infrared spectroscopy and imaging. Appl Spectrosc. 2014;68:564-9.

50. Huh D, Hamilton GA, Ingber DE. From 3D cell culture to organs-on-chips. Trends Cell Biol. 2011;21 12:745-54.

51. Kilic T, Navaee F, Stradolini F, Renaud P, Carrara S. Organs-on-chip monitoring: sensors and other strategies. Microphysiol Syst. 2018;2.

52. Paci A, Veal G, Bardin C, Levêque D, Widmer N, Beijnen J, et al. Review of therapeutic drug monitoring of anticancer drugs part 1 – Cytotoxics. Eur J Cancer. 2014;50:2010-9.

53. Mathijssen RH, Sparreboom A, Verweij J. Determining the optimal dose in the development of anticancer agents. Nat Rev Clin Oncol. 2014;11:272-81.

54. Esch EW, Bahinski A, Huh D. Organs-on-chips at the frontiers of drug discovery. Nat Rev Drug Discov. 2015;14:248-60.

55. Jang SH, Wientjes MG, Lu D, Au JL. Drug delivery and transport to solid tumors. Pharm Res. 2003;20:1337-50.

56. Al-Abd AM, Khedr A, Atteiah SG, Al-Abbasi FA. Intra-tumoral drug concentration mapping within solid tumor micro-milieu using in-vitro model and doxorubicin as a model drug. Saudi Pharm J. 2020;28:754-62.

57. Dong Y, Liao H, Yu J, Fu H, Zhao D, Gong K, et al. Incorporation of drug efflux inhibitor and chemotherapeutic agent into an inorganic/organic platform for the effective treatment of multidrug resistant breast cancer. J Nanobiotechnology. 2019;17:125-.

58. Zhitomirsky B, Assaraf YG. Lysosomes as mediators of drug resistance in cancer. Drug Resist Updat. 2016;24:23-33.

59. Baumann KY, Church MK, Clough GF, Quist SR, Schmelz M, Skov PS, et al. Skin microdialysis: methods, applications and future opportunities-an EAACI position paper. Clin Transl Allergy. 2019;9:24.

60. Rönquist-Nii Y, Edlund PO. Determination of corticosteroids in tissue samples by liquid chromatography-tandem mass spectrometry. J Pharm Biomed Anal. 2005;37:341-50.

61. Carlson M, Watson AL, Anderson L, Largaespada DA, Provenzano PP. Multiphoton fluorescence lifetime imaging of chemotherapy distribution in solid tumors. J Biomed Opt. 2017;22:1-9.

62. Boreham A, Kim TY, Spahn V, Stein C, Mundhenk L, Gruber AD, et al. Exploiting Fluorescence Lifetime Plasticity in FLIM: Target Molecule Localization in Cells and Tissues. ACS Med Chem Lett. 2011;2:724-8.

63. Alexiev U, Volz P, Boreham A, Brodwolf R. Time-resolved fluorescence microscopy (FLIM) as an analytical tool in skin nanomedicine. Eur J Pharm Biopharm. 2017;116:111-24.

64. Gan Y. Atomic and subnanometer resolution in ambient conditions by atomic force microscopy. Surf Sci Rep. 2009;64:99-121.

65. Dazzi A, Prater CB, Hu Q, Chase DB, Rabolt JF, Marcott C. AFM–IR: Combining Atomic Force Microscopy and Infrared Spectroscopy for Nanoscale Chemical Characterization. Appl Spectrosc. 2012;66:1365-84.

66. Vig K, Chaudhari A, Tripathi S, Dixit S, Sahu R, Pillai S, et al. Advances in Skin Regeneration Using Tissue Engineering. Int J Mol Sci. 2017;18:789.

67. Liu Y, Zhou G, Cao Y. Recent Progress in Cartilage Tissue Engineering—Our Experience and Future Directions. Engineering. 2017;3:28-35.

68. Madden MR, Finkelstein JL, Staiano-Coico L, Goodwin CW, Shires GT, Nolan EE, et al. Grafting of cultured allogeneic epidermis on second- and third-degree burn wounds on 26 patients. J Trauma. 1986;26:955-62.

69. Lauer G, Otten JE, von Specht BU, Schilli W. Cultured gingival epithelium. A possible suitable material for pre-prosthetic surgery. J Craniomaxillofac Surg. 1991;19:21-6.

70. Cooper ML, Andree C, Hansbrough JF, Zapata-Sirvent RL, Spielvogel RL. Direct Comparison of a Cultured Composite Skin Substitute Containing Human Keratinocytes and Fibroblasts to an Epidermal Sheet Graft Containing Human Keratinocytes on Athymic Mice. J Invest Dermatol. 1993;101:811-9.

71. Gerckens M, Alsafadi HN, Wagner DE, Lindner M, Burgstaller G, Königshoff M. Generation of Human 3D Lung Tissue Cultures (3D-LTCs) for Disease Modeling. J Vis Exp. 2019.

72. Huang JH, Kim J, Agrawal N, Sudarsan AP, Maxim JE, Jayaraman A, et al. Rapid fabrication of bio-inspired 3D microfluidic vascular networks. J Adv Mater. 2009;21:3567-71.

73. Fulco I, Miot S, Haug MD, Barbero A, Wixmerten A, Feliciano S, et al. Engineered autologous cartilage tissue for nasal reconstruction after tumour resection: an observational first-in-human trial. Lancet. 2014;384:337-46.

74. Finkbeiner SR, Freeman JJ, Wieck MM, El-Nachef W, Altheim CH, Tsai Y-H, et al. Generation of tissue-engineered small intestine using embryonic stem cell-derived human intestinal organoids. Biology Open. 2015;4:1462-72.

75. Huh D, Matthews BD, Mammoto A, Montoya-Zavala M, Hsin HY, Ingber DE. Reconstituting Organ-Level Lung Functions on a Chip. Science. 2010;328:1662-8.

76. Shevchenko RV, James SL, James SE. A review of tissue-engineered skin bioconstructs available for skin reconstruction. J R Soc Interface. 2010;7:229-58.

77. Tamay DG, Dursun Usal T, Alagoz AS, Yucel D, Hasirci N, Hasirci V. 3D and 4D Printing of Polymers for Tissue Engineering Applications. Front Bioeng Biotechnol. 2019;7.

78. Cruchley AT, Bergmeier LA. Structure and Functions of the Oral Mucosa. In: Bergmeier LA, editor. Oral Mucosa in Health and Disease: A Concise Handbook. Cham: Springer International Publishing; 2018. p. 1-18.

79. Otsuka-Tanaka Y, Oommen S, Kawasaki M, Kawasaki K, Imam N, Jalani-Ghazani F, et al. Oral lining mucosa development depends on mesenchymal microRNAs. J Dent Res. 2013;92:229-34.

80. Moharamzadeh K, Brook I, Van Noort R, Scutt A, Thornhill M. Tissue-engineered oral mucosa: a review of the scientific literature. J Dent Res. 2007;86:115-24.

81. Moharamzadeh K. 14 - Oral mucosa tissue engineering. In: Tayebi L, Moharamzadeh K, editors. Biomaterials for Oral and Dental Tissue Engineering: Woodhead Publishing; 2017. p. 223-44.

82. Wang Z, Wang Y, Farhangfar F, Zimmer M, Zhang Y. Enhanced keratinocyte proliferation and migration in co-culture with fibroblasts. PloS One. 2012;7:e40951-e.

83. Okazaki M, Yoshimura K, Suzuki Y, Harii K. Effects of Subepithelial Fibroblasts on Epithelial Differentiation in Human Skin and Oral Mucosa: Heterotypically Recombined Organotypic Culture Model. Plast Reconstr Surg. 2003;112:784-92.

84. Humphrey SP, Williamson RT. A review of saliva: normal composition, flow, and function. J Prosthet Dent. 2001;85:162-9.

85. Hanahan D, Weinberg RA. Hallmarks of cancer: the next generation. Cell. 2011;144:646-74.

86. Kalyankrishna S, Grandis JR. Epidermal growth factor receptor biology in head and neck cancer. J Clin Oncol. 2006;24:2666-72.

87. Pai SI, Westra WH. Molecular pathology of head and neck cancer: implications for diagnosis, prognosis, and treatment. Annu Rev Pathol. 2009;4:49-70.

88. Dongari-Bagtzoglou A, Kashleva H. Development of a novel three-dimensional in vitro model of oral Candida infection. Microb Pathog. 2006;40:271-8.

89. de Carvalho Dias K, de Sousa DL, Barbugli PA, Cerri PS, Salih VM, Vergani CE. Development and characterization of a 3D oral mucosa model as a tool for host-pathogen interactions. J Microbiol Methods. 2018;152:52-60.

90. Schmalz G, Schweikl H, Hiller KA. Release of prostaglandin E2, IL-6 and IL-8 from human oral epithelial culturemodels after exposure to compounds of dental materials. Eur J Oral Sci. 2000;108:442-8.

91. Moharamzadeh K, Franklin KL, Brook IM, van Noort R. Biologic assessment of antiseptic mouthwashes using a three-dimensional human oral mucosal model. J Periodontol. 2009;80:769-75.

92. Moharamzadeh K, Franklin KL, Smith LE, Brook IM, van Noort R. Evaluation of the Effects of Ethanol on Monolayer and 3D Models of Human Oral Mucosa. J Environ Anal Toxicol. 2015;5:1.

93. Jo Y, Choi N, Kim K, Koo H-J, Choi J, Kim HN. Chemoresistance of Cancer Cells: Requirements of Tumor Microenvironment-mimicking In Vitro Models in Anti-Cancer Drug Development. Theranostics. 2018;8:5259-75.

94. Kalluri R. Basement membranes: structure, assembly and role in tumour angiogenesis. Nat Rev Cancer. 2003;3:422-33.

95. Kessenbrock K, Plaks V, Werb Z. Matrix metalloproteinases: regulators of the tumor microenvironment. Cell. 2010;141:52-67.

96. Correia AL, Bissell MJ. The tumor microenvironment is a dominant force in multidrug resistance. Drug Resist Updat. 2012;15:39-49.

97. Mouw JK, Yui Y, Damiano L, Bainer RO, Lakins JN, Acerbi I, et al. Tissue mechanics modulate microRNA-dependent PTEN expression to regulate malignant progression. Nat Med. 2014;20:360-7.

98. Calvo F, Ege N, Grande-Garcia A, Hooper S, Jenkins RP, Chaudhry SI, et al. Mechanotransduction and YAP-dependent matrix remodelling is required for the generation and maintenance of cancer-associated fibroblasts. Nat Cell Biol. 2013;15:637-46.

99. J JP-P, Jakubik A, Przeklasa-Bierowiec A, Muszynska B. Artificial saliva and its use in biological experiments. J Physiol Pharmacol. 2017;68:807-13.

100. Pow EHN, Chen Z, Kwong DLW, Lam OLT. Salivary Anionic Changes after Radiotherapy for Nasopharyngeal Carcinoma: A 1-Year Prospective Study. PloS One. 2016;11:e0152817-e.

101. Hanahan D, Coussens Lisa M. Accessories to the Crime: Functions of Cells Recruited to the Tumor Microenvironment. Cancer Cell. 2012;21:309-22.

102. Box GEP. Robustness in the Strategy of Scientific Model Building. In: Launer RL, Wilkinson GN, editors. Robustness in Statistics: Academic Press; 1979. p. 201-36.

103. Valéry P. Mauvaises pensées et autres: Gallimard Paris, France; 1942.

104. Sawant S, Dongre H, Singh AK, Joshi S, Costea DE, Mahadik S, et al. Establishment of 3D Co-Culture Models from Different Stages of Human Tongue Tumorigenesis: Utility in Understanding Neoplastic Progression. PLoS One. 2016;11:e0160615.

105. Kinikoglu B, Rodríguez-Cabello JC, Damour O, Hasirci V. The influence of elastin-like recombinant polymer on the self-renewing potential of a 3D tissue equivalent derived from human lamina propria fibroblasts and oral epithelial cells. Biomaterials. 2011;32:5756-64.

106. Gaballah K, Costea DE, Hills A, Gollin SM, Harrison P, Partridge M. Tissue engineering of oral dysplasia. J Pathol. 2008;215:280-9.

107. Colley HE, Hearnden V, Jones AV, Weinreb PH, Violette SM, MacNeil S, et al. Development of tissue-engineered models of oral dysplasia and early invasive oral squamous cell carcinoma. Br J Canc. 2011;105:1582-92.

108. Roskelley CD, Srebrow A, Bissell MJ. A hierarchy of ECM-mediated signalling regulates tissue-specific gene expression. Curr Opin Cell Biol. 1995;7:736-47.

109. Hausmann C, Zoschke C, Wolff C, Darvin ME, Sochorová M, Kováčik A, et al. Fibroblast origin shapes tissue homeostasis, epidermal differentiation, and drug uptake. Sci Rep. 2019;9:1-10.

110. Poltavets V, Kochetkova M, Pitson SM, Samuel MS. The Role of the Extracellular Matrix and Its Molecular and Cellular Regulators in Cancer Cell Plasticity. Front Oncol. 2018;8.

111. Stark HJ, Willhauck MJ, Mirancea N, Boehnke K, Nord I, Breitkreutz D, et al. Authentic fibroblast matrix in dermal equivalents normalises epidermal histogenesis and dermoepidermal junction in organotypic co-culture. Eur J Cell Biol. 2004;83:631-45.

112. Carlson MW, Alt-Holland A, Egles C, Garlick JA. Three-dimensional tissue models of normal and diseased skin. Curr Protoc Cell Biol. 2008;Chapter 19:Unit-19.9.

113. Eastman A. Improving anticancer drug development begins with cell culture: misinformation perpetrated by the misuse of cytotoxicity assays. Oncotarget. 2017;8:8854-66.

114. Michel M, L'Heureux N, Pouliot R, Xu W, Auger FA, Germain L. Characterization of a new tissue-engineered human skin equivalent with hair. In Vitro Cell Dev Biol Anim. 1999;35:318-26.

115. Fleischmajer R, Contard P, Schwartz E, MacDonald ED, 2nd, Jacobs L, 2nd, Sakai LY. Elastin-associated microfibrils (10 nm) in a three-dimensional fibroblast culture. J Invest Dermatol. 1991;97:638-43.

116. Stark H-J, Boehnke K, Mirancea N, Willhauck MJ, Pavesio A, Fusenig NE, et al. Epidermal Homeostasis in Long-Term Scaffold-Enforced Skin Equivalents. J Investig Dermatol Symp Proc. 2006;11:93-105.

117. Gstraunthaler G, Lindl T, Valk JBF. A plea to reduce or replace fetal bovine serum in cell culture media. Cytotechnology. 2013;65.

118. Mosaad E, Chambers K, Futrega K, Clements J, Doran M. The Microwell-mesh: A high-throughput 3D prostate cancer spheroid and drug-testing platform. Sci Rep. 2018;8:1-12.

119. Breslin S, Driscoll L. The relevance of using 3D cell cultures, in addition to 2D monolayer cultures, when evaluating breast cancer drug sensitivity and resistance. Oncotarget. 2016;7.

120. Chambers KF, Mosaad EMO, Russell PJ, Clements JA, Doran MR. 3D Cultures of Prostate Cancer Cells Cultured in a Novel High-Throughput Culture Platform Are More Resistant to Chemotherapeutics Compared to Cells Cultured in Monolayer. PLoS One. 2014;9:e111029.

121. Paul SP. Melanoma arising after imiquimod use. Case Rep Med. 2014;2014:267535-.

122. Sankar V, Hearnden V, Hull K, Juras DV, Greenberg M, Kerr A, et al. Local drug delivery for oral mucosal diseases: challenges and opportunities. Oral Dis. 2011;17:73-84.

123. Hearnden V, Sankar V, Hull K, Juras DV, Greenberg M, Kerr AR, et al. New developments and opportunities in oral mucosal drug delivery for local and systemic disease. Adv Drug Deliv Rev. 2012;64:16-28.

124. Colley HE, Said Z, Santocildes-Romero ME, Baker SR, D'Apice K, Hansen J, et al. Pre-clinical evaluation of novel mucoadhesive bilayer patches for local delivery of clobetasol-17-propionate to the oral mucosa. Biomaterials. 2018;178:134-46.

125. Zou P, Yu Y, Zheng N, Yang Y, Paholak HJ, Yu LX, et al. Applications of human pharmacokinetic prediction in first-in-human dose estimation. Aaps j. 2012;14:262-81.

126. Roth W, Beschke K, Jauch R, Zimmer A, Koss FW. Fully automated high-performance liquid chromatography: A new chromatograph for pharmacokinetic drug monitoring by direct injection of body fluids. J Chromatogr B Biomed. 1981;222:13-22.

127. Vermorken JB, Trigo J, Hitt R, Koralewski P, Diaz-Rubio E, Rolland F, et al. Open-label, uncontrolled, multicenter phase II study to evaluate the efficacy and toxicity of cetuximab as a single agent in patients with recurrent and/or metastatic squamous cell carcinoma of the head and neck who failed to respond to platinum-based therapy. J Clin Oncol. 2007;25:2171-7.

128. Braig F, Kriegs M, Voigtlaender M, Habel B, Grob T, Biskup K, et al. Cetuximab resistance in head and neck cancer is mediated by EGFR-K521 polymorphism. Cancer Res. 2017;77:1188-99.

129. Kjaer I, Lindsted T, Frohlich C, Olsen JV, Horak ID, Kragh M, et al. Cetuximab Resistance in Squamous Carcinomas of the Upper Aerodigestive Tract Is Driven by Receptor Tyrosine Kinase Plasticity: Potential for mAb Mixtures. Mol Cancer Ther. 2016;15:1614-26.

130. Boer E, Warram J, Tucker M, Hartman Y, Moore L, Jong J, et al. In Vivo Fluorescence Immunohistochemistry: Localization of Fluorescently Labeled Cetuximab in Squamous Cell Carcinomas. Sci Rep. 2015;5:10169.

131. Lee CM, Tannock IF. The distribution of the therapeutic monoclonal antibodies cetuximab and trastuzumab within solid tumors. BMC Cancer. 2010;10:255-.

132. Takeo E, Shimma S. Development of quantitative imaging mass spectrometry (q-IMS) for drug visualization using animal tissues. Surf Interface Anal. 2019;51:21-6.

133. Végvári Á, Fehniger TE, Rezeli M, Laurell T, Döme B, Jansson B, et al. Experimental Models to Study Drug Distributions in Tissue Using MALDI Mass Spectrometry Imaging. J Proteome Res. 2013;12:5626-33.

134. Yamamoto K, Klossek A, Fuchs K, Watts B, Raabe J, Flesch R, et al. Soft X-ray microscopy for probing of topical tacrolimus delivery via micelles. Eur J Pharm Biopharm. 2019;139:68-75.

135. Pavan Taffner BM, Mattos FB, Cunha MCd, Saraiva FP. The use of optical coherence tomography for the detection of ocular toxicity by ethambutol. PloS One. 2018;13:e0204655-e.

136. Gemperline E, Chen B, Li L. Challenges and recent advances in mass spectrometric imaging of neurotransmitters. Bioanalysis. 2014;6:525-40.

137. Greer T, Sturm R, Li L. Mass spectrometry imaging for drugs and metabolites. J Proteomics. 2011;74:2617-31.

138. Zhang Q, Shi Y, Xu H, Zhou L, Gao J, Jiang J, et al. Evaluating the efficacy of the anticancer drug cetuximab by atomic force microscopy. RSC Advances. 2018;8:21793-7.

139. Zhang X, Balhorn R, Mazrimas J, Kirz J. Mapping and Measuring DNA to Protein Ratios in Mammalian Sperm Head by XANES Imaging. Journal of Structural Biology. 1996;116:335-44.

140. Bhattacharyya S, Bhattacharya R, Curley S, McNiven MA, Mukherjee P. Nanoconjugation modulates the trafficking and mechanism of antibody induced receptor endocytosis. Proc Natl Acad Sci U S A. 2010;107:14541-6.

141. Liao H-J, Carpenter G. Cetuximab/C225-induced intracellular trafficking of epidermal growth factor receptor. Cancer Res. 2009;69:6179-83.

142. Osaki T, Uzel SGM, Kamm RD. Microphysiological 3D model of amyotrophic lateral sclerosis (ALS) from human iPS-derived muscle cells and optogenetic motor neurons. Sci Adv. 2018;4:eaat5847.

143. Akbarzadeh M, Maroufi NF, Tazehkand AP, Akbarzadeh M, Bastani S, Safdari R, et al. Current approaches in identification and isolation of cancer stem cells. Journal of Cellular Physiology. 2019;234:14759-72.

144. Zhang Z, Shiratsuchi H, Lin J, Chen G, Reddy RM, Azizi E, et al. Expansion of CTCs from early stage lung cancer patients using a microfluidic co-culture model. Oncotarget. 2014;5:12383-97.

145. Chattopadhyay I, Verma M, Panda M. Role of Oral Microbiome Signatures in Diagnosis and Prognosis of Oral Cancer. Technol Cancer Res Treat. 2019;18:1533033819867354-.

146. Zhang L, Liu Y, Zheng HJ, Zhang CP. The Oral Microbiota May Have Influence on Oral Cancer. Front Cell Infect Microbiol. 2020;9:476-.

147. Schäfer-Korting M, Zoschke C. How qualification of 3d disease models cuts the gordian knot in preclinical drug development. In: Schäfer-Korting M, Landsiedel R, Maria-Engler SS, editors. Handbook of experimental pharmacology: "Organotypic models in drug development". Cham (Switzerland): Springer Nature; in press.

8. Publication Record

Original Articles

GRONBACH, L., JURMEISTER, P., SCHÄFER-KORTING, M., KEILHOLZ, U., TINHOFER, I. & ZOSCHKE, C. Primary extracellular matrix enables long-term cultivation of full-thickness human tumor oral mucosa models. Frontiers in Bioengineering and Biotechnology **2020**;8:579896 doi 10.3389/fbioe.2020.579896 *In press*

GRONBACH, L., WOLFF, C., KLINGHAMMER, K., STELLMACHER, J., JURMEISTER, P., ALEXIEV, U., SCHÄFER-KORTING, M., TINHOFER, I., KEILHOLZ, U. & ZOSCHKE, C. A multilayered epithelial mucosa model of head neck squamous cell carcinoma for analysis of tumor-microenvironment interactions and drug development. Biomaterials **2020**;258:120277 doi 10.1016/j.biomaterials.2020.120277.

JOSEPH, J., **GRONBACH, L.**, GARCÍA-MILLER, J., CRUZ, LM., WUEST, B., KEILHOLZ, U., ZOSCHKE, C. & PARR, MK. Automated Real-Time Pharmacokinetic Profiling in 3D Models: A Novel Approach for Personalized Medicine. Pharmaceutics **2020**;12:413 doi 10.3390/pharmaceutics12050413.

Conference Proceedings

GRONBACH, L., WOLFF, C., KLINGHAMMER, K., ZOSCHKE, C., KEILHOLZ, U. & SCHÄFER-KORTING, M. 2019. Organotypic head and neck cancer models for drug testing. 84th Annual Meeting of German Society for Experimental and Clinical Pharmacology and Toxicology (DGPT). Stuttgart / Germany: February 25-28.

ZOSCHKE, C., **GRONBACH, L.**, KLINGHAMMER, K.,KEILHOLZ, U., & SCHÄFER-KORTING, M. 2018. Remodeling the microenvironment of epithelial cancers to better understand cancer metastasis and drug effects. *4th AEK Autumn School, German Cancer Foundation*. Potsdam / Germany: November 05-07.

GRONBACH, L., WOLFF, C., KLINGHAMMER, K., ZOSCHKE, C., KEILHOLZ, U., & SCHÄFER-KORTING, M. 2018. Organotypic head and neck cancer models for drug testing. *18th Annual Congress of EUSAAT & 21st European Congress on Alternatives to Animal Testing*. Linz / Austria: ALTEX Proceedings. September 23-26.

ZOSCHKE, C., WOLFF, C., **GRONBACH, L.**, KLINGHAMMER, K., KEILHOLZ, U. & SCHÄFER-KORTING, M. 2018. Human cell-based carcinoma models for the improved prediction of drug absorption. *Central European Society for Anticancer Drug Research Annual Meeting.* Berlin / Germany: March 15-17.

GRONBACH, L., WOLFF, C., KLINGHAMMER, K., ZOSCHKE, C., KEILHOLZ, U. & SCHÄFER-KORTING, M. 2018. Patient-derived organotypic models of head and neck cancer emulate tumor grading in vivo. *Deutscher Krebskongress 2018 (German Cancer Congress).* Berlin / Germany: February 21-24.

GRONBACH, L., WOLFF, C., KLINGHAMMER, K., ZOSCHKE, C., KEILHOLZ, U. & SCHÄFER-KORTING, M. 2017. Patient-derived organotypic models of head and neck cancer emulate tumor grading in vivo. *Annual Meeting of the German Pharmaceutical Society-DPhG.* Saarbrücken / Germany: September 26-29.

Talks

- Organotypic head and neck cancer models – a human cell-based evaluation of drug delivery. *BB3R Seminar* of Dahlem Research School Graduate Studies Biomedical Sciences, 2019-05-14

- Organotypic head and neck cancer models for drug testing. *84th Annual Meeting of German Society for Experimental and Clinical Pharmacology and Toxicology* (DGPT). Stuttgart / Germany. 2019-02-28

- Organotypic head and neck cancer models – a human cell-based evaluation of drug delivery. *BB3R Seminar* of Dahlem Research School Graduate Studies Biomedical Sciences, 2017-12-05

9. Statement of Authorship

I hereby confirm, that I have authored this thesis independently and that I have not used other than the declared sources. I declare, that I have explicitly marked all material that has been quoted either literally or by content from the used sources. I did not receive any help or support from commercial consultants. Furthermore, I confirm that this thesis has not yet been submitted as part of another examination process neither in identical nor in a similar form.

Berlin, 27st November 2020

Place, Date

Leonie Gronbach

10. Curriculum Vitae

For reasons of data protection, the curriculum vitae is not published in the electronic version.